ADVANCED ELECTRICAL CHARACTERIZATION OF ORGANIC–INORGANIC HYBRID PEROVSKITE SOLAR CELLS BY IMPEDANCE SPECTROSCOPY

A THESIS SUBMITTED TO
THE GRADUATE SCHOOL OF NATURAL AND APPLIED SCIENCES
OF
MIDDLE EAST TECHNICAL UNIVERSITY

BY

MEHMET CEM ŞAHİNER

IN PARTIAL FULFILLMENT OF THE REQUIREMENTS
FOR
THE DEGREE OF MASTER OF SCIENCE
IN
ELECTRICAL AND ELECTRONICS ENGINEERING

SEPTEMBER 2018

Approval of the Thesis:

ADVANCED ELECTRICAL CHARACTERIZATION OF ORGANIC–INORGANIC HYBRID PEROVSKITE SOLAR CELLS BY IMPEDANCE SPECTROSCOPY

submitted by **MEHMET CEM ŞAHİNER** in partial fulfillment of the requirements for the degree of **Master of Science in Electrical and Electronics Engineering Department, Middle East Technical University** by,

Prof. Dr. Halil Kalıpçılar
Dean, Graduate School of **Natural and Applied Sciences** _____

Prof. Dr. Tolga Çiloğlu
Head of Department, **Electrical and Electronics Eng.** _____

Asst. Prof. Dr. Selçuk Yerci
Supervisor, **Electrical and Electronics Eng. Dept., METU** _____

Examining Committee Members:

Prof. Dr. Nevzat Güneri Gençer
Electrical and Electronics Engineering Dept., METU _____

Asst. Prof. Dr. Selçuk Yerci
Electrical and Electronics Engineering Dept., METU _____

Prof. Dr. Cengiz Beşikci
Electrical and Electronics Engineering Dept., METU _____

Assoc. Prof. Dr. Görkem Günbaş
Chemistry Dept., METU _____

Assoc. Prof. Dr. Savaş Sönmezoğlu
Metallurgical and Materials Engineering Dept., KMU _____

Date: 05.09.2018

I hereby declare that all information in this document has been obtained and presented in accordance with academic rules and ethical conduct. I also declare that, as required by these rules and conduct, I have fully cited and referenced all material and results that are not original to this work.

Name, Last Name: Mehmet Cem, Şahiner

Signature:

ABSTRACT

ADVANCED ELECTRICAL CHARACTERIZATION OF ORGANIC–INORGANIC HYBRID PEROVSKITE SOLAR CELLS BY IMPEDANCE SPECTROSCOPY

Şahiner, Mehmet Cem
M.Sc., Department of Electrical and Electronics Engineering
Supervisor: Asst. Prof. Dr. Selçuk Yerci

September 2018, 92 pages

The solar cells employing organic–inorganic hybrid perovskites combine high power conversion efficiency with low-cost processability. Owing to the transfer of expertise acquired in dye-sensitized solar cell research, photovoltaic perovskite research expanded in an extraordinary pace. Efficiency values escalated rapidly mostly through refinement of fabrication methods and optimization of deposition conditions. The understanding of device physics, however, lacked such momentum because the focus was mainly on the competitive race for efficiency. Informative characterization techniques often left unattended and used mostly to connect the observed efficiency increase to modifications in fabrication conditions and methods. In this thesis, perovskite solar cells were studied by electrical impedance spectroscopic techniques, driven by the intention of contributing to the thorough understanding of operation principles. In this context, the impedance response of planar p–i–n heterojunctions employing perovskite light harvesters was modelled. A clear link between both high and low-frequency features of impedance spectra and underlying recombination process was revealed. For nickel oxide-based devices, recombination was shown to be coupled to the geometrical capacitance of device in the high frequency, and to the carrier accumulation on the interface in the low-frequency regime. Passivation of sputtered nickel oxide surface by an organic interlayer material was demonstrated. For the devices employing passivating interlayers, the low-frequency feature was inferred

to be coupled to the ionic motion in perovskite absorber. Telltale signs of surface passivation were detected from impedance measurements through both the increase of recombination resistance and the disappearance of surface carrier accumulation.

Keywords: Impedance Spectroscopy, Perovskite Solar Cells, Nickel Oxide, Surface Passivation

ÖZ

ORGANİK–İNORGANİK PEROVSKİT GÜNEŞ HÜCRELERİNİN EMPEDANS SPEKTROSKOPİSİ İLE ELEKTRİKSEL KARAKTERİZASYONU

Şahiner, Mehmet Cem
Yüksek Lisans, Elektrik–Elektronik Mühendisliği Bölümü
Tez Yöneticisi: Dr. Öğr. Üyesi Selçuk Yerci

Eylül 2018, 92 sayfa

Organik–inorganik hibrit perovskitler kullanılarak geliştirilen güneş hücreleri düşük maliyetli üretim tekniklerini yüksek verim değerleri ile birlikte sunmaktadır. Boya esaslı güneş pilleri araştırmalarında elde edilen bilgi birikiminin aktarımı sonucu, perovskit araştırmaları olağanüstü bir hızda seyretmiştir. Üretim yöntemlerinin ve koşullarının iyileştirilmesi sonucunda, hücre verimleri süratli bir şekilde yükselmiştir. Araştırmacıların verimlilik yarışına odaklanmasıyla ilgili aygıtların arkasında yatan fiziksel prensipler bütünüyle belirlenememiş, karakterizasyon teknikleri çoğunlukla farklı aygıtların verim yönünden karşılaştırılması amacıyla sınırlı kalmıştır. Bu konuya ışık tutmak amacıyla, perovskit güneş hücreleri üzerinde elektriksel empedans spektroskopisi çalışmaları tez kapsamında gerçekleştirilmiştir. p–i–n heteroeklem yapısındaki perovskit güneş hücrelerinin empedans karakteristiği modellenmiştir. Yük taşıyıcılarını yokoluşum dinamikleri ile aygıtların düşük ve yüksek frekanstaki empedans yanıtları bağdaştırılmış; nikel oksit tabakası içeren hücrelerde elektron-delik çiftlerinin yokoluşunun yüksek frekansta hücrenin geometrik kapasitansına, düşük frekansta ise yüklerin arayüzeyde toplanmasına olan bağı gösterilmiştir. Saçtırma yöntemiyle üretilen nikel oksit tabakaların organik ara katmanlar vasıtasıyla yüzey pasivasyonu gösterilmiştir. İlgili pasive edilmiş hücrelerde düşük frekans karakteristiğinin perovskit katmanındaki iyon göçü ile ilgisi açıklanmıştır. Yokoluşum

direncinin artışı ve akümülasyon kapasitansının ortadan kalkması gibi yüzey pasivasyonunu doğrulayan bulgular empedans spektroskopisi ile elde edilmiştir.

Anahtar Kelimeler: Empedans Spektroskopisi, Perovskit Güneş Hücreleri, Nikel Oksit, Yüzey Pasivasyonu

To İlayda

ACKNOWLEDGEMENTS

I would like to express my heartfelt gratitude to my supervisor Professor Selçuk Yerci for his guidance. Without his continuous support and confidence in me, this work would not be possible. The mutual sincerity established between the members of his research group is reflective of his personality. Next, I would like to thank Professor Görkem Günbaş for the insightful discussions on the chemistry. His skillful approach to problems that is encountered in fabrication surely helped a lot. Fabrication of devices was possible thanks to the joint work conducted by both groups: Prof. Yerci's Applied Photonics and Photovoltaics (APP) and Günbaş Lab. Weekly meetings that we held as the members of both groups were productive.

I am grateful to the group members as they are wonderful friends. They helped me out many times for the experiments in the lab. I am grateful to Wiria Soltanpoor for his being my lab mate for more than three years. He and I together set the vacuum evaporation system up and keep it in order. His help on variety of structural and optical characterizations are also much appreciated. Special thanks go to Dr. Hava Kaya and Esra Bağ for their expertise on chemistry. We spent a lot of time together in the lab. They were always helpful and supportive. The other members should be mentioned as well: Deniz Türkay for the insightful discussions we made on semiconductors physics, Gence Bektaş for the fabrication of sputtered layers and his overall positivity, Merve Derya Oflaz for her help in the substrate preparation, Donald Isufi for the 3D printed parts of the custom-made impedance measurement setup, Ayça Yıldırım for we together carried out some impedance measurements, Can Özcan for being the founder of the video game nights and for, along with Arman Ayan, we were the thesis writing buddies.

I also thank Prof. Umut Orguner. He helped me to stabilize the derivation operation in my maximum-power-point tracker design. It was very kind of him, since he attended to my problem like his own.

I would also like to thank my family. They are always loving and supportive to me. They deserve the biggest praise. And to İlayda I express my sincerest gratitude. I thank her for the love and understanding she shows.

We carried out the fabrication and characterization of devices in the laboratories of Center for Solar Energy Research and Applications (GÜNAM). I would like to thank the members and employees of GÜNAM for their technical support.

This thesis work was supported by the Scientific and Technical Research Council of Turkey (TÜBİTAK) under the contract number 315M306.

TABLE OF CONTENTS

ABSTRACT.....v

ÖZ.....vii

ACKNOWLEDGMENTS.....x

TABLE OF CONTENTS.....xii

LIST OF TABLES.....xiv

LIST OF FIGURES.....xv

NOMENCLATURE.....xvii

CHAPTERS

1. INTRODUCTION.....1

1.1. Brief History of Solar Cells.....2

1.2. Perovskite Photovoltaic Materials.....4

1.3. Structural Evolution of Perovskite Solar Cells.....6

1.4. The Scope of The Thesis.....8

2. THEORETICAL BACKGROUND.....9

2.1. Physical Characteristics of Perovskites.....9

2.2. Recombination and Defect Tolerance of Perovskites.....11

2.3. Ion Migration and Hysteresis.....12

2.4. Other Issues.....14

2.5. Electrical Basics of Solar Cells.....15

2.6. Basics of Impedance.....18

2.7. Representation of Impedance Response and Equivalent Circuits.....20

2.8. Fitting of Impedance Response.....23

3. FABRICATION AND INSTRUMENTATION.....27

3.1. Structure and Fabrication of Perovskite Solar Cells.....27

3.2. Current–Voltage Measurements.....32

3.3. Impedance Measurements.....33

4. RELIABLE EFFICIENCY MEASUREMENTS OF PEROVSKITE SOLAR CELLS.....35

4.1. Effect of Hysteresis in Efficiency Measurements.....35

4.2. Efficiency Measurement Techniques.....36

4.3. Design of a Maximum-Power-Point Tracker.....40

4.4. Final Remarks.....44

5. IMPEDANCE RESPONSE AND MODELLING.....45

5.1. Impedance Spectroscopy.....45

5.2. Recombination in Impedance Response.....46

5.3. High Frequency Modelling.....48

5.4. Low Frequency Modelling.....56

6. ANALYSIS OF IMPEDANCE SPECTRA AND DISCUSSION.....63

6.1. Summary of Fabricated Perovskite Solar Cells.....63

6.2. Analysis of PEDOT:PSS Based Devices.....64

6.3. Analysis of Nickel Oxide Based Devices.....67

6.4. Discussion.....73

7. CONCLUSION AND FUTURE OUTLOOK.....79

REFERENCES.....83

APPENDIX.....91

LIST OF TABLES

TABLES

Table 1.1 Selected optoelectronic properties of perovskites and other PV technologies.....5

Table 3.1 Materials used in perovskite solar cell fabrication.....30

Table 5.1 Parameters calculated by fitting to the HF equivalent circuit.....54

Table 5.2 Parameters calculated by fitting to the overall impedance model.....60

Table 6.1 Photovoltaic performance parameters of the studied PSCs.....64

LIST OF FIGURES

FIGURES

Figure 1.1 Three generations of photovoltaics.....2

Figure 1.2 Crystal structure of perovskites: ABX_3.....4

Figure 1.3 Schematics of structural evolution of perovskite solar cells.....7

Figure 2.1 A schematic diagram and the equivalent circuit of a p–n junction solar cell.....15

Figure 2.2 Typical I–V curve of a perovskite solar cell.....17

Figure 2.3 Measurement of complex impedance in time domain and linearization of the response on I–V characteristics.....19

Figure 2.4 Bode plot and R, X vs. f plots for an RC circuit.....20

Figure 2.5 Nyquist plot of impedance of a parallel RC circuit.....21

Figure 3.1 The architecture and layout of an n–i–p perovskite solar cell.....28

Figure 3.2 Schematics of perovskite layer fabrication.....29

Figure 3.3 An SEM micrograph of a perovskite solar cell.....32

Figure 3.4 Impedance measurement configuration at open-circuit.....33

Figure 4.1 I–V curves demonstrating severe hysteresis in a TiO2-based n–i–p PSC.....36

Figure 4.2 Dynamic I–V measurement in time domain.....38

Figure 4.3 Comparison of dynamic I–V and standard I–V for PSCs.....38

Figure 4.4 PID control schematic for MPPT.....40

Figure 4.5 MPPT block diagram.....40

Figure 4.6 Evolution of cell voltage and current in logarithmic time scale, and efficiency in linear time scale for an MPPT measurement.....44

Figure 5.1 Nyquist plot of a PSC featuring high and low frequency characteristics.....49

Figure 5.2 Ideal and modified high frequency models for PSCs.....50

Figure 5.3 Set of impedance spectra of a PSC in different steady-state conditions.....52

Figure 5.4 The equivalent HF model and the Nyquist plots for a p–i–n PSC.....54

Figure 5.5 Illumination dependence of R_{HF} and R_{rec}.....55

Figure 5.6 Nyquist plot of a PSC measured from 100 Hz to 1 MHz.....56

Figure 5.7 Equivalent circuits modelling processes having two time constants.....57

Figure 5.8 Overall impedance model of PSCs.....58

Figure 5.9 Nyquist plots at different irradiance levels for a NiO_x-based PSC.....59

Figure 5.10 Sample impedance spectra showing fitting accuracy.....59

Figure 5.11 Illumination dependence of low-frequency resistance R_{LF}.....61

Figure 6.1 A selection of I–V curves for PEDOT:PSS-based devices and their R_{HF}–Φ characteristics.....65

Figure 6.2 The I–V curves of the most stable NiO_x-based PSCs.....68

Figure 6.3 The illumination dependence of R_{HF} and R_{REC} for NX and NT….....70

Figure 6.4 The Nyquist plots of NX, NT and NP at 30% equivalent Sun.....71

Figure 6.5 Illumination dependence of dispersion parameter p and time constant τ.....72

Figure 6.6 Band diagram schematics for devices employing unpassivated and passivated NiOx layers.....73

Figure 6.7 Illumination dependence of V_{OC} for NX and NT.....76

NOMENCLATURE

a-Si	Amorphous silicon
c-Si	Single-crystal silicon
BCP	Bathocuproine
C_{geo}	Geometrical capacitance
C_{LF}	Low-frequency capacitance
CdTe	Cadmium telluride
CIGS	Copper indium gallium selenide
CPE	Constant phase element
DSSC	Dye-sensitized solar cell
DUT	Device under test
ETL	Electron transport layer
FA	Formamidinium
FF	Fill factor
FTO	Fluorine doped tin oxide
GaAs	Gallium arsenide
HF	High-frequency
HTL	Hole transport layer
IC	Integrated circuit
I–V	Current-voltage
IS	Impedance spectroscopy
ITO	Indium tin oxide
J_{SC}	Short circuit current density
LF	Low-frequency
MA	Methylammonium
MAI	Methylammonium iodide
mc-Si	Multi-crystalline silicon

MPP	Maximum power point
MPPT	Maximum power point tracker
NiO_x	Nickel oxide
NP	NiO_x/PEDOT:PSS device
NT	NiO_x/poly-TPD device
NX	NiO_x-only device
OIHP	Organic–inorganic hybrid perovskite
OPV	Organic photovoltaics
p-value	Dispersion parameter of constant phase element
p-Si	Polycrystalline silicon
PbI_2	Lead(II) iodide
PCE	Power conversion efficiency
PSC	Perovskite solar cell
PT	PEDOT:PSS/poly-TPD device
PTm	PEDOT:PSS/modified poly-TPD device
PX	PEDOT:PSS-only device
PV	Photovoltaics
QCM	Quartz crystal microbalance sensor
R_{HF}	High-frequency resistance
R_{LF}	Low-frequency resistance
R_{rec}	High frequency recombination resistance
R_{REC}	Total DC recombination resistance
R_{sh}	Shunt resistance
SEM	Scanning electron microscopy
TCO	Transparent conductive oxide
V_{OC}	Open circuit voltage

CHAPTER 1

INTRODUCTION

The concept of sustainability has become a significant focus of attention in recent years, particularly due to the increase in economic and environmental awareness. Providing sustainable energy is one of the main aspects of sustainable development. In this context, fossil fuels, which constitutes approximately 80% of the energy consumption worldwide, pose an issue of instability: They are limited and stored unevenly under the Earth's surface [1]. Rapid consumption of fossil fuels will result in the depletion of energy resources that further promotes energy insecurity [2]. Another major concern is the adverse effects of carbon dioxide emission on the environment, as a byproduct of fuel combustion. In order to address these problems, alternative sustainable energy sources are being investigated and studied now more than ever. These alternatives include geothermal, hydro, nuclear, solar and wind. The utilization of sustainable and renewable energy technologies in cooperation might provide the solution to critical energy issues that will be faced in the future.

Considering the subject matter of sustainable energy, the development potential for solar energy is notable by being the most abundant form of accessible energy. From photosynthesis to weather patterns, the Sun is the source of most, if not all, natural processes. Production of electricity from solar power is divided to two main types: photovoltaic (PV) and thermal. Photovoltaics employs the direct conversion of light into electricity, whereas thermal approach uses solar heat to generate electricity. PV industry distinguished itself by growing rapidly. With a growth factor of 57 over the time period from 2000 to 2015, solar PV capacity is increasing exponentially thanks to the economic incentives and advances in technology [3].

The elementary unit of a PV system is the solar cell. History of the solar cells dates back to 1839, when E. Becquerel discovered PV effect [4]. Then, the first solid state PV cell was built in 1883 by C. Fritts [5]. Finally, the first practical p–n junction solar cell made of silicon was demonstrated by the Bell Laboratories in 1954 [6]. Initially appealed to the niche market of space industry, solar cells attracted extensive investments and created a sizable industry, with price reductions and the development of the integrated circuit (IC) technology. Now, PV systems are regarded as one of the main rivals of conventional generation of electricity using fossil fuels.

1.1. Brief History of Solar Cells

As the history of the solar cells are summarized, it is customary to divide the technology to generations. In Figure 1.1, three generations of solar cell technology are depicted with their significant members.

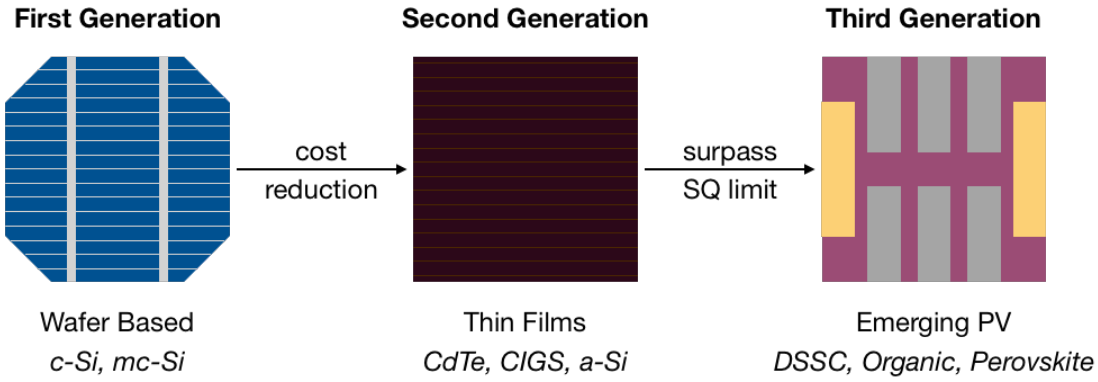

Figure 1.1. *Three generations of photovoltaics*

1st generation solar cells are p–n junctions based on silicon wafers and include single-crystal silicon (c-Si) and multi-crystalline silicon (mc-Si) cells. Silicon solar cells dominate the PV market with 95% share [7]. The manufacturing tools and processing know-how provided by the IC industry assisted the rise of silicon PV [8]. However, high expenses associated with the high-grade silicon wafers resulted in a search for solar cells employing less materials. Then, thin-film p–n junction devices emerged in the field.

2nd generation technologies aim to reduce the cost associated with the material manufacturing while maintaining the efficiency of the 1st generation PV [8]. While doing so, the pay-back time of the PV systems were aimed to be reduced. Due to the indirect bandgap nature of crystalline silicon, absorber thickness is quite large. In order to use less material, direct bandgap semiconductors are used in the 2nd generation PV: Cadmium telluride (CdTe) and copper indium gallium selenide (CIGS) are examples of thin-film absorbers of this generation. In addition to the less material usage, roll-to-roll fabrication is available for thin-film case. This is a strong advantage considering the rather slow and tedious process of silicon wafer production. In consideration of aforementioned arguments, thin-film PV systems hit the market. However, silicon PV firmly dominates the market and thin-film PV holds a share of ~5% currently [7]. It should be noted that silicon based 2nd generation devices such as amorphous silicon (a-Si) and polycrystalline silicon (p-Si) might prove the true potential of thin-films representing the marriage of silicon industry and thin-film PV.

Another side of this story of reducing cost per power is to increase the power through increasing the efficiency of solar modules. The record solar to electrical power conversion efficiency (PCE) of single p–n junction silicon is about 26% [9]. Considering the maximum attainable single junction PCE of ~32% for silicon (see Shockley–Queisser limit [10]), efficiency is about to be saturated. At this point, researchers started exploring other means of increasing efficiency and surpassing the Shockley–Queisser limit: multi-junction, hot-carrier, impurity photovoltaics, to name a few [11]. Solar PV research employing these techniques are classified as 3rd generation. Through the discovery of the potential of the organic PV (OPV) materials, a subsidiary of 3rd generation technologies, named as emerging PV, has been defined. Especially, utilization of OPVs spurred interest in the scientific community due to organic materials' potential to be significantly inexpensive. In addition, another type of solar cell called dye-sensitized solar cell (DSSC) was introduced. DSSCs presented some noteworthy features: fabrication by printing and roll-to-roll, semi-transparency for rather cosmetic functions such as architectural integration. Further, DSSC technology had a commercial success (see the company, GCell [12]), although it was quite limited. The newest member of the emerging PV technologies is the organic–

inorganic hybrid perovskite (OIHP) materials. They were discovered as a sensitizer PV material in a DSSC application in 2009 [13]. In 2012, OIHPs proved to be working with a solid hole conductor, without the need of a DSSC architecture and sensitization concept [14]. Subsequently, researchers from DSSC field have transferred their know-how and efforts to the perovskite materials and the OIHP PV research boomed. PCE values have escalated rapidly, from a mere 3.8% to the current value of 23.3% [9]. At the present day, OIHP materials and their applications in optoelectronics and PV are among the most studied topics in the research community.

1.2. Perovskite Photovoltaic Materials

Perovskite is a specific crystal structure of certain compounds. The mineral calcium titanate ($CaTiO_3$) was discovered in 1839 and named after the mineralogist L.A. Perovski [15]. Due to its distinctive lattice, this mineral gives its name to a class of crystal structures: perovskites. The general chemical formula of perovskite structure is ABX_3. The unit cell of the crystal structure is shown in Figure 1.2.

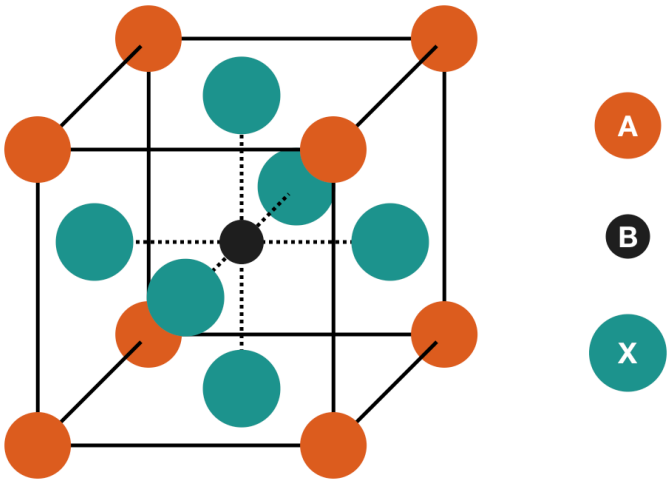

Figure 1.2. *Crystal structure of perovskites: ABX_3*

For the archetypal PV perovskite material, A cation is methylammonium ($CH_3NH_3^+$, i.e. MA^+), B cation is lead (II) ion (Pb^{2+}), and X anion is iodine (I^-). This

semiconducting $CH_3NH_3PbI_3$ (i.e. $MAPbI_3$) compound is the most studied perovskite having a favorable direct bandgap of ~1.55 eV for PV applications.

Perovskite crystal structure can be formed with ions of different radii. Such flexibility of crystal structure allows for a wide spectrum of perovskite compounds. In addition to $CH_3NH_3PbI_3$, A site can be formamidinium ($HC(NH_2)_2^+$, i.e. FA^+) and cesium ion (Cs^+), B site can be tin (II) ion (Sn^{2+}) and X site can be a halide (Cl^-, Br^-, I^-). Mixtures of those constituents are also available, making compounds of type $Cs_x(MA_pFA_{1-p})_{1-x}PbI_{3-y}Br_y$ a possibility with different optoelectronic properties. The optical bandgap of the base perovskite $MAPbI_3$ is around 1.5 eV with valence band maximum of –5.4 eV and conduction band minimum of –3.9 eV [16]. As the $MAPbI_3$ is doped with bromine (Br^-), yielding $MAPbI_{3-x}Br_x$, the bandgap shifts up to 2.3 eV gradually. This tunability of the bandgap enables OIHPs to be used in multi-junction solar cell applications.

Table 1.1.
Selected optoelectronic properties of perovskites and other PV technologies

Photovoltaic Technology	Power Conversion Efficiency* [%]	Bandgap [eV]	Absorption Coefficient [cm^{-1}]	Diffusion Length [µm]	Carrier Mobility [$cm^2V^{-1}s^{-1}$]	Carrier Lifetime
c-Si	26.7 ± 0.5	1.1	10^2	100–300	$10–10^3$	5 ms
GaAs	28.8 ± 0.9	1.4	10^4	1–5	$>10^3$	50 ns
CIGS	22.9 ± 0.5	1.1	$10^3–10^4$	0.3–0.9	$10–10^2$	250 ns
CdTe	21.0 ± 0.4	1.5	10^3	0.4–1.6	10	20 ns
Organic	11.2 ± 0.3	1.6	$10^3–10^5$	0.005–0.01	$10^{-5}–10^{-4}$	10–100 µs
Perovskite†	20.9 ± 0.7	1.6	$10^3–10^4$	0.1–1.9	$1–10^2$	0.1–1 µs

(Reproduced from [17], an Open Access article, Creative Commons Attribution license. Updated with recent improvements from *[18], †[19], [20])

Other than having a direct and tunable bandgap [21], OIHP materials have multitude of attractive properties such as high absorption coefficient [14], long carrier diffusion lengths [22], [23] and mobilities [24], [25], and long carrier lifetime [25] values. Typical values for these optoelectronic parameters of OIHP materials are given in

Table 1.1 along with the comparison between perovskite and other prominent PV technologies.

$MAPbI_3$ and $MAPbI_{3-x}Cl_x$ perovskites exhibit balanced charge transport properties such that carrier mobility values for electrons and holes are similar. In other words, OIHPs are able to transport both electrons and holes due to their ambipolar charge transport nature. Due to this ambipolarity, along with other intriguing features that will be discussed later, perovskite solar cells (PSC) needs different designs and architectural modifications compared to its base technology of DSSCs and conventional p–n junctions [26].

1.3. Structural Evolution of Perovskite Solar Cells

In contrast to the conventional oxide perovskites, the organic functional group in the A-site of the crystal structure renders OIHPs solution processable [27]. This solution processability made study of OIHPs available to most and inexpensive, and boosted the research of perovskites. At this point, it is convenient to depict the history of OIHP materials as the structural evolution of PSCs since it will provide with a sound understanding of OIHP materials' characteristics. More comprehensive historical narrative can be found elsewhere: [28]–[30].

Structural evolution of PSCs is given in the Figure 1.3 schematically. These structures are composed of glass as the substrate, transparent conductive oxide (TCO) as the bottom electrical contact, electron transport layer (ETL) and hole transport layer (HTL) as the carrier selective materials, perovskite as light harvester, and metal as the top contact. ETLs are low work function materials where HTLs have high (or deep) work function values. Typically, indium tin oxide (ITO) and fluorine doped tin oxide (FTO) are used as bottom contact TCO, titanium (IV) oxide (TiO_2) is used as ETL, an organic p–type material of spiro-OMeTAD is used as HTL whereas $CH_3NH_3PbI_3$ is employed as the perovskite absorber. Top contact is usually a metal, and aluminum, gold or silver is commonly used.

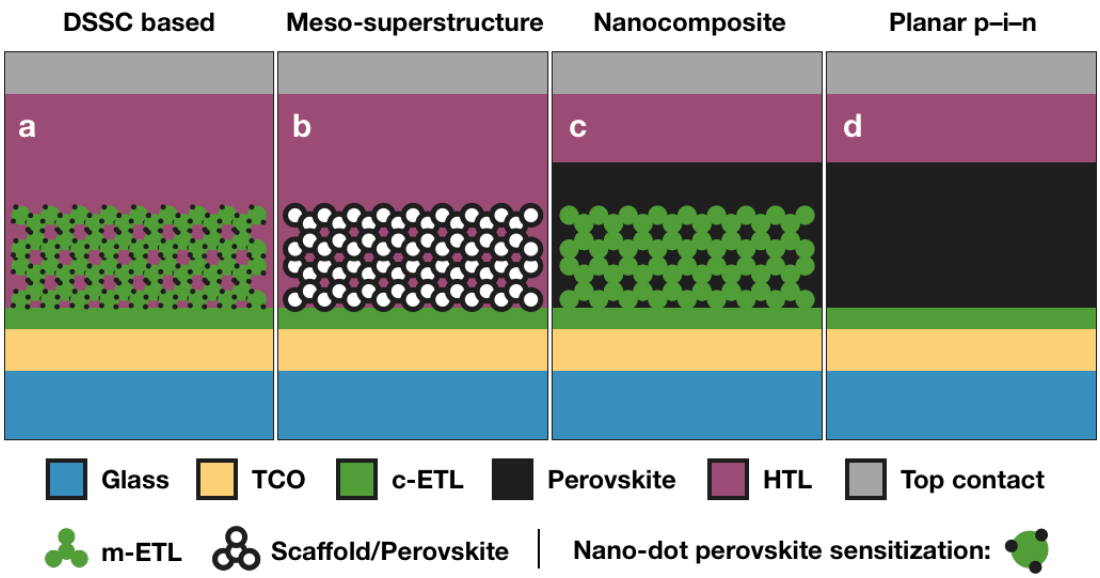

Figure 1.3. *Schematics of structural evolution of perovskite solar cells: (a) DSSC-based, (b) meso-superstructured, (c) nanocomposite type and (d) planar p–i–n*

First significant use of perovskite as the PV active material was presented in 2009 [13]. In this DSSC concept show in Figure 1.3a, perovskite light harvester was acting as a sensitizer material: Bound electron–hole pairs (i.e. excitons) generated in the dye sensitizer (here perovskite nano-dots) is separated by ETLs and HTLs. After the excitons are separated in the vicinity of ETL/perovskite and HTL/perovskite boundaries, electrons and holes are transported through the carrier selective layers. And finally, charge carriers are extracted from the metal top contact and TCO bottom contact, to drive an external load. Deviation from this DSSC-based concept was observed when the mesoporous ETL (m-ETL, an absorbent, sponge-like network) was replaced by an insulating scaffold of aluminum oxide (Al_2O_3) [14]. Having observed similar efficiency values of ~10% in these meso-superstructured cells, it was shown that perovskite $CH_3NH_3PbI_3$ itself is able to transport electrons up to the compact ETL (c-ETL) surface [28]. Al_2O_3 scaffold was merely a frame onto which perovskite is adsorbed (see Figure 1.3b). This observation is one of the most significant findings in the history of PSCs [30]. Later, m-ETL were infiltrated completely by the perovskite as shown in Figure 1.3c. Achieving PCE of 12% [31] in this nanocomposite structure confirmed that $CH_3NH_3PbI_3$ is also able to transport holes sufficiently—leading to the conclusion that $CH_3NH_3PbI_3$ shows ambipolar transport characteristics. Since the use of m-ETL is not mandatory, heterojunction p–i–n structure given in Figure 1.3d can

be fabricated. Here intrinsic perovskite is sandwiched between an n-type ETL and a p-type HTL in a planar architecture. This structure is quite different than the base technology of DSSC and possibly falls somewhere near conventional p–i–n solar cells such a-Si. A study employing ~300 nm thick $CH_3NH_3PbI_{3-x}Cl_x$ in a planar p–i–n configuration with a PCE of over 15% is of particular interest: While showing that nano-structuring is not necessary for high efficiency, perovskite absorber is vacuum deposited for the first time in the literature [32].

Discussion on the structural evolution of PSCs strongly suggests that perovskites should be considered as a distinct PV technology that deserves special attention. Although efficiency values had exceeded 20% in a very short time, the understanding of the device physics and operation principles is not developed sufficiently.

1.4. The Scope of the Thesis

The main focus of this thesis is the electrical characterization of PSCs by impedance spectroscopic techniques. Driven by the purpose to contribute to the understanding of device physics, impedance measurements on nickel oxide-based PSCs were made.

Chapter 2 establishes the necessary theoretical framework on properties of OIHPs, electrical basics of solar cell operation and impedance measurements, and impedance data analysis. Fabrication procedures and measurement methods are detailed in Chapter 3. In order to resolve the discrepancies encountered in the efficiency measurement of perovskite devices, different measurement techniques are evaluated in Chapter 4. Details on a designed maximum-power-point tracking system were given as well. Chapter 5 and 6 comprises the bulk of this thesis. In Chapter 5, impedance modelling of PSCs was carried out through the analyses of impedance responses of the devices. More concentrated analysis on the effects of different interlayers in nickel oxide-based PSCs is presented in Chapter 6. With a special emphasis on the underlying recombination channels, relevant discussion on the impedance responses were made. Thesis is concluded by final remarks and a future outlook is provided in Chapter 7.

CHAPTER 2

THEORETICAL BACKGROUND

In this chapter, informative background on various subjects is provided. After the summary of physical characteristics of organic-inorganic hybrid perovskite materials, several matters regarding the properties of perovskites are discussed as they will be referred to in the analyses in subsequent chapters. Electrical basics covering the operation of solar cells and impedance measurements are included as well. Finally, the theory and method connected to the analysis of impedance data through fitting to equivalent circuits are presented.

2.1. Physical Characteristics of Perovskites

Organic-inorganic hybrid perovskites (OIHP) have numerous optoelectronic properties that are favorable for photovoltaic applications. Some of these properties are summarized in Table 1.1 and explained in this section in more detail. For a PV material, properties regarding the light absorption, charge generation, and carrier transport composes the fundamentals of device operation.

Bandgap of photovoltaically appealing OIHPs typically ranges from 1.4 eV to 2.3 eV [33]. This wide range is achieved through a compositional engineering such that different combinations of ions results in perovskite mixtures. Bandgap of 1.4 eV is obtained in formamidinium-based $FAPbI_3$, and 2.3 eV corresponds to bromine-based $MAPbBr_3$. For the conventional perovskite of $MAPbI_3$, ~1.55 eV bandgap is commonly observed. Although bandgap of 1.55 eV is suboptimum (according to Shockley–Queisser limit of 1.4 eV for the highest efficiency) its ease of fabrication

and availability made $MAPbI_3$ the most studied OIHP material. $MAPbI_3$ absorbs photons up to ~800 nm very efficiently.

As an important point, the thickness of the absorber layer in a solar cell are subject to two competitive processes. The absorbed portion of light in the absorber increases with its thickness. But at the same time, extraction probability of charge carriers, and hence the collection efficiency decreases. This trade-off is strongly related to discussion on charge generation and carrier transport of solar cells in general. Typical perovskite layer thickness is about 300–500 nm although values up to 1μm were shown to be working efficiently [34]. This is probably due to the suppressed carrier recombination thanks to engineering of transport layers and possibly to vacuum deposition technique itself.

High absorption coefficient of OIHPs allows for devices having absorber thickness of >250 nm to have high efficiency values over 15% [35]. OIHPs exhibit optical absorption coefficients of $\sim 10^5$ cm^{-1} in the visible range, outperforming GaAs [36]. It should be noted that values of $\sim 10^4$ cm^{-1} was given in Table 1.1 is for near band edge absorption. Such high absorption coefficients were ascribed to orbital transitions of *s* and *p* of Pb atom [36], [37]. Also, strong photon absorption is intuitive since OIHPs have direct bandgap nature.

Regarding the origin of charge generation, it is important to point out that OIHPs are composed of two parts: organic and inorganic, as the name suggests. Due to this hybrid nature, charge generation mechanism can initially be thought as either excitonic or free carrier generation, like in the organic solar cells or inorganic counterparts. Yet their non-excitonic properties were revealed by findings of very small exciton dissociation energy [38], and also by showing the domination of free charge carriers in the operating conditions [37], [39]. Overall, OIHPs can be treated like inorganic semiconductors of non-excitonic nature.

For the carrier transport properties, ambipolarity of OIHPs has been pointed out previously. Perovskites' having ability to efficiently transport both electrons and holes

was reinforced with the findings of similar electron and hole effective masses (ranging from 0.1 to 0.3m_0) [36], [40], [41], leading to high mobilities. Thanks to their ambipolar carrier transport and high mobility of carriers, OIHPs are efficiently employed in p–i–n heterojunction solar cell architectures.

Another point that should be discussed is the doping of OIHP materials. Doping of materials are strongly correlated with their electronic properties. Internal electronic dynamics, from carrier concentrations to resultant recombination processes, are determined by the doping in a semiconductor. In order to establish an understanding regarding a particular semiconductor technology and optimizing device performances accordingly, proper doping control is necessary. However, the case for perovskites is rather complex, or at least, a complete picture is not provided yet.

Carrier concentrations are shown to be connected to the composition of precursors and fabrication conditions through self-doping in perovskites [42]. For $MAPbI_3$ perovskite fabricated from PbI_2 and MAI, MAI-rich deposition conditions results in p-type behavior while stoichiometry of excess PbI_2 (in addition to strong annealing that drives off MAI) causes n-type doping. Although this behavior is generally accepted, dependence of doping on minute details of fabrication is fairly possible. In addition, instability of OIHP materials might change the doping of perovskites. (When left in ambient conditions without proper encapsulation, PSCs typically degrade to yellow colored PbI_2). Furthermore, doping throughout the absorber layer is not uniform as it is pointed out in the subsequent discussion on ion migration. Additional studies regarding the doping should be made in order to understand the doping mechanisms in perovskites.

2.2. Recombination and Defect Tolerance of Perovskites

Recombination in solar cells is an important process having fundamental significance. Radiative recombination by itself is the result of photon absorption phenomenon in a solar cell, and hence is unavoidable and indeed necessary. But addition of non-radiative recombination channels decreases the performance of the device, especially

the open-circuit voltage. The reason for this is the diminution in quasi-Fermi level separation due to reduced steady-state free charge densities caused by non-radiative recombination—particularly, if these additional channels are faster than radiative recombination.

OIHPs are renowned for their defect tolerant nature, especially of native point defects. Obtaining high efficiencies in devices fabricated by using suboptimum solution processing, in a relatively short time, has ascribed to the tolerance of perovskites to intrinsic defects. Minor effects due to deviation from stoichiometric composition of precursor materials on the performance of devices also supported this point of view. It is generally agreed upon that intrinsic point defects that causes creation of deep trap levels have high formation energies so that they are unlikely to affect the device performance severely [43]. Yet, non-radiative recombination seems to be prominent in OIHP materials, as evidenced by electroluminescence response of them [44]. Here, Shockley-Read-Hall (SRH) recombination, which is through defects, has shown to be dominating. When considering the polycrystalline structure of OIHPs featuring grain boundaries, and possibly unpassivated surfaces, domination of recombination through defects is trivial.

There are other points of discussion regarding the recombination mechanisms and charge transport properties in perovskite solar cells (PSC) and OIHPs in general. Comprehensive reviews can be found in [37], [43], [45].

2.3. Ion Migration and Hysteresis

Hysteresis is simply defined as the dependence of the condition of a system on the history of itself; or, by considering its etymology, as a phenomenon in which the value of a parameter lagging the cause of the change associated to it. PSCs generally exhibit hysteresis in their I–V curves. The overall shape of the I–V curve changes as the scan direction of voltage is changed. Also, conditions prior to the measurement affect the curve: These include light-soaking, pre-biasing, or both of them at the same time. One question regarding hysteresis is whether the resultant I–V curve represents the steady-

state response of the cell or not. Typically, they are not representative of the steady-state response. Extensive care should be taken when evaluating a major figure of merit of solar cells, namely the power conversion efficiency, in aforementioned situations.

Underlying reasons of hysteresis in PSCs have been a topic of interest in the perovskite community. In general, arguments behind this phenomenon can be listed as [46], [47]: i) migration of mobile ionic species, ii) slow filling and emptying of density of states near the interfaces, and iii) slow polarization due to ferroelectricity, although the last item shown to be unlikely [48]. In this thesis, ion migration was emphasized since it explains the features observed in impedance measurements.

The first demonstration of ion migration was done through the presentation of switchable PV effect [49]. In this study, cycling poling of perovskite devices made from unselective contacts exhibited PV characteristics in opposite quadrants of I–V curve, depending on the previous poling voltage. This is well explained by the formation of p–i–n junctions in an otherwise symmetric device, through the doping effect caused by migration of ionic species (or ion vacancies). In addition, substantial band bending caused by ion accumulation was shown as in [49], [50].

Aforementioned p–i–n junction formation can describe the hysteresis phenomenon in PSCs: Typically, scanning from voltages corresponding to open-circuit to short-circuit (i.e. reverse scan) results in a sharper I–V curve compared to the opposite (i.e. forward scan, see Figure 4.1). Initially applying high voltage would result in a redistribution of ions by acting against the built-in voltage in the structure. Positively charged mobile ions drift to p-side (HTL) doping it further, and vice versa for the n-side (ETL). In this way, such an additional electric field promotes the charge extraction by the contacts. Therefore, I–V curve obtained by reverse scan *provides* with better efficiency values. Note that this situation by no means imply the true steady-state efficiency, which is also the case for forward scan. An elaborate discussion on efficiency measurements is presented in Chapter 4.

More interesting feature associated with mobile ions, as in the context of this thesis, are their effect on impedance measurements. In fact, prominent low-frequency features observed in impedance spectra are most probably due to the response of the mobile ionic species to external voltage perturbation. Owing to their sizes compared to electrons, they are expected to respond to applied electric field much slowly—as also evidenced by the I–V measurements carried out on the order of seconds. Thus, at high frequencies they cannot keep the pace with electric field, and they virtually freeze. But in low-frequency regime, their response can be observed. Eventually, low-frequency response of perovskite devices will be discussed by taking ionic motion into consideration.

2.4. Other Issues

Having provided the favorable properties of OIHPs, the open issues should also be mentioned. Instability of perovskites is a major concern that creates suspicion on whether they can endure the stringent conditions of PV electricity generation. Perovskite materials easily degrade to their precursors when they contact with polar materials such as water [51]. Elevated temperatures and humid conditions readily increases the rate of degradation [52]. Ionic migration can also facilitate the degradation by creating zones of volatile non-stoichiometric composition—MAI itself can degrade to its constituents of volatile nature: hydroiodic acid HI and methylamine CH_3NH_2.

Another issue related to perovskites is the toxicity associated to lead (Pb). As a byproduct of decomposition of perovskite, PbI_2 is regarded as a carcinogenic compound in addition to its threat to the environment [28]. Proper encapsulation techniques to contain the toxic materials and to passivate the degradation mechanisms are needed in the longer term in order for the PSCs to compete with the existing PV technologies.

2.5. Electrical Basics of Solar Cells

Solar cell is simply an asymmetric device that extracts light-generated carriers through its contacts eventually to drive an outer load. The asymmetry built inside the solar cells is what selectively extracting hole and electrons before they recombine with each other. Archetypically, they are p–n junctions. A schematic diagram of a p–n junction solar cell is given in Figure 2.1 along with its equivalent circuit model.

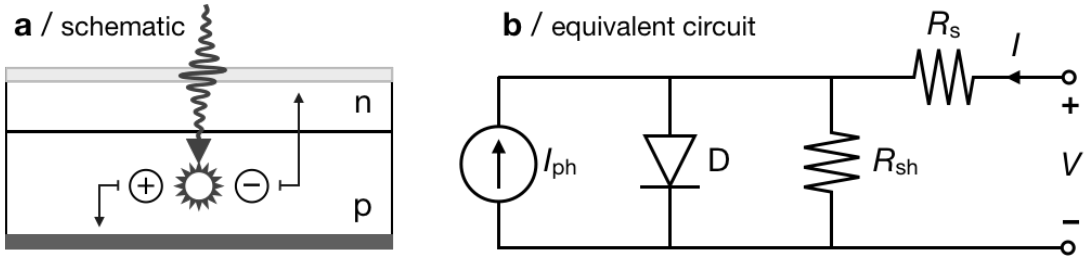

Figure 2.1. *A schematic diagram (a) and the equivalent circuit (b) of a p–n junction solar cell. I_{ph}: light-generated current; D: diode, R_{sh}: shunt resistance, R_s: series resistance*

Using the ideal diode equation, the current–voltage relation for a p–n junction solar cell can be written as follows:

$$I = I_0 \left[\exp\left(\frac{qV}{mk_B T} \right) \right] - I_{\text{ph}} \tag{2.1}$$

where I is the current through the terminals across which voltage V is generated, q is elementary charge, m is the diode ideality factor, k_B is the Boltzmann constant, T is the absolute temperature, I_0 is the diode saturation current, and I_{ph} is the light-generated current. This equation describes an addition of light generation current to the diode current expression in the dark. An equivalent circuit depicting this behavior is given in Figure 2.1b with modifications due to a pair of non-idealities: series resistance R_s and shunt resistance R_{sh}. These parasitic resistances are inherent in all solar cells and they affect the solar cells performance. Equation 2.1 can be modified by accounting for these resistances. A typical I–V curve of a solar cell is illustrated in Figure 2.2 for a PSC.

Solar to electrical power conversion efficiency (PCE), or simply efficiency, is regarded as a major figure of merit for a photovoltaic device. Efficiency, in simple terms, is defined as the ratio of electrical output power P_{OUT} to the incident solar power P_{IN}:

$$\text{Efficiency, or PCE} \equiv \frac{P_{\mathrm{OUT}}}{P_{\mathrm{IN}}} \tag{2.2}$$

The standardized solar irradiance spectrum for PV device efficiency measurements is denoted as AM1.5 (i.e. air mass coefficient of 1.5). This standard corresponds to an input power density of 1000 W/m^2 (or 100 mW/cm^2). By using P_{IN} = 100 mW/cm^2 in Equation 2.2 while correcting the output electrical power by the area of the device yields:

$$\%\ \text{Efficiency} = \frac{\max\ (JV)}{S_{\mathrm{eq}}} \quad [\%]$$

where J is current density in mA/cm^2, V is the electrical potential in V, and S_{eq} is the equivalent amount of AM1.5 Sun irradiance. For instance, 900 mW/cm^2 corresponds to S_{eq} = 0.9.

Current–voltage characteristics (i.e. I–V curve) of a solar cell shows current passing through the device as a function of the voltage across its electrodes. Since electrical power equals voltage times current, it also shows the efficiency of the device providing input power is specified. Therefore, an I–V curve can be thought as an extension that presents additional performance parameters while showing the efficiency value.

Typical I–V curve for a perovskite n–i–p junction is given in Figure 2.2 along with associated output power density. Note that the reversed sign convention is used in this figure so that the generated power is positive. Here, input power is 850 mW/cm^2—resulting in S_{eq} = 0.85 and efficiency of 15%. Other additional performance parameters that can be extracted from the I–V curve are open-circuit voltage (V_{OC}), short-circuit current (J_{SC}) and maximum-power-point (MPP). MPP is the point at which JV, hence

the output power, is maximized. As a measure of the sharpness of the I–V curve, Fill factor (*FF*) is defined as:

$$\text{Fill Factor, } FF \equiv \frac{J_{\text{MPP}} V_{\text{MPP}}}{J_{\text{SC}} V_{\text{OC}}}$$

where J_{MPP} and V_{MPP} is current density and voltage at MPP, respectively. *FF* can also be visualized as the ratio of the area of the inner rectangle, defined by MPP and origin, to the area of the outer rectangle defined by J_{SC} and V_{OC}.

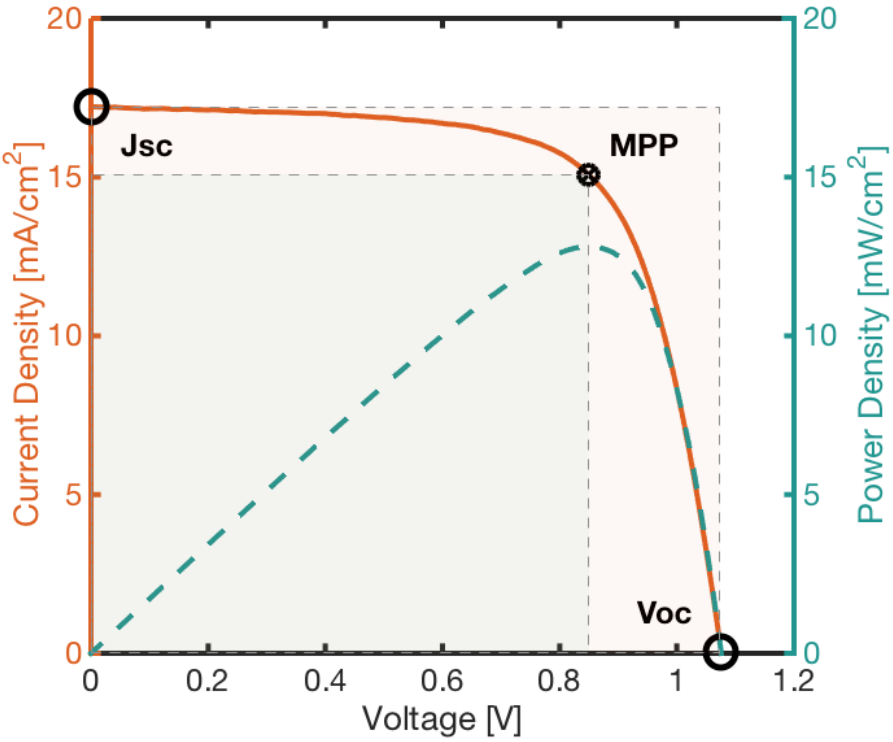

Figure 2.2. *Typical I–V curve of a perovskite solar cell*

An I–V curve is typically obtained by scanning the voltage across the device under test and recording the current at each voltage increment. At each voltage, some amount of time is spent, i.e. dwell time, so that the current stabilizes [53]. Regularly, response time of a PV device is in the order of µs to ms like c-Si solar cells so that they allow for fast I–V curve scans (or even pulsed measurements). Furthermore, it is expected

that the results do not depend on the history of the device such that there is no need for pre-conditioning. In that case, I–V curves associated with them represent their true steady-state performance. Yet, the case is quite complicated for PSCs as it is elaborated in Chapter 4.

2.6. Basics of Impedance

Impedance (Z) is defined as the ratio of voltage and current, and in general, complex valued so that it relates the sinusoidal output current to the sinusoidal input voltage applied on a system:

$$Z \equiv \frac{V}{I}$$

Sinusoidal voltage (v) and current (i) can be represented in cartesian form as well as in polar form. In time domain, following convention can be implemented:

$$v(t) = V_{\mathrm{DC}} + v_{\mathrm{ac}} \cos(\omega t)$$
$$i(t) = I_{\mathrm{DC}} + i_{\mathrm{ac}} \cos(\omega t - \phi)$$

In these expressions, V_{DC} is the DC bias, I_{DC} is the DC current, v_{ac} is the amplitude of the sinusoidal voltage, i_{ac} is the amplitude of the sinusoidal current, ω is the radial frequency, ϕ is the phase shift angle (with convention of negative for leading current). In phasor domain, impedance Z and its inverse, admittance Y can be written in both polar and cartesian form as:

$$Z = |Z|e^{j\phi} = R + jX$$
$$Y \equiv Z^{-1} = |Y|e^{-j\phi} = G + jB$$

where R is resistance, X is reactance, G is conductance, and B is susceptance. Note that the magnitude of Z is $|Z| = v_{\mathrm{ac}} / i_{\mathrm{ac}}$. Having defined necessary parameters, basics of impedance measurement will be given.

When a system (e.g. a device) is excited by a sinusoidal ac voltage, current passes through it will also be a sinusoidal if the system is linear. Resistors, capacitors and inductors are ideally linear, yet diodes are nonlinear devices. Since a solar cell is virtually a diode, its behavior is also nonlinear. Therefore, response of a solar cell to an alternating voltage is not necessarily linear. However, by imposing a *small* voltage, their behavior can be linearized around their DC operating point (I_{DC}, V_{DC}). By this way, their complex nonlinear behavior can be analyzed. Graphical representation of aforementioned application is given in Figure 2.3. An input signal $v(t)$ and the associated output current $i(t)$ are illustrated in time domain in Figure 2.3a. Note that DC voltage level is taken as zero in Figure 2.3a for convenience.

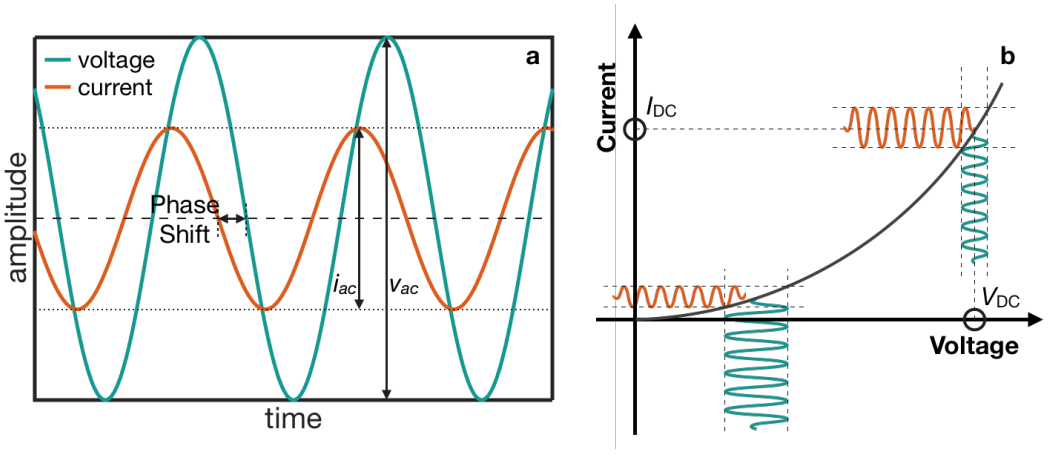

Figure 2.3. *Measurement of complex impedance in time domain (a) and linearization of the response on I–V characteristics (b)*

Small-signal linearization assumes local linearity over the operating point. Hence, selection of voltage amplitude v_{ac} is critical. For instance, a lower amplitude was chosen in Figure 2.3b for V_{DC} lies on the right-hand side (high V_{DC}) than the one in the left-hand side (low V_{DC}) for preserving linearity over a fast-changing $i(v)$ as its higher derivatives becoming more prominent. Overall, impedance measurements techniques, impedance spectroscopy (IS) in this case, provide electrical characterization of devices by employing small perturbations of voltage. Additional DC voltage is added on this ac perturbation so that different operating points can be selected. For a solar cell, ac oscillation level of few mV should not be exceeded, especially in higher bias voltages where I–V curve bending is prominent.

2.7. Representation of Impedance Response and Equivalent Circuits

Typically, in impedance measurements, the impedance Z of the device under test (DUT) is measured at different frequencies f. There are various representations of the impedance data. If polar form variables ($|Z|$, ϕ) are used, a Bode plot can be employed so that the magnitude and the phase of the DUT can be plotted against the frequency. Or, in cartesian form, real (R) and imaginary parts (X) of the impedance, i.e. resistance and reactance, can be plotted against frequency. An example Bode plot and R, X vs. f plots are given in Figure 2.4, for a parallel connected resistor R_P and a capacitor C_P as shown as the inset with their values.

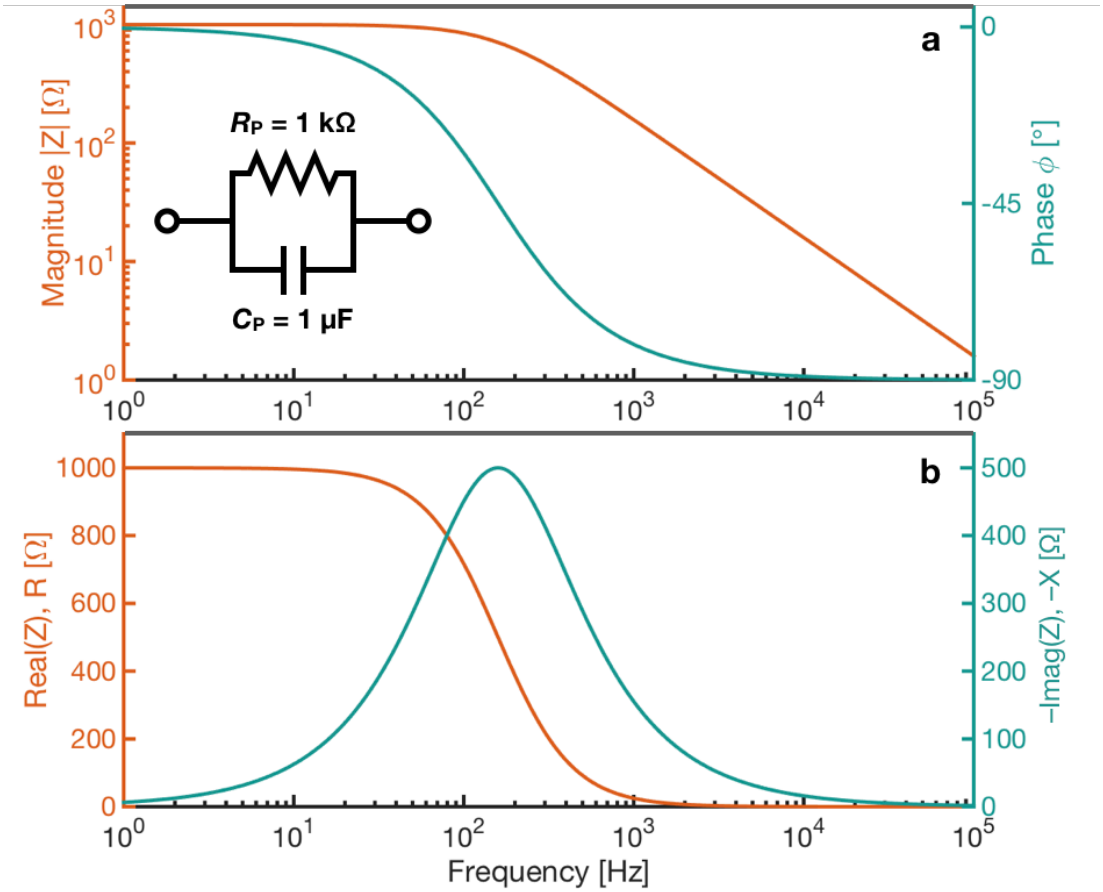

Figure 2.4. *Bode plot (a) and R, X vs. f plots (b) for an RC circuit*

Representation of impedance can also be made through vectors: In Nyquist plot, impedance at a point is given as a vector on polar coordinates of R and X, which are the real and imaginary parts of the complex impedance Z. Such plot of the previous

RC circuit is given in Figure 2.5. Values of $|Z|$, ϕ, R, and X for a random point were also depicted in this figure. Note that, the frequency information is lost in Nyquist plots. Yet, their use is quite valuable since they facilitate the recognition of different processes in a real system, which can be troublesome in impedance vs. frequency plots if the system is quite complicated. Using both type of data illustration techniques in conjunction provides with a strong understanding of underlying processes in a real and complex system, such as perovskite solar cells.

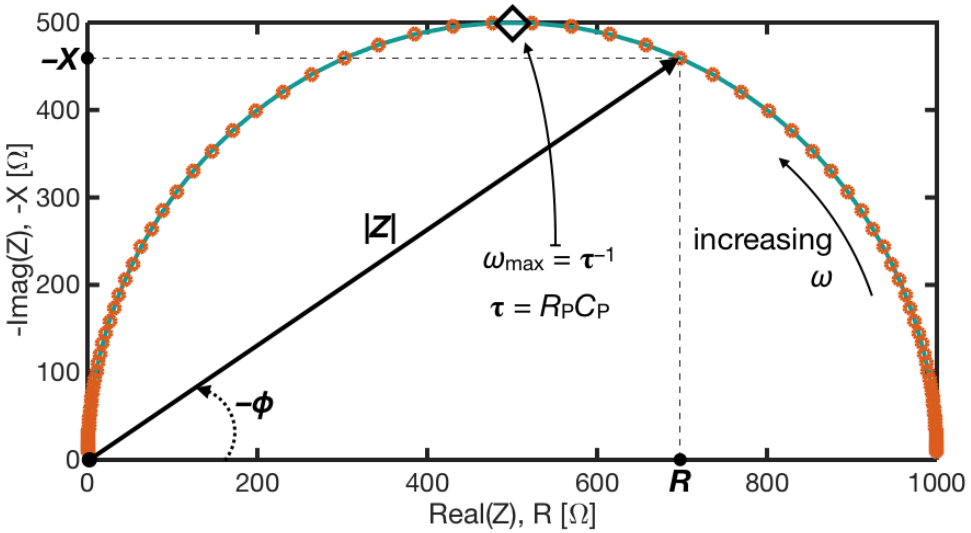

Figure 2.5. *Nyquist plot of impedance of a parallel RC circuit*

Number of different features are observed in Nyquist plots. First of all, parallel connected RC circuits results in semi-circles. This result agrees with the following observation: At low frequencies, impedance of a capacitor goes to infinity (since the complex impedance of a capacitor C is $Z_C = -j/\omega C$), and overall impedance goes to R_P. At high frequencies, capacitor acts as a short circuit, and Z goes to 0—crossing the origin. In a mid-frequency, RC circuit has a maximum X at $\omega_{max} = (R_P C_P)^{-1}$. This peak point in Nyquist plot corresponds to the time constant τ of a *process* in general. At this very case, that process is RC circuit charging and discharging.

Another point should be made in order to expedite the recognition of changing parameters by eye inspection. As the R_P increase, the diameter of the semi-circle increases, and vice versa. Change in C_P changes neither the diameter nor the shape. It

only translates the frequency range where X peaks ($\omega_{max} = (R_P C_P)^{-1}$). The peak value of X is equal to $-R_P/2$ and is independent of C_P.

In impedance measurements of real devices, a certain dispersion in frequency is often observed for capacitive responses. Such deviation from ideality reveals itself as the semi-circles in Nyquist plots gets depressed; in fact, semi-circles rotates clockwise around the origin. This nonideality might stem from some inhomogeneity such as fractal electrodes [54], although the reasons are mostly unknown. Historically, this deviation was interpreted as the dispersion in time constants of underlying processes as follows [55], in terms of admittance associated with them:

$$\text{Ideal: } Y_{RC} = \frac{1}{R_P} + \frac{j\omega\tau}{R_P} \quad \rightarrow \quad \text{Measurements: } Y_{meas} = \frac{1}{R_P} + \frac{(j\omega\tau)^p}{R_P} \tag{2.3}$$

where p is the power parameter of dispersion. Note that in ideal case $\tau = R_P C_P$ and Y_{RC} directly corresponds to the admittance of an RC circuit. This dispersion is then modelled by using a parallel connected resistance and a constant phase element (CPE). Admittance of the constant phase element is expressed as $Y_{CPE} = (j\omega)^p Q$ (it should be noted that for $p = 1$, CPE is simply an ideal capacitor). The dispersion model including CPE is given as follows [56]:

$$Y_{CPE||Rp} = \frac{1}{R_P} + (j\omega)^p Q \tag{2.4}$$

where Q is a parameter in unit of s^p.S (i.e. seconds^p.Siemens). Expression in the right-hand side of Equation 2.3 is equivalent to Equation 2.4 when $Q = \tau^p / R_P$ i.e. Y_{meas} is equal to $Y_{CPE||Rp}$. An equivalent capacitance C_{eq} can be defined so that $\tau = R_P C_{eq}$. Overall, C_{eq} can be expressed in terms of p and Q:

$$C_{eq} \equiv \frac{1}{R_P}(R_P Q)^{\frac{1}{p}} \tag{2.5}$$

It should be noted that this equivalent capacitance is the capacitance that would be obtained *if* the nonideality of dispersion was absent and $p > 0.75$ [55]. Hence, it is the main component that should be evaluated with respect to the changing conditions in IS.

Derivation given above was mostly performed according to [55]. For the sake of simplicity, the models of impedance will be shown with ideal capacitor symbol that corresponds to C_{eq} (if $p > 0.8$), throughout this thesis. But the fittings of the model were carried out with CPEs and the associated p-values were given when necessary.

When the dispersion parameter $p = 0.5$, CPE element models the diffusion process, and it is named as the Warburg element. This special case is commonly observed in electrochemical impedance spectroscopy by corresponding to the diffusion of ionic species in the solution. As the diffusion of ionic species also observed in mixed ionic–electronic conductors such as perovskites, this element might (and will) prove useful in the analysis of perovskite solar cells, as well.

2.8. Fitting of Impedance Response

In order to check the validity of proposed models and subsequently extracting the set of parameters of interest **P**, impedance data should be fit to the equivalent circuits of interest. Proper fitting procedure has utmost importance as a tool since it determines whether the impedance model is valid or not. Here, nonlinear least squares method was employed in order to fit the IS spectra obtained in the scope of this thesis.

Least squares method employs the minimization of the sum (S) of the square of residuals with respect to **P**. The term S can be thought as the error value representing the accuracy of the proposed model. Overall, the minimum of the sum is searched as:

$$\min_{\mathbf{P}}(S) = \min_{\mathbf{P}}\left\{\sum_{i} W_i\left[Z_i^{*\mathrm{E}}(\omega_i) - Z_i^{*\mathrm{M}}(\omega_i, \mathbf{P})\right]^2\right\} \tag{2.6}$$

where i is the index of data point, W_i is weighting parameters, $Z_i^{*\mathrm{E}}$ and $Z_i^{*\mathrm{M}}$ are the experimental and modelled impedance *functions* (yet to be determined), and ω_i is frequencies of measurements. Note that **P** is a vector containing different parameters such as series resistance R_s and geometrical capacitance C_geo. When using equivalent circuits, the real part of the impedance spectra completely defines the imaginary part and vice versa, if values at all the frequency range is known, and the system is stable, causal and linear—as a constraint stated by Kramers–Kronig relations [57], [58]. Therefore, either the real part (R) or the imaginary part (X) of the experimental and modelled impedance values can be used as impedance functions of $Z_i^{*\mathrm{E}}$ and $Z_i^{*\mathrm{M}}$, respectively. Yet, better approach would be to use them both in conjunction as the *separate* sum of them. This approach can be justified considering the dynamic behavior of R and X. There are cases where $R \gg X$, or $R \ll X$ that would otherwise causes poor fitting due to the finite precision of the impedance analyzer.

Another concern regarding the fitting procedure is the selection of weighting functions. There are cases where impedance Z is very large or small at certain frequency ranges, e.g. impedance is small at high frequencies since all capacitive components are shorted. In order to even out the contributions of different frequency ranges, weighting functions can be defined as the inverse squared of the magnitude of the impedance belonging to the model Z_i^{M} [59]. Finally, the minimization problem can be solved according to the following expression based on Equation 2.6:

$$\min_{\mathbf{P}} \left\{ \sum_i \frac{1}{\left| Z_i^{\mathrm{M}}(\omega_i, \mathbf{P}) \right|^2} \left[\left(R_i^{\mathrm{E}}(\omega_i) - R_i^{\mathrm{M}}(\omega_i, \mathbf{P}) \right)^2 + \left(X_i^{\mathrm{E}}(\omega_i) - X_i^{\mathrm{M}}(\omega_i, \mathbf{P}) \right)^2 \right] \right\}$$

where R_i^{E} and X_i^{E} are the real and imaginary part of the experimentally measured impedance, and R_i^{M} and X_i^{M} are the real and imaginary part of the impedance of the model. The minimization procedures were carried out by using the *fminsearch* function in MATLAB® [60] that employs simplex search method in [61]. Starting points of **P** is crucial in order for the solver to reach a meaningful minimum (the global minimum if it is physically valid). Hence, proper initial guessing regarding the parameters of the model necessitates *a priori* knowledge on the system. For instance,

it is known that the geometrical capacitance should be on the order of several 100 nF/cm^2.

After the fittings were done, the *goodness* of fit were checked each time by the adjusted coefficient of determination (R-squared) as given in [62]. Closeness to value 1 is indicative of a good fit. Addition of extra parameters to the model, and hence to the fit, were justified by checking the adjusted R-squared value to getting close to 1, by approximately an order of magnitude, at least. For instance, if R-squared = 0.990, addition of an extra parameter should increase it to around 0.999.

Another issue concerning proper fitting of IS spectra is the over-parameterization. Often, simple models are enough to explain the underlying physical processes, and any additional model parameters would complicate the evaluation of impedance data. Although the goodness of fit might improve, this might be an over-fitting—limiting the applicability and relevance of the proposed models to other sets of data and different PSC configurations. Therefore, proper care should be taken when modelling. Throughout this thesis, special effort was made to construct simple models that explains impedance response well enough.

CHAPTER 3

FABRICATION AND INSTRUMENTATION

This chapter provides the details of perovskite solar cell fabrication through the deposition of each layer. The electrical characterization techniques employed in the scope of this thesis are presented: current–voltage, efficiency and impedance measurements. The details of instrumentation and measurement conditions are included as well.

3.1. Structure and Fabrication of Perovskite Solar Cells

In this thesis, perovskite solar cells (PSC) of several different architectures were fabricated, characterized, and analyzed. All PSCs are planar p–i–n heterojunctions. Transparent conductive oxide (TCO) layers used in this study are either indium tin oxide (ITO) or fluorine doped tin oxide (FTO). For electron and hole transport layers (i.e. ETL and HTL), a number of different structures were used: fullerene-C_{60} as ETL, and PEDOT:PSS, nickel oxide (NiO_x) as HTLs. For top metal contact bathocuproine/silver (BCP/Ag) was used. There is also an interface layer of poly-TPD deposited in order to suppress surface recombination, or to improve band alignment. It is common practice to call the solar cell structure as *regular* when the deposition order of layers is ETL/perovskite/HTL, and *inverted* for the opposite, i.e. when the order is HTL/perovskite/ETL (in contrast to the use in organic photovoltaic technology, i.e. OPV). Here *n–i–p* and *p–i–n* will be used for ETL/perovskite/HTL and HTL/perovskite/ETL, respectively. The architecture of the PSCs fabricated is given in Figure 3.1a along with the layout of the substrates containing 6 individual cells, i.e. pixels, in Figure 3.1b. The active areas are shown in the figure by red

rectangles. Note that only n–i–p structure is depicted along with the device electrode polarity.

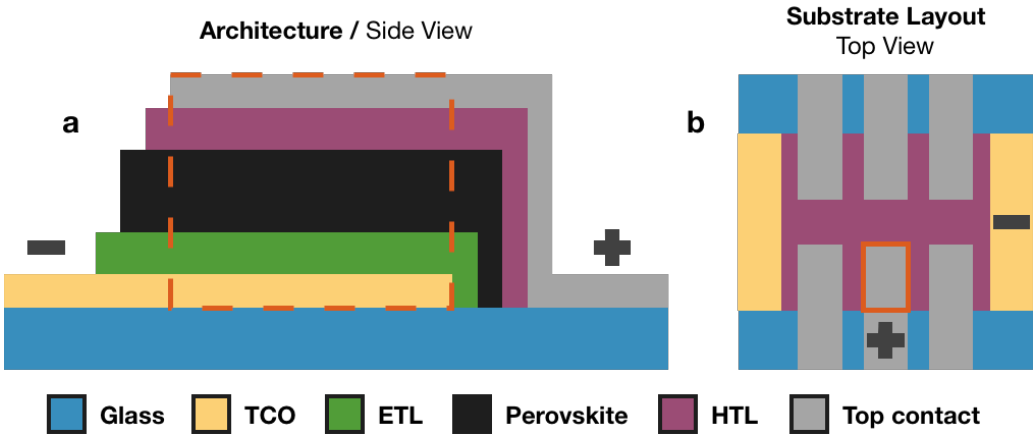

Figure 3.1. *The architecture (a) and layout (b) of an n–i–p perovskite solar cell*

The reaction takes place as the perovskite was formed is given as PbI_2 + MAI → $MAPbI_3$. Note that mixtures are possible such as $CH_3NH_3PbI_{3-x}Br_x$. The methods of perovskite film deposition are numerous—resulting in a polycrystalline layer. The simplest one is the direct (also known as one-step) spin-coating of perovskite precursor solution containing lead (II) halide (PbX_2), and methylammonium halide (MAX) where halide X = Cl, Br, I. The solution is prepared in a polar solvent such as N,N-Dimethylformamide (DMF). Another method employs a two-step approach: First PbX_2 is spin-coated onto the substrate, then MAX solution dissolved in an orthogonal solvent (such as 2-propanol, i.e. IPA) is either dip-coated or spin-coated as well. Availability of vacuum deposition also enables different approaches. Vacuum evaporation has obvious advantages over solution processing techniques. Films deposited using spin-coating are prone to exhibit pin-holes that potentially shorts the perovskite absorber. In addition, evaporated films tend to be denser and of uniform coverage. Co-evaporation of precursors PbX_2 and MAX, and evaporation of PbX_2 followed by spin-coating of MAX are among the vacuum methods. Latter is the method employed in this study. In this method, PbI_2 was deposited in a vacuum chamber by thermal evaporation. Then, MAX mixture of MA(I:Br:Cl) was spin-coated on the compact PbI_2 layer, followed by thermal annealing on a hot plate. Resulting perovskite structure is $CH_3NH_3PbI_{3-x}Br_x$(Cl)—where (Cl) denotes chloride doping

although Cl^- seems not to be incorporated into the perovskite layer [63]. The perovskite films deposition technique used in this study is depicted in the Figure 3.2 as it is the core of the fabrication of PSCs.

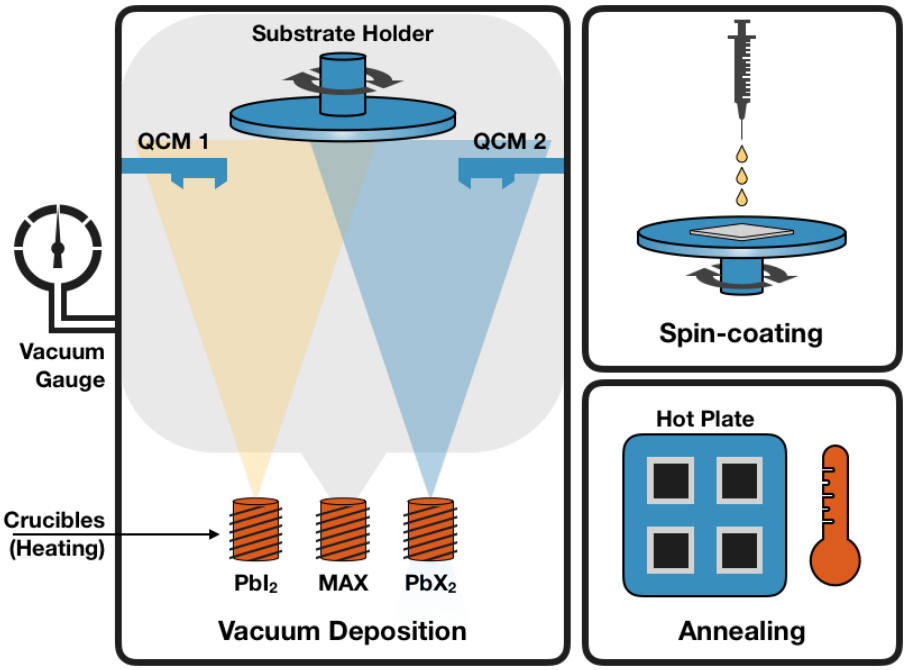

Figure 3.2. *Schematics of perovskite layer fabrication*

Vacuum deposition technique illustrated in Figure 3.2 deserves additional explanation. (Note that the operation of the perovskite vacuum deposition is given generically here, and all features and possibilities are not necessarily employed in the scope of this thesis.) The vacuum chamber that were used in this study has a diffusion pump that is backed up by a mechanical pump and can be evacuated up to ~10^{-6} Torr as the base pressure. It has 3 crucibles with resistive tungsten wire heating. Two of the crucibles were assigned to inorganic sources of lead halides PbX_2. The crucible in the middle is used for organic source of MAX, typically CH_3NH_3I. There are 2 quartz crystal microbalance (QCM) sensor that measures the mass deposited on them, and hence the rate of deposition. In order to control the deposition rates of different precursors, QCMs were placed at different positions with respect to the sources. Due to this asymmetry, properly tooled QCMs give the individual deposition rate of 2 inorganic sources. Inorganic sources follow ballistic evaporation such that they follow straight line from their source up to the substrates. On the other hand, MAX fills up the

chamber entirely as evidenced by the considerable increase in the pressure of the chamber (on the order of 10^{-5}). In fact, the deposition pressure is itself a control parameter relating to the amount of MAX when the co-evaporation approach is employed. Since the MAX fills up the chamber uniformly, they merely add a constant background noise to QCMs that is corrected readily.

The materials used for the fabrication of perovskite devices are given in Table 3.1 along with their properties of interest. Shown abbreviations are used throughout this thesis. Fabrication of each layer is given in detail, subsequently. All steps were carried out in ambient atmosphere.

Table 3.1. *Materials used in perovskite solar cell fabrication*

Material	Name	Doping	Type	Usage	Deposition Method
BCP	Bathocuproine	n	Small molecule	Contact interlayer	Evaporation
C_{60}	Buckminsterfullerene C_{60}	n	Small molecule	ETL	Evaporation
NiO_x	Nickel oxide	p	Oxide	HTL	Sputter
PEDOT:PSS	Poly(3,4-ethylenedioxythiophene)-poly(styrenesulfonate)	p	Polymer mixture	HTL	Spin-coat
poly-TPD	Poly[N,N'-bis(4-butylphenyl)-N,N'-bisphenylbenzidine]	p	Polymer	HTL / interlayer	Spin-coat

Substrate. TCO of ITO was patterned by etching. Approximately 15 Ω/sq. ITO coated glass was taped using acid-resistant tape to protect underlying areas. Zinc powder was spread on taped substrates. 2 M aqueous hydrochloric acid, HCl(aq) was dropped on the ITO followed by abrasion with a toothbrush. After rinsing with deionized (DI) water, tapes were removed. Patterned substrates were cleaned in toluene, Hellmanex™ detergent, DI water, acetone, and IPA, sequentially by using ultrasonic bath. Substrates were made ready for the deposition of subsequent layer after they were treated UV-ozone plasma for 10 minutes. This treatment makes the surface hydrophilic and free of organic residues.

NiO_x. Radio frequency (RF) magnetron sputtering was employed for the deposition of NiO_x HTLs. Argon was used as the sputtering gas. Deposition pressure and power were 30 mTorr and 120 Watts, respectively.

PEDOT:PSS. Heraeus Clevios™ Al 4083 dispersion was used after filtration by a 0.45 µm syringe filter. Then 50µL of PEDOT:PSS solution is dynamically spin-coated on TCO substrates at 6000 rpm for 40 seconds. Substrates were annealed on a hot plate at 110 ºC for 20 minutes in order to cross-link the polymers.

Poly-TPD. Typically, a thin interlayer of poly-TPD was spin-coated subsequently on hole transporting PEDOT:PSS to improve the hole extraction properties. Poly-TPD solution of 7 mg/mL prepared in anhydrous chlorobenzene was spin-coated on substrates at 3000 rpm for 30 seconds. When modified, in order to thin the layer down, substrates were spin-washed twice with 50 µL of chlorobenzene at the same run of spin-coater. Then, substrates were annealed on a hot plate at 130 ºC for 30 minutes, making them ready for perovskite deposition.

Perovskite. Unless otherwise stated, $CH_3NH_3I_{3-x}Br_x(Cl)$ perovskite absorber fabrication was carried out as follows: 220 nm of PbI_2 layer was deposited in vacuum of $2x10^{-6}$ Torr at a rate of ~2.5Å/sec. Then 50µL MAX solution, containing 35:10:5 mg of MAI:MABr:MACl in 1 mL anhydrous IPA, was spin-coated dynamically at 2000 rpm for 20 seconds after filtration by 0.2 µm syringe filter. Resulting films were immediately placed on hot plate at 100 ºC and annealed for 30 minutes. Finally, in order to clean the residual unreacted MAX agglomerates on the surface, 100 µL of anhydrous IPA was spin-coated on the perovskite layer at 4000 rpm. At this point, substrates were ready for subsequent ETL or HTL deposition.

A cross-sectional micrograph of a p–i–n perovskite solar cell obtained by scanning electron microscope (SEM) is given in Figure 3.3. Here, the structure is ITO / NiO_x / Perovskite / C_{60} / BCP / Ag. Note that C_{60} and BCP cannot be distinguished since they are too thin for this magnification. They simply lumped into top contact metal.

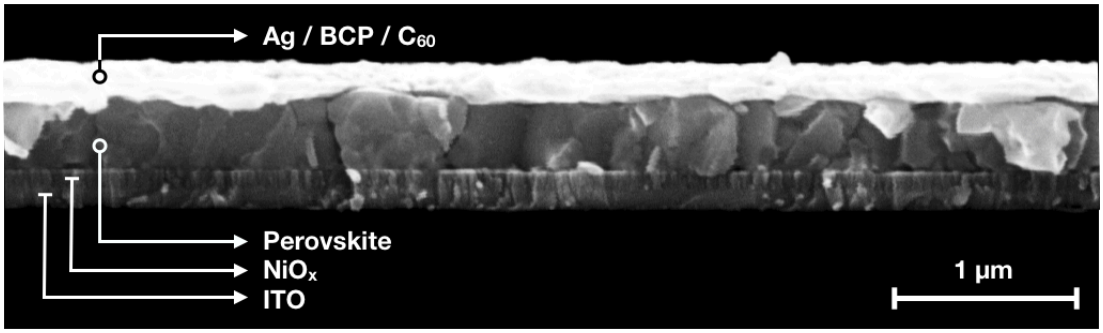

Figure 3.3. *An SEM micrograph of a perovskite solar cell*

C_{60}. Approximately 25 nm of C_{60} was deposited in the vacuum of $2x10^{-6}$ Torr at a rate of ~1Å/sec. The same vacuum chamber used for perovskite deposition was used by changing the evaporation crucibles.

Top metal contact. BCP was evaporated in a thermal metal evaporation system with a thickness of ~7 nm. Then metallization was completed with evaporation of Ag at a rate of <1Å/sec initially and up to 1Å/sec. About ~100 nm of Ag was deposited. When the cells were taken out of the metallization chamber, they have been annealed at 100 ºC for 10 minutes in order to improve the ohmic contact properties.

3.2. Current–Voltage Measurements

Current–voltage measurements were carried out with a Keithley 2400 Series source-meter that is controlled by a custom-made LabVIEW™ programs. Different DC I–V measurements of standard I–V scan, current and voltage monitoring at steady-state, dynamic I–V, and maximum-power-point tracking were all made in similar fashion.

For accurate efficiency measurements, Newport® Oriel Model 91192 solar simulator was used in conjunction with a calibrated silicon reference cell. Active areas were defined with laser-cut polycrystalline silicon masks of 1.5 mm^2 aperture. Aperture areas were corrected for laser kerf. Electrical contacts were made with alligator clips. 2-wire connection was used since the active areas of the cells and hence the orders of currents are quite small. Therefore, utilization of 4-wire setup was not necessary for I–V measurements.

Voltage is scanned from 1.2 V to –0.2 V for reverse scan, and exactly opposite for forward scan. Unless stated, voltage scan rate of 120 mV/sec was employed. Settling of the solar cell's response to the fast change occurring in initial voltage step was allowed for at least 1 second. Other than this, no pre-conditioning was applied on perovskite solar cells.

3.3. Impedance Measurements

Impedance measurements were conducted by an Agilent 4192A LF Impedance Analyzer for frequency ranges 10 Hz–1 MHz on a custom-made probe station supporting 4-wire measurement technique. Oscillation level of v_{ac} ~10 mVrms was used in order to ensure linearity. Measurements were mostly carried out at open-circuit conditions. Overall, configuration shown in Figure 3.4 was used. This configuration guarantees that the open-circuit condition is satisfied at all times since the series connected capacitor does not pass DC current.

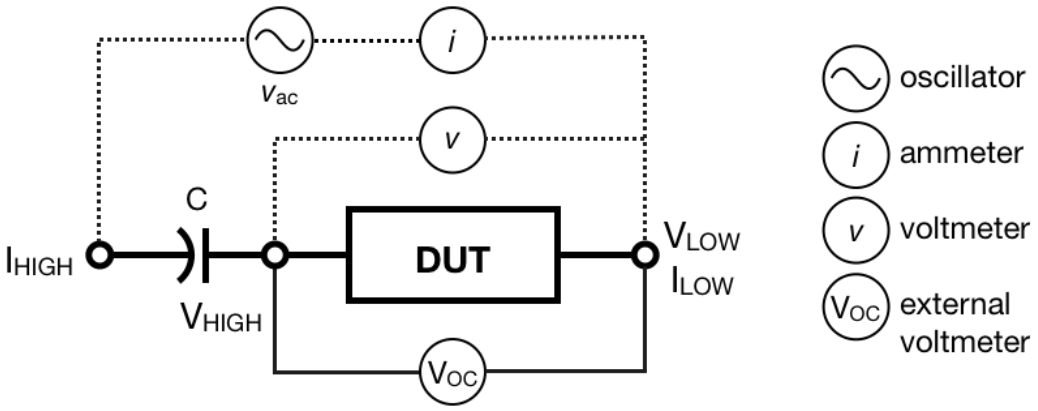

Figure 3.4. *Impedance measurement configuration at open-circuit; DUT: device under test, v_{ac}: oscillation voltage, I, V: terminals.*

In this figure, dashed lines represent the internals of impedance analyzer. It consists of an oscillator for small voltage perturbation v_{ac}, vector ammeter *i* and a vector voltmeter *v*. It employs 4-wire configuration where voltage is sensed between V_{HIGH} and V_{LOW} terminals, and current is measured through I_{HIGH} and I_{LOW} terminals. In order for the generated voltage to be held on the device under test (DUT), a large electrolytic

capacitor C (~10 μF) was connected in series between the I_{HIGH} and V_{HIGH} terminals. Since the voltmeter's impedance is high, the DUT preserves its open-circuit voltage (there is no DC current flowing through DUT). However, because the capacitor C is large, it allows an alternating current on itself. As the frequency drops around several tens of Hertz, there might be a certain voltage drop on C. This does not affect the measured impedance though, since the voltage is remotely sensed on DUT. But, the oscillation level on DUT is diminished resulting in a drop of signal-to-noise ratio. Oscillation voltage was adjusted in order to compensate this effect. Note that the perturbation of voltage on DUT itself was always checked through the analyzer and was not allowed to exceed 10 mVrms.

Benefits of employing the large capacitor C in impedance measurements at open-circuit is twofold: (i) The voltage on the cell was constantly measured by an external voltmeter V_{OC} to see if there was a degradation, (ii) otherwise employing a constant DC voltage to imitate open-circuit conditions might have been problematic due to the low-frequency dynamics of perovskites (open circuit voltage of the cell can drift during the measurement), which is also observed as hysteresis.

The cells were illuminated with a custom-made setup using chip-on-board white LED array of 3 by 3 placed on a cooling fan attached heatsink. LED was placed ~10 cm away from the cone shaped aperture where in between light is diffused by using several frosted tapes. The interior of the aperture was covered with aluminum foil in order to reflect and scatter the light. Uniformity of light intensity was confirmed by measuring the short circuit current of the cells at different lateral points. Sun equivalent photon flux was calibrated using a high-grade c-Si solar cell with a short-pass filter window of 800 nm cutoff attached to it. For this calibration, 1 Sun equivalence was determined by comparing the short-circuit current of the c-Si solar cell obtained in the solar simulator with the one obtained in this setup. Intensity of white light was adjusted by controlling the current passing through it for small increments. For decreasing light intensity substantially, neutral optical density filters were used.

CHAPTER 4

RELIABLE EFFICIENCY MEASUREMENTS OF PEROVSKITE SOLAR CELLS

Reliable assessment of efficiency of a perovskite solar cell (PSC) is quite complicated due to the hysteretic behavior of these cells. It is commonly observed that simple current–voltage (I–V) scan does not yield reproducible results for different scan rates, or directions. Therefore, different types of approaches should be employed in order to determine the efficiency of the devices reliably. This chapter presents methods of efficiency measurement of PSCs with a special emphasis on extraction of the steady-state behavior by resolving the hysteretic response. In addition, a control algorithm has been proposed in order to track the maximum-power-point (MPP) of solar cells.

4.1. Effect of Hysteresis in Efficiency Measurements

Dynamic processes, going on a PSC might occur on the timescales of seconds and minutes, which is dependent on the architecture of the solar cell. Hence, an I–V curve of a PSC generally features hysteresis so that the history of the device affects its state. For instance, reverse scan of the voltage (from forward bias or open-circuit voltage V_{OC}, to reverse bias or short-circuit current J_{SC}) and forward scan yields different results. Furthermore, different scan speeds (i.e. mV/sec) gives different I–V curves. I–V characteristics of an n–i–p cell featuring severe hysteresis is presented in Figure 4.1.

As it is evidenced by Figure 4.1, any I–V curve does not necessarily reflect the real-world efficiency, since all curves belonging to the same device implies different efficiency values. In fact, for a photovoltaic (PV) device, the ultimate performance

criterion is the maximum power output at the steady-state. Although maximum-power-point tracking (MPPT) seem to be the obvious choice, different measurement procedures are proposed in the literature to address this issue [53], [64], [65]. Here some approaches to this issue was presented and a MPPT algorithm was designed and implemented as well.

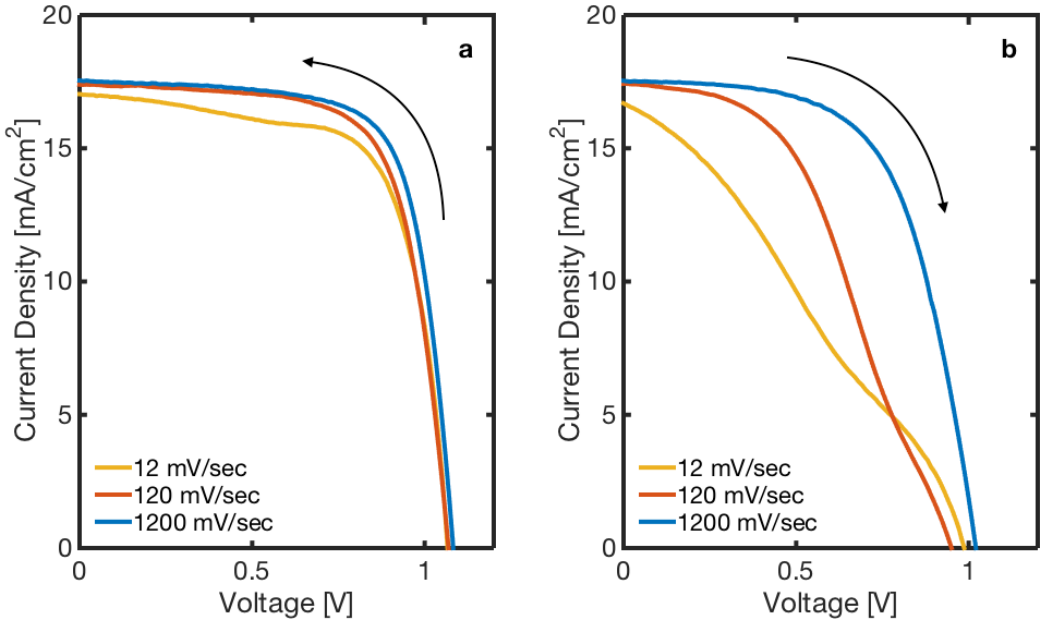

Figure 4.1. *I–V curves demonstrating severe hysteresis in a TiO_2-based n–i–p PSC: a) reverse scan, b) forward scan. Cells are fabricated in this study.*

4.2. Efficiency Measurement Techniques

Different efficiency measurement techniques are evaluated in this section. Special emphasis is made on dynamic I–V and MPPT measurements.

Standard I–V measurement. Current is recorded for each voltage increment where voltage changes are abrupt and has fixed dwell time. It allows acquisition at variable time durations so that dwell time can be modified.

Current measuring at the steady-state. Current passing through the device is monitored and recorded for a fixed voltage, or a voltage generated by the cell is

recorded at the open-circuit. This approach gives the time evolution of J_{SC}, current at the MPP J_{MPP} and V_{OC} while providing insight on the device dynamics—for example, by employing open-circuit voltage decay and rise measurements. In particular, if V_{MPP} can be chosen accurately, steady-state measurement of J_{MPP} yields stabilized PCE.

Dynamic I–V. Alternatively called time-resolved I–V, this method was probably is the most accepted one since a complete I–V curve is obtained. In this scheme, voltage is swept like in the standard I–V measurements but at each voltage increment, current is allowed to be stabilized. Either a certain time interval is applied, or an adaptive monitoring system determines the stabilization of the current. Being a major institute that certifies PCE values of solar cells, National Renewable Energy Laboratory (NREL) of U.S. Department of Energy adopts the use of dynamic I–V while it disregards standard I–V measurements for perovskite devices [53].

A LabVIEW™ program that controls Keithley Series 2400 source-meter (device that can measure and supply current and voltage) in order to obtain dynamic I–V characteristics was constructed. An excerpt taken from a dynamic I–V measurement is presented in Figure 4.2. Voltage was continuously applied as in (b) and the current was measured at the points denoted by circles (a), in contrast to the standard I–V measurements which takes the measurement rather instantly, at the points denoted by crosses. As can be seen in Figure 4.2b, current had not stabilized at these points which causes erroneous results. Dynamic I–V represents steady-state values and it is better and a reliable alternative to the conventional I–V sweep techniques when characterization of slow-response devices is needed.

In Figure 4.3, standard and dynamic I–V characteristics of two p–i–n perovskite devices of different behaviors are depicted: In (a), PSC allows for standard I–V measurements since dynamic I–V agrees with it well enough. However, in (b) dynamic measurement does not match with the standard I–V. Hence, dynamic I–V should take the precedence when determining the efficiency since steady-state value is the only value that has a significance in the real-world applications [65].

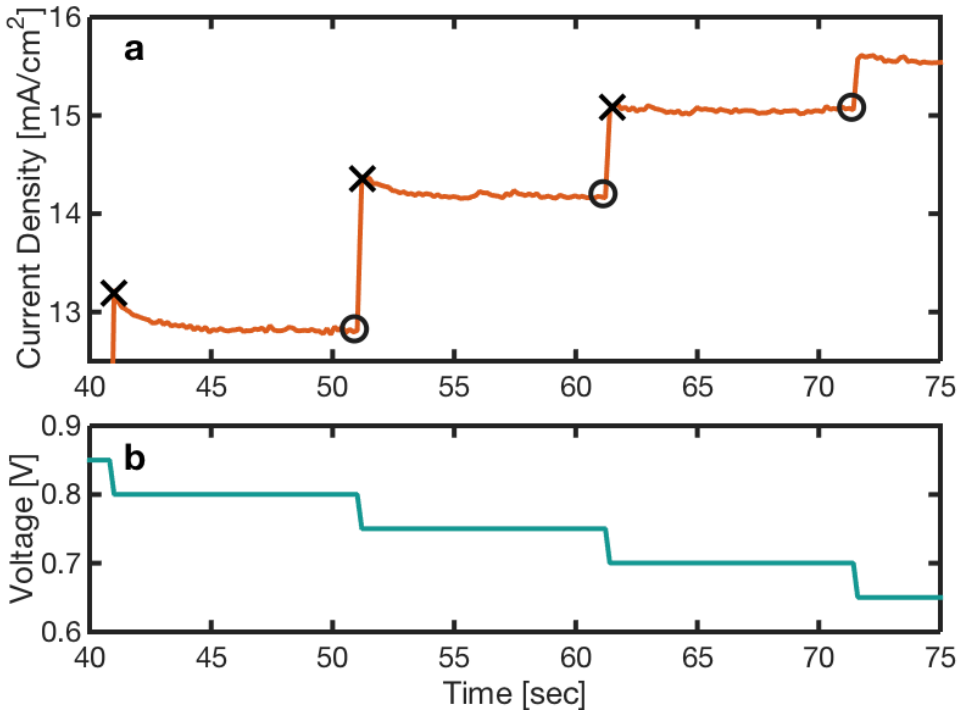

Figure 4.2. *Dynamic I–V measurement in time domain: time evolution of (a) current and (b) fixed voltage increments*

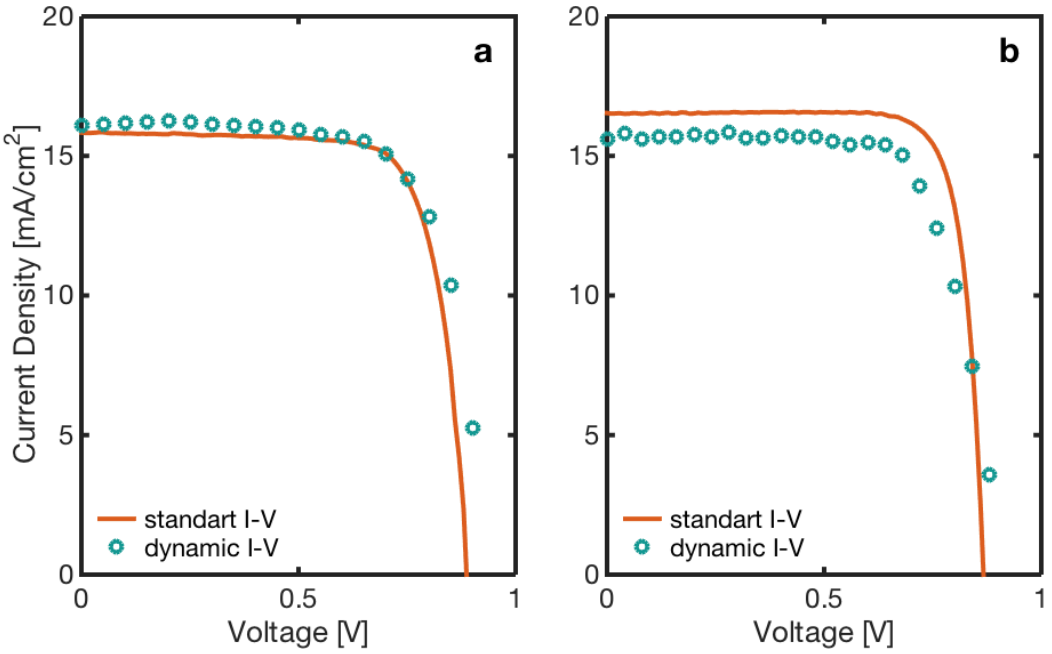

Figure 4.3. *Comparison of dynamic I–V and standard I–V for PSCs: (a) a PSC where dynamic measurements agrees with standard I–V, (b) a PSC where dynamic measurement does not match with the standard I–V*

Maximum-power-point tracking, MPPT. Being the fastest efficiency assessment method, MPPT also imitates the real-world application of PV devices since PV power stations supplying electricity in the grid level uses MPPT algorithms. However, this method alone lacks multitude of different information that can be obtained by using other methods, and it gives only the J_{MPP} and V_{MPP}. Other parameters such as J_{SC}, V_{OC}, and hence fill factor *FF* are left undetermined. Also, the shape of the I–V curve, which might provide insight on the solar cell behavior, such as through the determination of diode ideality factor, is not acquired.

Incremental conductance, perturb & observe, and fuzzy logic algorithms are among the major MPPT methods employed in the literature [66]. Typical power curve of a PV cell or an installation was given earlier in Figure 2.2. By the inspection of this figure, it is evident that increasing voltage will increase the power output when operating point is on the left of the MPP and decrease it if operation point lies in the right. This observation also equivalent to the following expression relating the slope of the power–voltage curve:

$$\begin{cases} dP/dV = 0, & V = V_{\mathrm{MPP}} \\ dP/dV > 0, & V < V_{\mathrm{MPP}} \\ dP/dV < 0, & V > V_{\mathrm{MPP}} \end{cases}$$

In perturb & observe algorithm a small perturbation ΔV is imposed on the voltage and the power output is observed. If the resulting change in power *dP/dV* is positive, then the perturbation sustained and $V_{k+1} = V_k + \Delta V$ is used as the next bias voltage. In contrast, if *dP/dV* is negative, perturbation is reversed so that $V_{k+1} = V_k - \Delta V$. This system causes oscillations of $\pm\Delta V$ around the MPP in the steady-state. Reduction in ΔV solves this problem but slows down the system. A dynamic approach can be applied so that the perturbation voltage is decreased as the MPP is reached [66].

4.3. Design of a Maximum-Power-Point Tracker

Here, a more comprehensive and effective method was implemented: feedback control for the parameter *dP/dV*. Since *dP/dV* = 0 at the MPP, a PID controller can be used to drive the error to zero and, hence, to reach the MPP. A generic block diagram for PID feedback control is given in Figure 4.4.

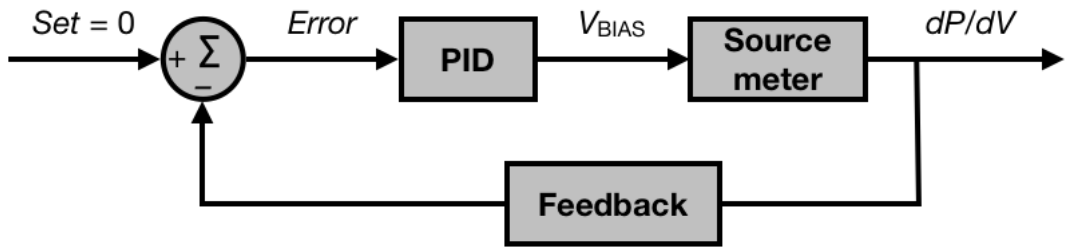

Figure 4.4. *PID control schematic for MPPT*

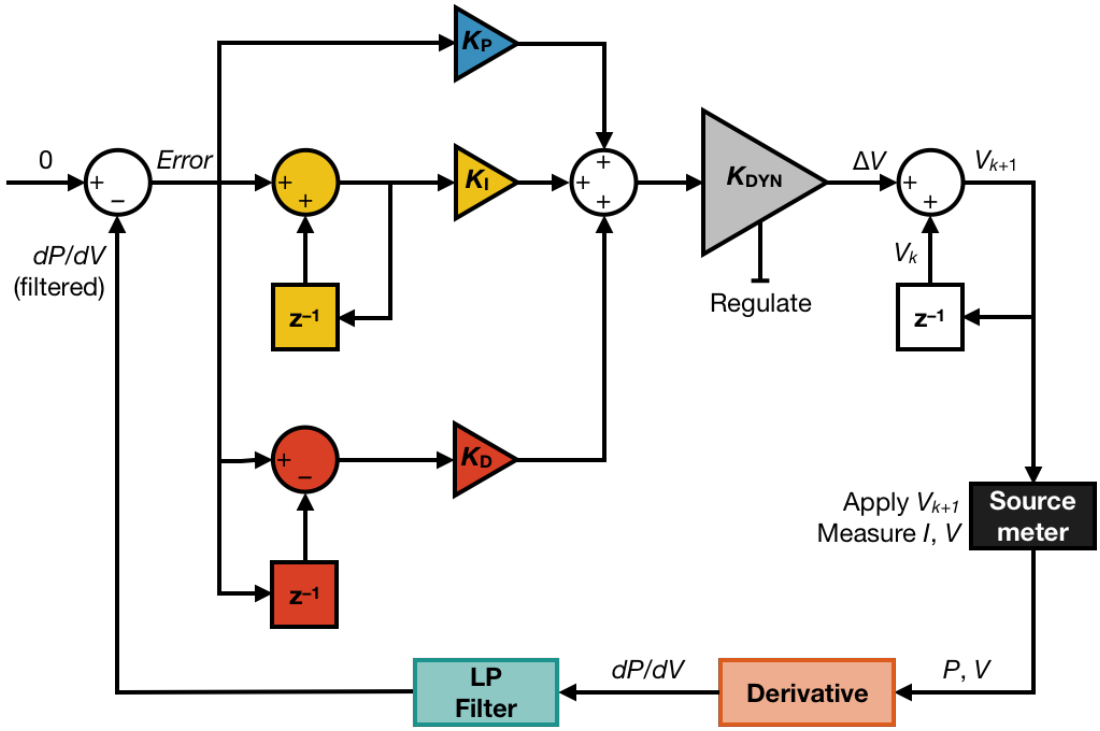

Figure 4.5. *MPPT block diagram*

Implementation of such a control scheme is slightly more involved. Explanation of the designed MPPT system will be given by the help of Figure 4.5. In this figure,

parameters and components for proportional, integral, and derivative (hence the name PID) parts is given with the colors blue, yellow, and red, respectively. Circles denote summation, squares (see z-transform, z^{-1}) denote delay of single iteration, and triangles denote proportional gain operations.

The term $Error = -dP/dV$ is accumulated by the summer (i.e. integrator), consecutively subtracted from the previous value by the difference operation (i.e. differentiator) and scaled accordingly by the gain terms K_P, K_I and K_D—subscripts denoting P: proportional, I: integral, and D: derivative. Then, all 3 components are summed. Since the dynamics of the system should be invariant of the order of magnitude of the current, and hence of the power, a regulating dynamic gain parameter K_{DYN} was introduced. This parameter is inversely proportional to the area of the device, light intensity, and expected efficiency of the device since the power output is proportional to these variables. Also, since the slope dP/dV in the left-hand side of the MPP is typically smaller than the right-hand side, another gain correction is included in K_{DYN} depending on the sign of dP/dV. After aforementioned corrections are made on the PID controller output by K_{DYN}, resulting value, denoted as ΔV, is added to the current voltage bias value of V_k. A new voltage value is obtained as $V_{k+1} = V_k + \Delta V$ and it is applied in the next iteration by the source-meter. After applying new bias V_{k+1}, a special pseudo-derivative (orange rectangle in Figure 4.5) operation was performed to yield dP/dV term. Digital low-pass filtering was applied in order to suppress noisy components associated with the differentiation in discrete-time. Resulting filtered dP/dV term is subtracted from the set value of 0 to complete the feedback cycle.

The derivation operation yielding dP/dV term needs special treatment. Here, a pseudo-differentiation subroutine employing another feedback loop was used since standard 2-point discrete differentiation gives noisy results and causes unstable operation.

In a typical 2-point discrete derivative, a differentiation operation can be written as:

$$\frac{dP}{dV} \cong \frac{P_k - P_{k-1}}{V_k - V_{k-1}} \equiv \frac{\Delta P}{\Delta V} \tag{4.1}$$

Here subscripts k and k–1 denotes current and previous values of the variable, respectively. Note that as the MPP is reached, the term ΔV goes to zero. Since it is in the denominator, division by 0 (or a value close to 0) produces an unbounded, very high dP/dV. This results in a very high adjustments in next value of ΔV—thus, causes instability. In the pseudo-derivative approach, following intuition was used: dP/dV value should approximate the real slope of the power curve in transient, but not necessarily in the steady-state. So, a damping factor along with recursive computation can be used so that dP/dV can be approximated by using previous values of dP/dV itself, as follows:

$$\left(\frac{dP}{dV}\right)_k = C\left(\frac{dP}{dV}\right)_{k-1} + \frac{\alpha(P_k - P_{k-1})}{1 + \alpha(V_k - V_{k-1})}, \qquad \text{where } C \in (0,1), \alpha > 0 \qquad (4.2)$$

From Equation 4.2, it is seen that initially, $(dP/dV)_k \approx \Delta P/\Delta V$ if α is large and C is small enough where $\Delta P \equiv P_{k+1} - P_k$, and $\Delta V \equiv V_{k+1} - V_k$. As the MPP is reached, with ΔP and ΔV going to zero, $(dP/dV)_k \approx (dP/dV)_{k-1}$ if C goes to 1. It means that now, the value $(dP/dV)_{k+1}$ is bounded by its previous value $(dP/dV)_k$, while it approximates real slope of the power–voltage curve in transient. At this point, if C is defined as the denominator in the right-hand side, $C \equiv 1 / (1 + \alpha\Delta V)$, the specified conditions on C is satisfied by picking a large α. Such modification yields:

$$\left(\frac{dP}{dV}\right)_k = \frac{1}{1 + \alpha(\Delta V)}\left(\left(\frac{dP}{dV}\right)_{k-1} + \alpha(\Delta P)\right), \qquad \alpha > 0 \qquad (4.3)$$

In fact, Equation 4.3 corresponds to the replacement of derivation in s-domain of Laplace transform so that s is replaced by $\alpha s / (s+\alpha)$. Note that as α goes to infinity, these expressions are directly equal to the standard 2-point discrete derivative in Equation 4.1. The expression in Equation 4.3 still needs some refinement since at the right-hand side of MPP, V_{k+1} might be smaller than V_k. It might result in $(1 + \alpha\Delta V) \approx 0$, which drives $(dP/dV)_k$ to infinity. Hence, the absolute value of ΔV should be taken and $\alpha\Delta P$ should be corrected for the sign of ΔV. Final adjustments result in the following expression:

$$\left(\frac{dP}{dV}\right)_k = \frac{1}{1 + \alpha|\Delta V|}\left(\left(\frac{dP}{dV}\right)_{k-1} + \alpha(\Delta P)\mathrm{sgn}(\Delta V)\right), \qquad \alpha > 0 \tag{4.4}$$

In Equation 4.4, sgn(.) is the signum function that returns the sign of the argument as:

$$\mathrm{sgn}\,(x) \equiv \begin{cases} -1, & x < 0 \\ 0, & x = 0 \\ +1, & x > 0 \end{cases}$$

By this way, Equation 4.4 defines the operation of MPPT for both sides of the MPP, symmetrically.

The resulting MPPT algorithm was implemented by using LabVIEW™. Tuning of PID was carried out by using Good Gain method [67] with a modification of derivative term borrowed from Ziegler-Nichols' Ultimate Gain method [68]. These methods provide a rather heuristic approach for tuning PID controllers for cases that the underlying transfer function of a real system is not known or vaguely defined. In fact, this is the case for the I–V measurements of PSCs since they might exhibit severe hysteresis. Modelling such behavior (see Figure 4.1) is daunting and redundant for this very case of MPPT system. Therefore, for the sake of simplicity and practicality, Good Gain method was employed (details regarding this procedure can be found elsewhere: [69]). By this way, a versatile MPPT algorithm that is operating efficiently, whether the cell exhibit hysteresis or not, was realized.

Overall, an MPPT system was designed and implemented by a custom-made LabVIEW™ program. This program communicates with a Keithley Series 2400 source-meter through a computer and controls it to find and hold the MPP of the device connected to it. Efficiency values reported in this thesis, if they were extracted from the I–V curves, were always cross-checked with MPPT results. An example of MPPT result is given in Figure 4.6. Note that, the *I*, *V* vs. time plot drawn in semi-logarithmic scale for the clear inspection of voltage settling. Voltage is settled in ~6 seconds. The

~10% efficiency of this PEDOT:PSS based p–i–n device did not degrade in 30 minutes. Device were monitored for another 30 minutes with no change in efficiency.

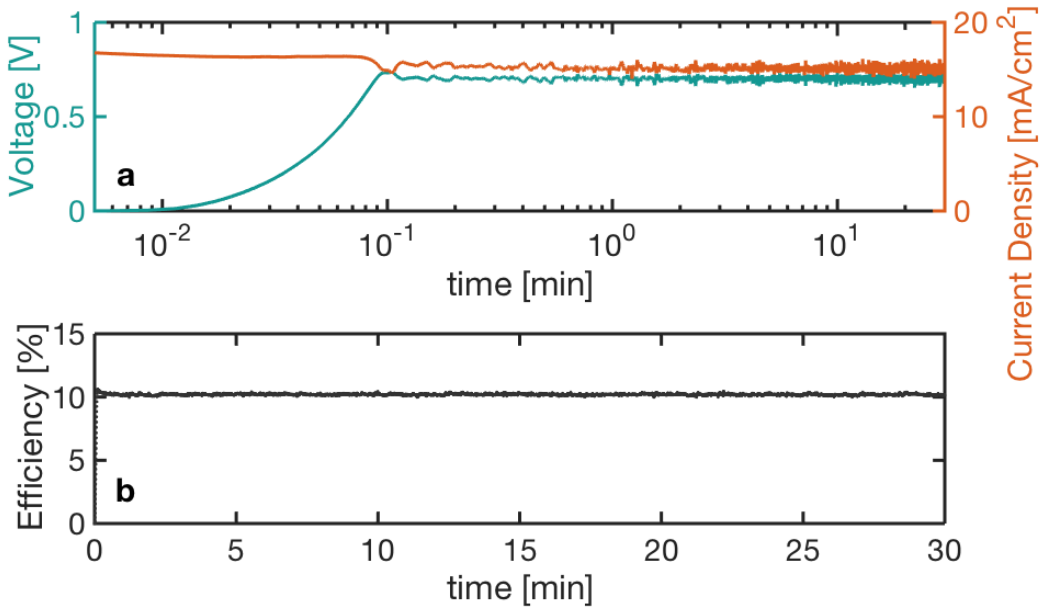

Figure 4.6. *Evolution of cell voltage and current in logarithmic time scale (a), and efficiency in linear time scale (b) for an MPPT measurement*

4.4. Final Remarks

In emerging PV technologies, the driving force of research is often the race for efficiency enhancement. This tendency necessitates the reliable assessment of device performances in order for the dissemination of true and relevant knowledge. For PSCs, which demonstrates anomalous behavior during I–V characterizations, special care should be taken. Because a solar cell is made to operate in steady-state conditions, the real figures of merit are the steady-state parameters. Therefore, when a discrepancy between two different measurement methods are observed, the one utilizing the stabilized values should take the priority. In this chapter, it has been shown that the dynamic I–V measurements are more reliable than standart I–V scans. In addition, if a fast acquisition of efficiency is needed, MPPT systems should be employed. MPPT of solar cells under working conditions also provides the time evolution of efficiency, which is of utmost importance when they are utilized in PV power stations.

CHAPTER 5

IMPEDANCE RESPONSE AND MODELLING

High and low frequency impedance models of perovskite solar cells (PSC) have been proposed by analyzing the impedance response of the cells in different steady-state conditions. The proposed models were verified by showing that they describe the impedance response in open-circuit well enough with respect to the changes in incident light intensity.

5.1. Impedance Spectroscopy

Impedance spectroscopy (i.e. IS) is the measurement of the electrical impedance of a system as a function of frequency, in simple terms. In IS, impedance response $Z(f)$ of the system is measured at a range of frequency f while preserving linearity. The main strength of IS technique is the ease in deconvolution of different processes occurring in different time orders, hence frequencies. In order to extract the physical meaning of different processes, a variety of steady-state conditions are imposed on the system prior to and during impedance measurements. By analyzing the resultant impedance data in conjunction with the steady-state conditions, a model representing the system might be constructed. This model can be pretty valuable since it might serve as a guide on how to optimize the system of concern.

In fact, the emerging PSC field still lacks a thorough understanding of device physics. Hence, IS techniques can be applied to reveal and elucidate the underlying physical processes. It should be noted that dye-sensitized solar cell (DSSC) research benefited greatly from IS techniques over the course of its evolution. The literature is simply

vast (see [70] as a detailed analysis) and will not be reviewed here. Actually, there are many applications of IS on PSCs in the literature as well: [71]–[73]. Yet, there are still numerous issues that need to be clarified. In addition, perovskites are notorious owing to the dependence of their properties to nuances in fabrication techniques. And, their fabrication techniques are plentiful along with their architectures as it were explained in Chapter 3. One-step solution processing is the most employed method. Impedance modelling of PSCs involving vacuum deposition in the fabrication is rather unexplored. Therefore, IS techniques were applied in order to study the PSCs employing vacuum deposited PbI_2 layers, which have been fabricated in the scope of this thesis.

5.2. Recombination in Impedance Response

One of the strengths of IS is that it allows the analysis of recombination in devices. IS analyses might provide the recombination mechanisms present, give quantitative idea on *how much* recombination occurs in device, and contribute to the comparison of modifications on the device structure in regard to their effect on recombination. IS methods are, in general, quite advanced and intensive but can be very rewarding in certain cases—if proper care is taken during evaluation of the data.

Impedance measurements can be used to resolve the underlying recombination processes through the analysis of impedance spectra since these processes, governing the operation of devices, have impedance responses associated to them. Physical origins of such responses are well established in the literature. The central parameter of impedance modelling of recombination is the recombination resistance R_{rec}. It is defined as the inverse rate of change of recombination rate $U_{n,p}$ with respect to the associated charge carriers' (electrons or holes) Fermi level $E_{Fn,p}$. Here, $U_{n,p}$ is the stationary component of the recombination rate, and by definition, is not affected by imposed ac voltage. For a p-type semiconductor where electrons are minority carriers, R_{rec} can be defined as [58]:

$$R_{\mathrm{rec}} \equiv K\left(\frac{\partial U_{\mathrm{n}}}{\partial E_{\mathrm{Fn}}}\right)^{-1} \tag{5.1}$$

where K is a proportionality factor that depends on the volume of the semiconductor. (In fact, this definition is what allows the impedance model of solar cells to be the parallel combination of R_{rec} and chemical capacitance C_{μ} as it will be presented later.) As the Fermi level E_{Fn} is modified by the externally applied small ac voltage, the measured R_{rec} can be thought as a differential *resistance* representing the change of E_{Fn} (related to voltage) to the change of U_{n} (related to current by the number of electrons responding to the field). In order for the terms E_{Fn} and U_{n} to be approximated by the stationary components, the voltage perturbation v_{ac} should be small to preserve linearity. By this intuition, Equation 5.1 makes sense as well. In the simplest terms, R_{rec} is inversely proportional to the number of carriers that undergo recombination, hence the *amount* of recombination.

Another representation which is equivalent to Equation 5.1 is given as follows [58], [74], [75]:

$$R_{\mathrm{rec}} = \left(\frac{\partial J_{\mathrm{rec}}}{\partial V}\right)^{-1} \tag{5.2}$$

where J_{rec} is the recombination current per unit area, and R_{rec} is the resistance times the unit area. Note that $J_{\mathrm{rec}} = qWU$ where q is the elementary charge, W is the thickness of the semiconductor and U is the recombination rate given generically. At open-circuit conditions, where all generated carriers are to recombine, the rate of generation G equals to the rate of recombination U, i.e. $G = U$. Since G is proportional to the photon flux Φ so is U, and hence J_{rec}. Therefore, it is trivial that R_{rec} is inversely related to Φ incident on semiconductor. Overall, any inverse relation observed in light dependence of an IS resistance can be considered as a telltale sign of connection of that resistance to recombination. Furthermore, assuming a power law dependence of U to free carrier density n (i.e. $U = k_{\mathrm{rec}} n^{\gamma}$ where γ is the order of reaction), R_{rec} contains information on recombination coefficient, k_{rec}. In fact, $R_{\mathrm{rec}} \propto k_{\mathrm{rec}}^{-1}$.

One of the most important processes in a solar cell is the recombination of carriers and it can be readily observable by IS through R_{rec}. Therefore, discussion regarding the recombination and its effect on impedance spectra will be integral to the developed impedance model.

5.3. High Frequency Modelling

Establishment of impedance model of a solar cell can be made by using equivalent circuits. They provide with visualization of ongoing processes in a cell, facilitation of analysis of each process, and enforcing causality dictated by Kramers–Kronig relations [76]. The simplest impedance model of a solar cell with perfectly selective contacts can be given by a parallel connection of a capacitor and a resistor corresponding to chemical capacitance C_μ and recombination resistance R_{rec} (derivation can be found in [58]). Ideal case of equivalent circuit is given in Figure 5.2. It is important to note that this equivalent circuit of $C_\mu \parallel R_{rec}$ does not correspond to components of a physical parallel plate capacitor and a power dissipating resistor. It is merely a model that explains the ac response of an ideal solar cell. This notion should be kept in mind always when treating equivalent circuits of IS models, although some components can have a direct correspondence to electrical origin.

Some peculiar features of PSCs, such as hysteresis associated with the dependence of I–V curves on cell's history and voltage scan rate, are occurring on the order of milliseconds to seconds. This is plausible since I–V curves are obtained on the similar order of time. Such low-frequency features surely affect the IS spectra at low frequencies. Therefore, high-frequency response is the right choice as the starting point of modelling PSCs. A typical Nyquist plot of PEDOT:PSS based p–i–n PSC is given in Figure 5.1. In this case, frequency was swept from 1MHz to 100 Hz and impedance response was recorded in the dark. As it is evident from Figure 5.1, there are two distinct features: (i) high-frequency (HF) semi-circle and (ii) a low-frequency (LF) component. HF feature will be analyzed first.

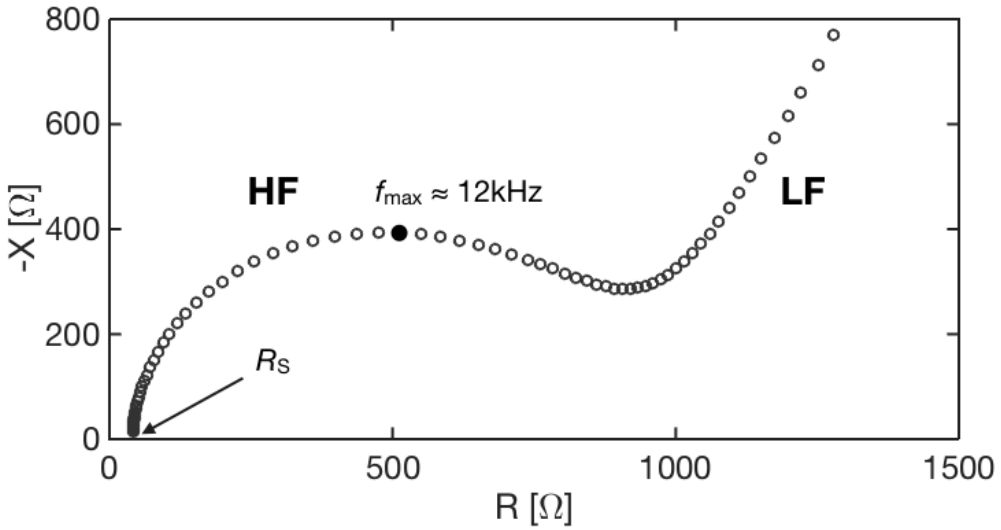

Figure 5.1. *Nyquist plot of a PSC featuring high and low frequency characteristics*

In an ideal solar cell whose impedance model is $C_\mu \parallel R_{rec}$, time constant associated with f_{max} observed at HF is equal to the carrier lifetime [58]. Typically, carrier lifetimes in perovskite materials are on the order of 100 ns to 1µs (see Table 1.1). These values correspond to f_{max} of order 1–10 MHz. Mismatch between f_{max} values calls for several arguments: (i) this HF process of $f_{max} \approx 12$ kHz is not associated directly with recombination, (ii) recombination resistance R_{rec} sees another capacitance C_x that is considerably larger than C_μ i.e. $C_x \gg C_\mu$ (so that $f_{max} = 2\pi(R_{rec}C_x)^{-1} \ll$ 1–10 MHz) or (iii) both. When a simple RC circuit was fit into the HF part of the impedance response, a $C_x \approx 130$ nF/cm^2 was found. Typical value for the relative permittivity of perovskite $\varepsilon_{PVK} \approx 20$ [77], [78] and the thickness is $d \approx 300$ nm, as in cross-sectional micrograph in Figure 3.3. For these values, the geometrical capacitance C_{geo} (which is unavoidable and associated with the top and bottom contacts of the device) of the cell is around ~60 nF/cm^2 which is comparable to 130 nF/cm^2. (Here, note that $C_{geo} = \varepsilon_{PVK}\varepsilon_0 / d$ where ε_0 is vacuum permittivity.) This twofold increase can be ascribed to the roughness of electrodes. Also it has been shown that, for planar PSC configurations lacking a m-TiO_2 layer, $C_{geo} \gg C_\mu$, even in high bias voltages of V_{OC} [79], [80]. Therefore, it might be assumed that C_x corresponds to C_{geo}. This is verified in the upcoming analyzes.

Another observation regarding Figure 5.1 is that Nyquist plot does not cross the origin. In fact, the point where it intersects with x-axis of R corresponds to the series resistance R_s of the device that is present in all solar cells. As the frequency tends to infinity, all capacitive components are shorted, and this results in $Z \rightarrow R_s$. In PSCs, R_s mostly corresponds to the resistance associated with the bottom contact of TCO. Also, shunt resistance R_{sh} is mostly unavoidable in polycrystalline materials like perovskite films. Abundance of grain boundaries might provide additional low resistance pathways for electrons causing leakage. By using aforementioned observations, a modified HF model of PSC (as it deviates from the ideal case) can be proposed as in Figure 5.2.

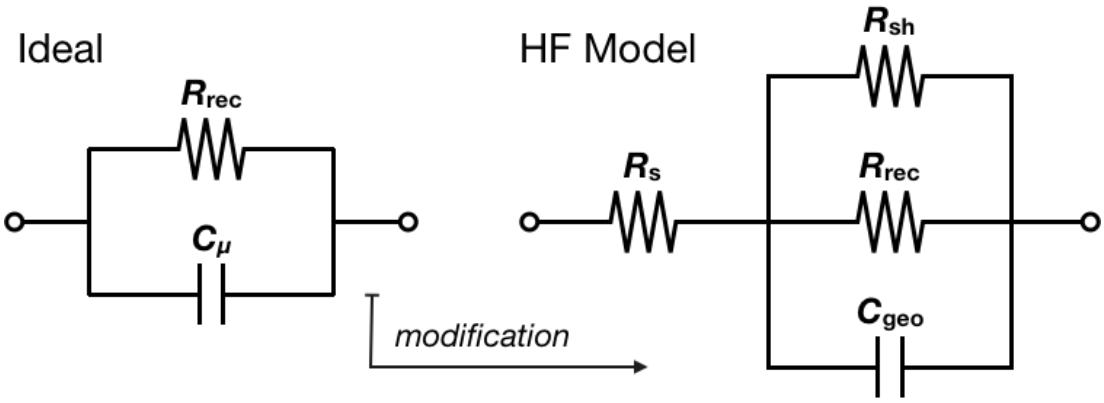

Figure 5.2. *Ideal and modified high frequency models for PSCs*

Impedance modelling from a given set of impedance data is an inverse problem of ill-posed nature. In this context, it means that for an output impedance data, there are models that can reproduce the data and they are not unique. Hence, different steady-state conditions should be imposed in order to verify the proposed model. At this point, suitable experimental sets regarding these different steady-state conditions should be designed so that the validity of the proposed HF model of PSC is checked. In the IS setup that was built, different bias voltages V_{DC} as well as different irradiance levels can be imposed on the devices. In this thesis, an equivalent representation of photon flux was adopted: Photon flux Φ is represented by its equivalent intensity of AM1.5 irradiance and was sometimes given in terms of optical density OD. OD value corresponds to the negative logarithm of the transmittance. For instance, for a Φ value

of 0.3 OD, the photon flux is equal to the $10^{-0.3}$ (~1/2) times the number of total photons in AM1.5 irradiance spectra that can be absorbed by the perovskite.

First attempt to carry out is to verify (or at least strengthen) the assumptions made: (i) x-axis crossing of Nyquist plots correspond to the electrical series resistance R_s, (ii) HF semi-circle is associated with the geometrical capacitance of the device C_{geo} by assuming $C_{geo} \gg C_{\mu}$, (iii) R_{sh} is of order that cannot be omitted for the sake of simplicity. All these components are assumed to be of electrical origin and should not be affected by either V_{DC} or photon flux Φ. Hence, a trivial approach would be to change V_{DC} and Φ, and see if these parameters remain unaffected in impedance data. Note that the case is a bit complicated for R_{sh} as it is discussed subsequently in Section 6.2. However, R_{sh} was assumed to be independent of Φ in this chapter since this assumption does not invalidate the proposed impedance models, at least in low to high illumination conditions at open-circuit.

In Figure 5.3, three cases are demonstrated for a PEDOT:PSS based p–i–n device as Nyquist plots: In (a) V_{DC} is changed while devices were measured in the dark. When fitting on the HF portion of the spectra carried out, C_{geo} turned out to be 113 nF/cm^2 for all three cases. And associated resistance changed very little, as readily observed from the plot itself. In (b) V_{DC} is changed while devices were measured under an illumination of Φ = 0.5 OD. After fitting, C_{geo} values of 89, 86, and 86 nF/cm^2 were obtained for 0.4 V, 0.6 V, and 0.8 V, respectively. Change in associated resistance is observed by inspection as the semi-circles gets smaller with increase in V_{DC}. In (c), devices were measured in the open-circuit condition while Φ was changed. As the light intensity increases (OD gets smaller), C_{geo}-associated resistance decreases accordingly. Yet, C_{geo} value stays approximately the same with 107, 98, and 97 nF/cm^2 with respect to the increasing Φ. Typically, the dispersion parameter p for constant phase element (CPE) fitting is ~0.95 in these cases.

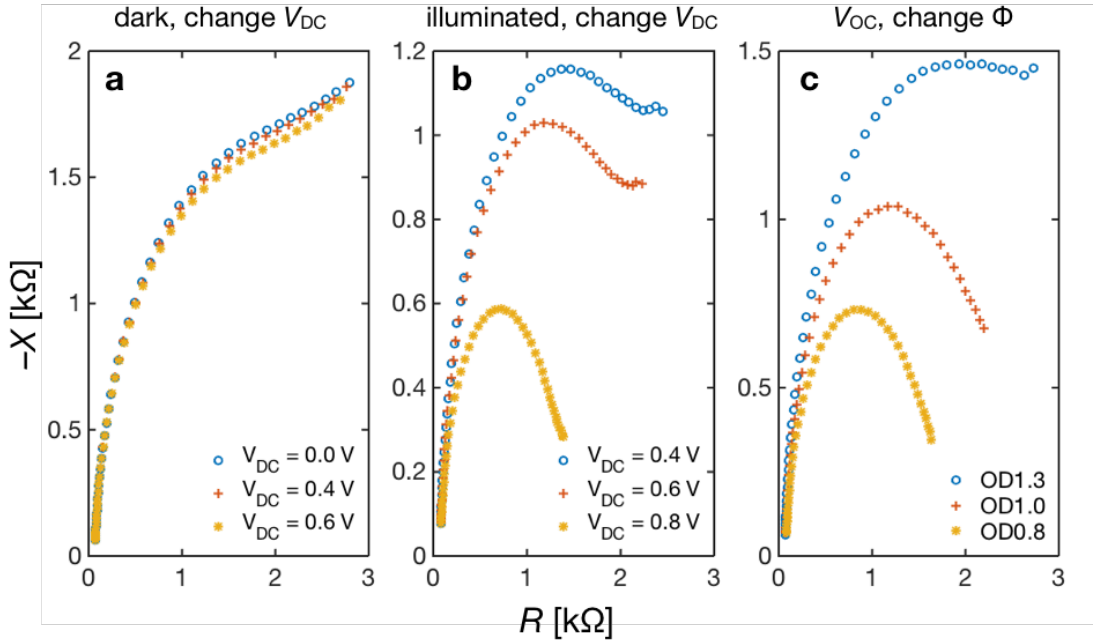

Figure 5.3. *Set of impedance spectra of a PSC in different steady-state conditions: (a) V_{DC} is changed in dark, (b) V_{DC} is changed under illumination, (c) irradiance level is changed in open-circuit*

These findings were interpreted as follows. In all instances in Figure 5.3, Nyquist plot tends to cross the x-axis at the same point of ~60 Ω. Thus, R_s is in fact the series resistance of electrical origin. Furthermore, it is known that C_μ shows exponential dependence on bias V_{DC} [58]. Yet C_{geo} does not change with V_{DC} or Φ. Such independence of C_{geo} to both voltage and irradiance level validates that the capacitance associated with HF semi-circle is simply geometrical and it is much greater than C_μ. The similarity of it to the theoretical value of ~60 nF/cm^2 further confirms that C_{geo} is of electrical origin and is formed by the top and bottom contacts sandwiching the perovskite absorber.

The case for a Φ-independent R_{sh} can be understood with some intuition. In all three cases, the resistance associated with C_{geo} is the parallel combination of R_{sh} and R_{rec} i.e. $R_{sh} \parallel R_{rec}$. If recombination increases, R_{rec} decreases by default. In Figure 5.3a, HF resistance was unaffected by changing voltage although recombination increases with increasing V_{DC}, and is maximized at V_{OC}. This observation implies that $R_{sh} \ll R_{rec}$ and shunt resistance dominates the HF response. It should be noted that R_{sh} can be treated

as a constant resistance due to electrical pathways caused by pin-holes and grain boundaries in the device. When light was shined on the cell, R_{rec} decreases and at least becomes comparable to R_{sh}, which, in turn, decreases $R_{sh} \parallel R_{rec}$ as well. Now, the inverse relation between V_{DC} and R_{rec} can be observed as in Figure 5.3b. Same observation can also be made on Figure 5.3c, since R_{rec} and Φ are also inversely related. Inverse relation between R_{rec} and Φ is due to the increase of recombination with the light-generated carrier density.

This analysis confirms that the proposed HF model given in Figure 5.2 is valid indeed. The analysis of the dependence of R_{rec} on the illumination will be carried out eventually, with considering the effect of R_{sh}. As an important remark, R_{sh} might conceal the direct evaluation of R_{rec} as it is shown in the preceding discussion.

Having established a physical meaning of R_{rec} in Section 5.2, the evaluation of it for changing steady-state conditions will be done. The number of carriers in a device should be changed by some means, so that the response of R_{rec} is studied. One trivial way to do this is to change the illumination Φ upon the solar cell. The following analysis was made on the impedance response of NiO_x-based device ITO / NiO_x / Perovskite / C_{60} / BCP / Ag. Details of fabrication can be found in Chapter 3.

As a first attempt to study HF behavior of PSCs, a HF resistance R_{HF} is defined as the parallel combination of R_{sh} and R_{rec} by lumping them together to a single parameter: $R_{HF} \equiv R_{sh} \parallel R_{rec} = (R_{sh}R_{rec}) / (R_{sh} + R_{rec})$. By this way, the HF model is defined as in Figure 5.4a. IS measurements were carried out in the frequency range 10 Hz–1 MHz at the open-circuit condition. Fitting of HF response was typically made using the impedance data in the frequency range of 30 kHz–10 MHz. Nyquist plots for a selected set of irradiance level are given in Figure 5.4b where dashed lines represent semi-circles of fitting.

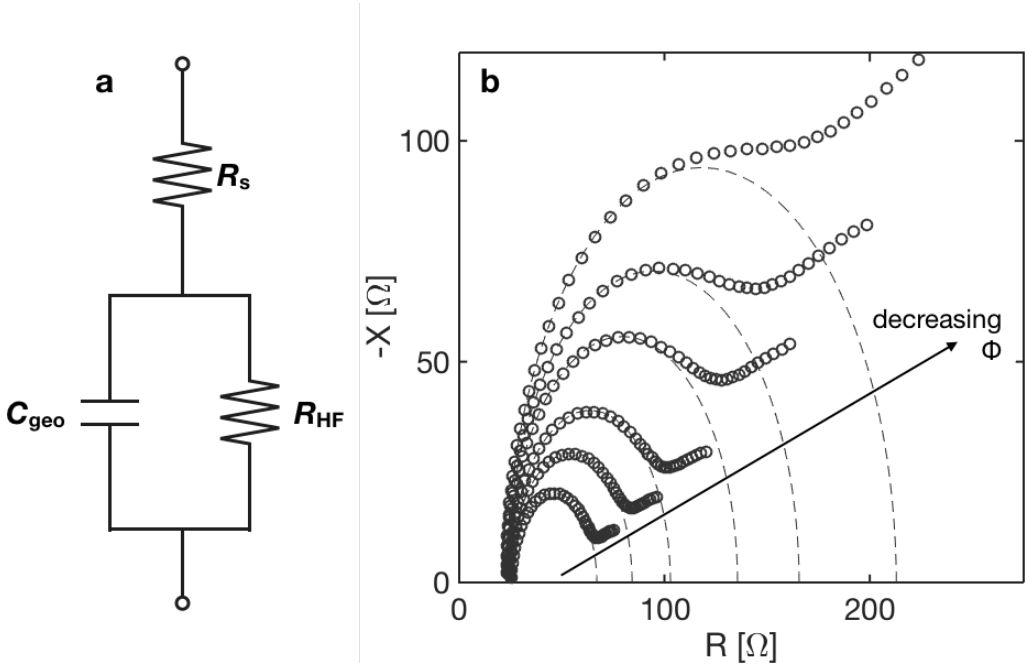

Figure 5.4. *The equivalent HF model (a) and the Nyquist plots (b) for a p–i–n PSC*

Fitting parameters measured at different light intensity conditions were presented in Table 5.1. Values were normalized to a device having 1 cm^2 active area. The listed C_{geo} values are the equivalent capacitance values calculated by Equation 2.5. Dispersion parameters *p* are indicative of well-structured capacitance of geometrical origin as they are very close to 1.

Table 5.1. *Parameters calculated by fitting to the HF equivalent circuit*

Φ [OD]	R_s [Ω]	C_{geo} [nF]	*p*	R_{HF} [Ω]
dark	23.2	92	0.993	77.0
2.5	23.3	136	0.969	35.9
2.1	23.2	137	0.983	34.0
1.7	22.9	139	0.984	31.8
1.4	22.9	142	0.980	27.1
1.2	22.0	144	0.980	23.7
1.0	21.9	146	0.979	19.6
0.9	22.2	143	0.994	17.2

Φ [OD]	R_s [Ω]	C_{geo} [nF]	*p*	R_{HF} [Ω]
0.8	22.3	144	0.995	15.4
0.7	22.3	145	0.996	13.6
0.6	23.0	149	0.994	11.0
0.5	22.9	150	0.995	9.6
0.4	23.0	151	0.996	8.4
0.3	23.1	153	0.994	7.3
0.2	23.2	157	0.992	6.2
0.1	23.3	160	0.988	5.3

Inspection of Table 5.1 reveals that R_s and equivalent C_{geo} parameters mostly remain unaffected by Φ, confirming their electrical origin. R_{HF} decreases with Φ as it is expected. At this point, R_{HF} vs. Φ plot should be given so that the behavior of R_{HF} with respect to Φ is depicted. R_{HF} is previously defined so that $R_{HF} = R_{sh} \parallel R_{rec}$ where R_{rec} is inversely proportional to Φ. Figure 5.5 depicts the illumination dependence of R_{HF} where lines represent the result of fitting. Inset shows the equation of fitting where A is a dummy proportionality constant. In addition, calculated R_{rec} is also shown as it is corrected with the fit value of $R_{sh} = 35.8\ \Omega.cm^2$. R_{sh} can also be found from the y-axis crossing of R_{HF}. Although such value for shunt resistance seems unacceptable for a decently working solar cell, it is speculated that R_{sh} might depend on both voltage and frequency so that the effect of it on I–V curves is not directly associated with this HF value. Such voltage and frequency dependence were discussed in Section 6.2.

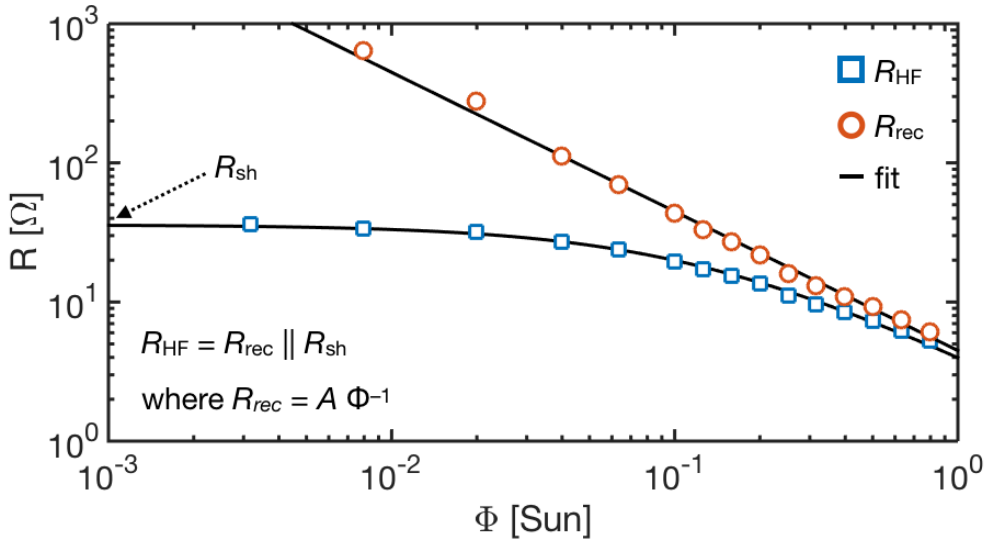

Figure 5.5. *Illumination dependence of R_{HF} and R_{rec}*

Inspection of Figure 5.5 reveals that R_{rec} is in fact the recombination resistance that is inversely proportional to photon flux Φ. The resistance associated with the HF response is simply the parallel combination of R_{rec} and a constant shunt resistance R_{sh}. Note that R_{sh} can easily be confused with R_{rec}, especially in low-illumination conditions in leaky devices, resulting in wrong interpretation of the data.

Overall, the HF impedance model well represents the impedance spectra of NiO_x-based p–i–n devices. This model also successfully applied to the devices employing PEDOT:PSS layer as hole transport material as it is seen in Figure 5.10.

Although analysis of HF response of a solar cell is valuable, mostly in material science perspective, the overall model will be incomplete without the interpretation of LF portion of the impedance spectra. Since the solar cells operate in steady-state (i.e. DC conditions), the total contribution of both high and low frequency response is what determines the overall performance of solar cells. Therefore, analysis of LF response follows.

5.4. Low Frequency Modelling

The Nyquist plot of impedance spectrum obtained for the same NiO_x-based device analyzed in previous section, is given in Figure 5.6. Impedance measurements were carried out from 10 Hz to 1 MHz under 0.1 Sun equivalent illumination at open-circuit. At first glance, appearance of a second semi-circle was observed at low frequency. This hints at a different process coupled to a large capacitive response.

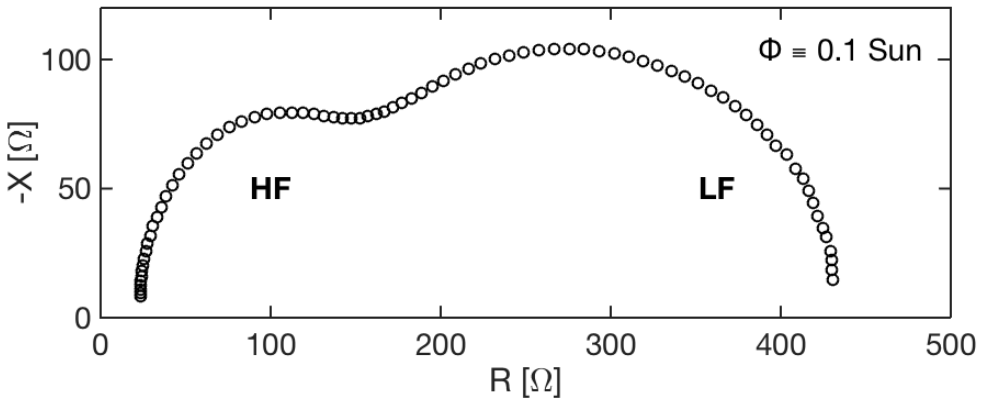

Figure 5.6. *Nyquist plot of a PSC measured from 100 Hz to 1 MHz*

There are various possible equivalent circuits that can represent systems possessing two distinct processes of distinguishable time constants, like the case in Figure 5.6. In order to represent in a simple way, most uncomplicated ones are shown in Figure 5.7.

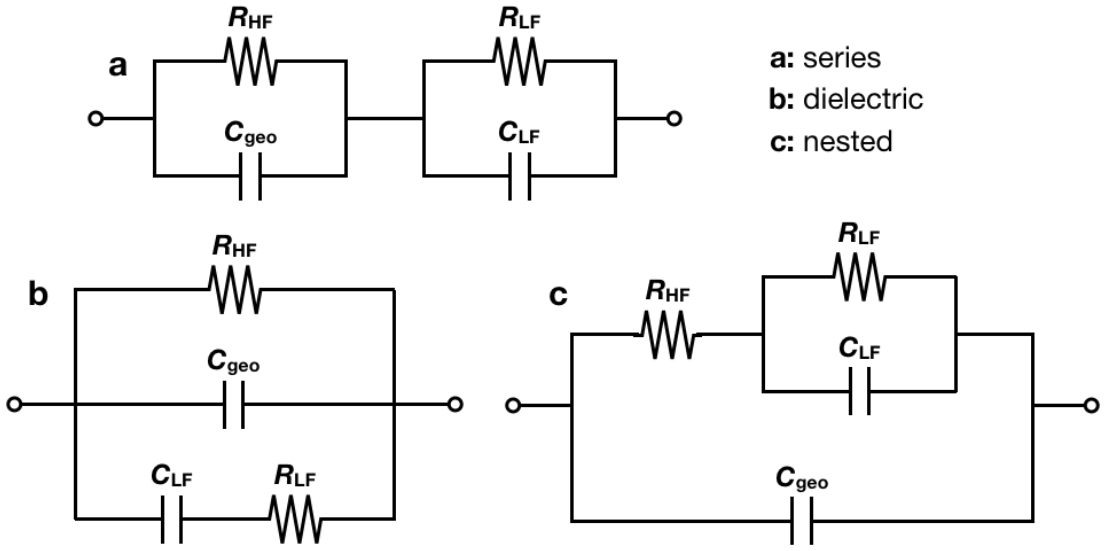

Figure 5.7. *Equivalent circuits modelling processes having two time constants: (a) series type connection, (b) dielectric relaxation circuit, (c) nested structure*

In Figure 5.7, three possibilities are illustrated: (a) Voight type series connection of two RC circuits, (b) a circuit generally modelling dielectric relaxation behavior, and (c) a nested circuit where a LF component directly coupled to HF resistance. As all three possibilities considered, adoption of series (a) meant that there is a process occurring outside of the perovskite layer (see C_{geo}) which is much slower than recombination in perovskite. This is highly unlikely when considering efficient carrier extraction through these layers, and also when noting high doping density of them. Any recombination or transport process through these selective layers should be very fast. Second circuit in (b) is a model of dielectric relaxation in materials. Although, such possibility is not completely disregarded, evidences on ionic migration are more abundant as it was pointed out in Section 2.3. Recombination process coupled to motion of defects (here ionic species) can be explained by using circuit (c). Therefore, a model employing a nested structure in Figure 5.7c was adopted.

As it is remarked earlier in Section 2.3, mobile ionic species can be thought as moving of defects through the perovskite layer. Such movement responding ac perturbation at LF regime might also be coupled to the recombination resistance in impedance model. Figure 5.7c indeed depicts this type of behavior where LF process associated RC circuit is connected in series to R_{HF}. It should be noted that more complex dependence

can be observed as well, as in [80]. Nevertheless, here it progresses with this type of circuit with slight modifications as it well explains the LF impedance response.

Overall model representing both HF and LF responses is provided in Figure 5.8. R_{LF} and C_{LF} are the LF resistance and the capacitance that is associated with the second semi-circle in Figure 5.6. In Figure 5.8, C_{LF} is shown by a CPE since it proved to be necessary by yielding dispersion parameters smaller than 0.8 i.e. $p < 0.8$. Fitting of the LF portion of the impedance spectra was quite unsuccessful when a constant R_{sh} (obtained by fitting to the HF model) was included by connecting it in parallel with C_{geo}. Therefore, it is discarded in LF model. No further assumptions are made on the nature of R_{sh} other than it seems constant in HF spectra and it is needed in order to explain the HF response in conjunction with recombination. More involved discussion can be found in the next chapter.

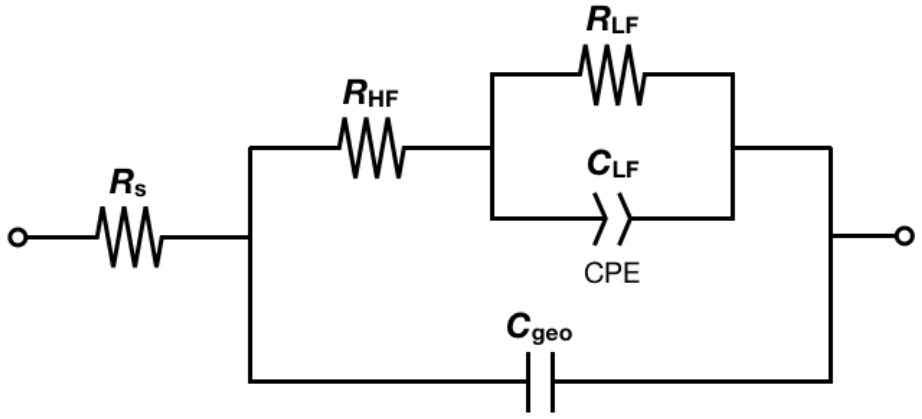

Figure 5.8. *Overall impedance model of PSCs*

Impedance spectra of a NiO_x-based device spanning frequency range of 10 Hz – 1MHz were fit to this model as in Figure 5.9. Result of the fitting with different illumination conditions is given here for the same NiO_x-based PSC, whose HF response is given in Figure 5.4b. In addition, fitting performance of the overall impedance model is presented in Figure 5.10, as R, $-X$ vs. frequency plots: (a) for a NiO_x-based device, (b) for a PEDOT:PSS-based device. Markers denote the experimental data and lines are the result of the fit. Note that the illumination intensity is 50% Sun equivalent.

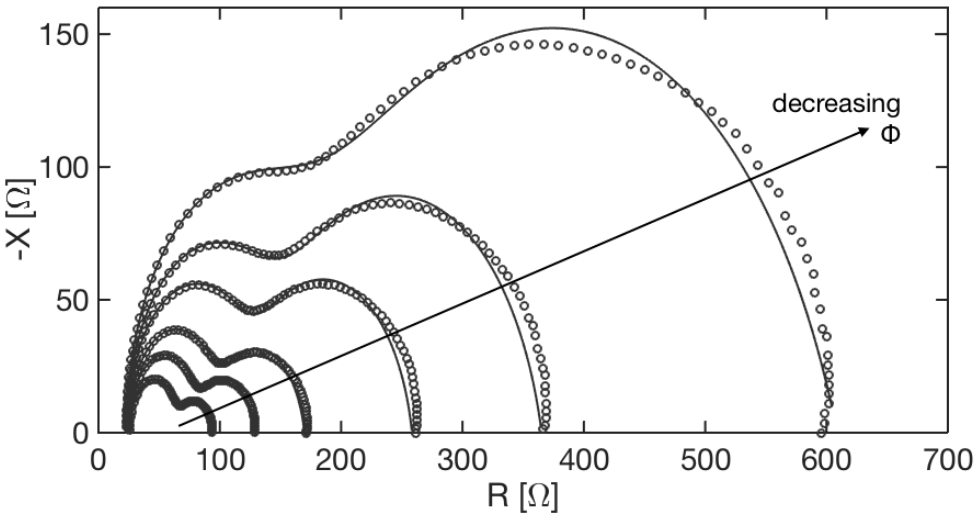

Figure 5.9. *Nyquist plots at different irradiance levels for a NiO_x-based PSC*

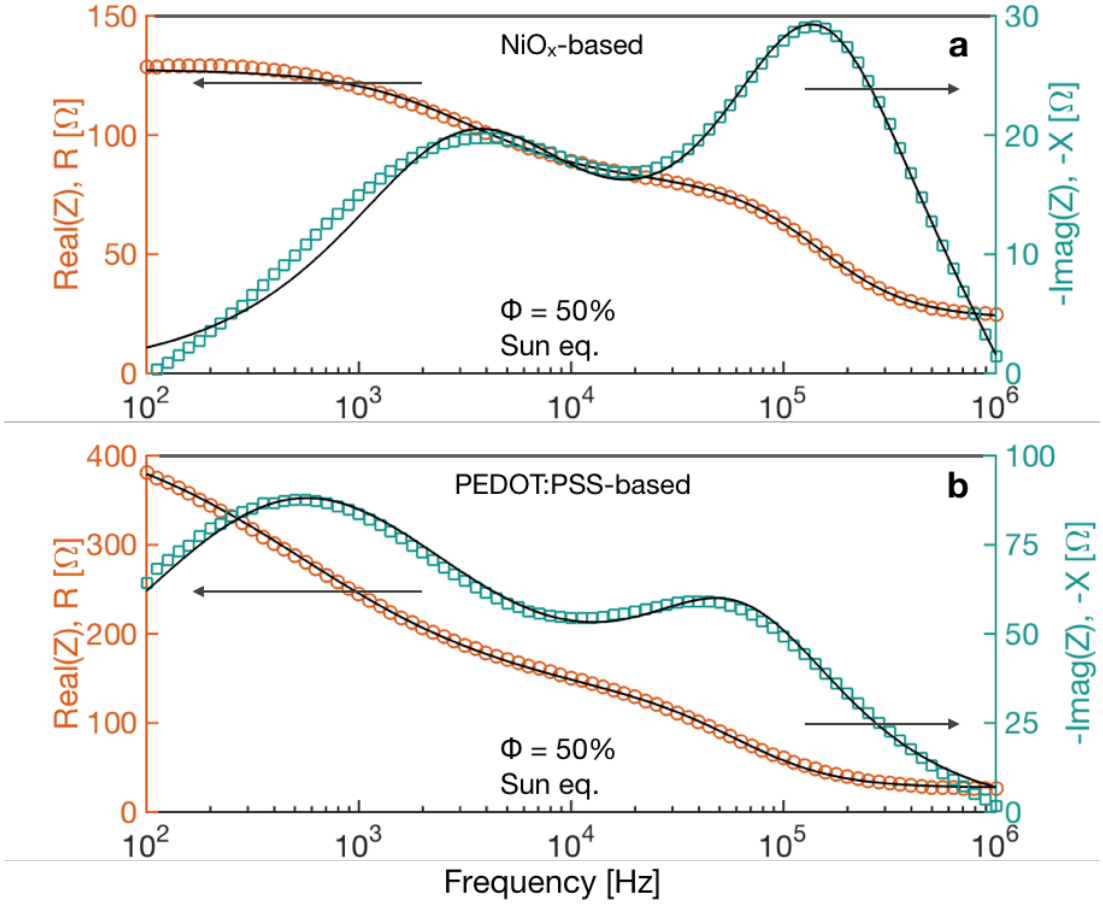

Figure 5.10. *Sample impedance spectra showing fitting accuracy*

In LF regions of NiO_x-based devices, the accuracy of the model decreases as evidenced by the Figure 5.10a. However, for PEDOT:PSS devices, smooth fitting can be obtained as in Figure 5.10b. The reduction in accuracy for NiO_x-based devices are not too critical since most of the information regarding the time constants is contained where reactance X makes a peak. In this mid-frequency region, the quality of the fit seems adequate. Nevertheless, introduction of extra components into the model would complicate the analysis and reduces the applicability of the model by causing over-parameterization. In this trade-off, simplicity was chosen over the fitting accuracy, and such choice is justified in Section 2.8. It deserves an emphasis that the current model is well applicable to both NiO_x and PEDOT:PSS-based devices as in Figure 5.10.

Fitting parameters calculated for different irradiance levels are given in Table 5.2 for LF response. The values were normalized for a 1 cm^2 device. In addition, the time constant of the LF process is presented i.e. $\tau_{LF} = R_{LF}C_{LF}$. This calculation is valid when $p > 0.8$, as it is explained in Chapter 2. Therefore, τ_{LF} was denoted as not applicable (i.e. NA) when $p < 0.8$. The parameters of HF response are virtually the same with Table 5.1 given before, hence, they are not repeated.

Table 5.2. *Parameters calculated by fitting to the overall impedance model*

Φ [OD]	R_{LF} [Ω]	p	C_{LF} [μF]	τ_{LF} [μs]
dark	7358	1.000	*NA*	*NA*
2.5	1886	0.555	*NA*	*NA*
2.1	518	0.566	*NA*	*NA*
1.7	169	0.624	*NA*	*NA*
1.4	79.2	0.711	*NA*	*NA*
1.2	50.3	0.709	*NA*	*NA*
1.0	30.9	0.794	2.37	73.3
0.9	24.7	0.816	2.69	66.5
0.8	19.4	0.837	3.14	61.0
0.7	15.0	0.858	3.76	56.4
0.6	10.2	0.841	5.18	52.7
0.5	8.5	0.800	5.88	50.2
0.4	6.2	0.892	8.48	52.8
0.3	5.3	0.869	8.99	48.0
0.2	3.7	0.872	14.4	54.0
0.1	3.2	0.882	13.9	44.2

Inspection of Table 5.2 reveals that τ_{LF} seems rather unchanged for a wide range of Φ, suggesting that there is a light-independent process observed in a moderate range of illumination. Similar observation was also made in [81] with much higher time

constants. In order to progress further, illumination dependence of R_{LF} should be evaluated, as in Figure 5.11. An obvious revelation is that R_{LF} is also inversely related to Φ, as it is the case for R_{HF} in HF through $R_{rec} \parallel R_{sh}$ configuration. This important observation suggests that the resistance associated with the LF process is in fact a recombination resistance, in consistence with the inverse relation of recombination resistance to illumination.

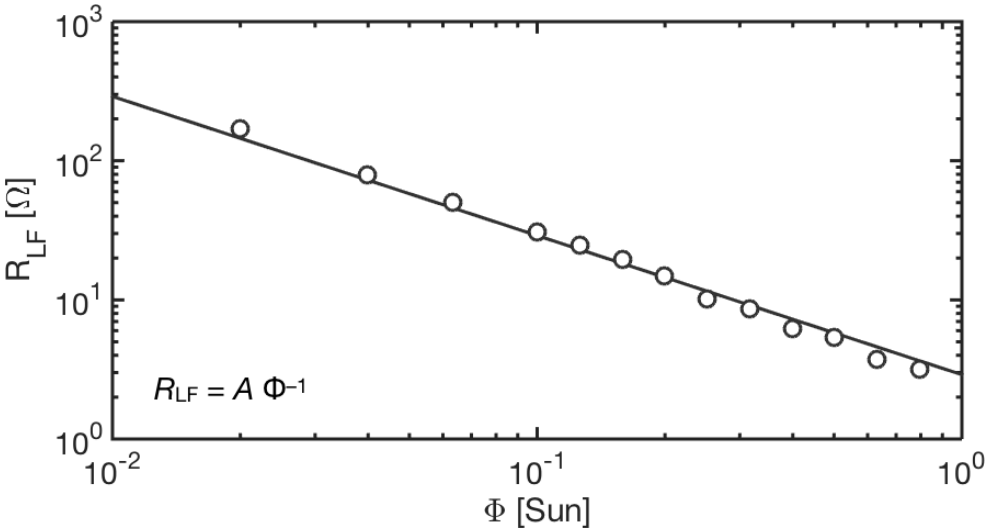

Figure 5.11. *Illumination dependence of low-frequency resistance R_{LF}*

In summary, a complete impedance model that depicts the impedance response of NiO_x-based PSCs of ITO / NiO_x / Perovskite / C_{60} / BCP / Ag architecture was developed. This model was shown to be applicable to PEDOT:PSS devices as well. By employing open-circuit conditions in which carrier generation is completely compensated by recombination, resistances in equivalent models have interpreted as the representations of underlying recombination processes—for both resistances connected to high and low frequency regimes. In order to evaluate the HF impedance response, a constant shunt resistance was introduced specifically for HF equivalent circuit. Finally, recombination process was shown to be coupled to a LF capacitive response that yields light-independent time constant. In the next chapter, analysis of impedance response of different PSCs was conducted, and relevant discussion was made.

CHAPTER 6

ANALYSIS OF IMPEDANCE SPECTRA AND DISCUSSION

This chapter is strongly connected to the previous one, in which a complete impedance model was developed for p–i–n heterojunction perovskite solar cells. Resistances governing the impedance response have shown to be correlated to recombination processes. In this chapter, significance of those findings was emphasized through the comparison of different cells. In addition, issues regarding the impedance spectra of those cells were elaborated.

6.1. Summary of Fabricated Perovskite Solar Cells

In the scope of this thesis, different solar cells were fabricated and characterized. They have p–i–n heterojunction configurations of HTL / Perovskite / ETL architecture. Here, they are separated into two groups in terms of their HTLs: Nickel oxide (NiO_x)-based and PEDOT:PSS-based. It should be emphasized that NiO_x is an inorganic material deposited by sputtering and PEDOT:PSS is an organic polymer mixture deposited by spin-coating from a dispersion. This remark will be relevant to subsequent discussions.

Table 6.1 summarizes the main photovoltaic (PV) performance parameters of 6 different cells whose impedance responses were analyzed. These cells were abbreviated according to their structures. All parameters were extracted from reverse scanned I–V plots measured at 98% Sun equivalent and they were given as the average values of 6 different pixels on a single substrate. Note that the efficiencies of best cells were also measured in maximum-power-point tracker (MPPT) whose design details

were given in Chapter 4. There was no deviation more than relative 10% of their standard I–V scan efficiency in 3 minutes at least.

Table 6.1. *Photovoltaic performance parameters of the studied PSCs*

Cell Abreviation	Structure	V_{OC} [V]	J_{SC} [mA/cm^2]	FF	%Efficiency
NX	ITO / NiO_x / Perovskite / C_{60} / BCP / Ag	0.81	16.23	63.3	8.52 ± 0.70
NT	ITO / NiO_x / polyTPD / Perovskite / C_{60} / BCP / Ag	0.85	14.72	69.2	9.11 ± 0.38
NP	ITO / NiO_x / PEDOT:PSS / Perovskite / C_{60} / BCP / Ag	0.86	15.95	68.3	9.69 ± 0.55
PX	ITO / PEDOT:PSS / Perovskite / C_{60} / BCP / Ag	0.76	10.79	56.3	5.10 ± 0.56
PT	ITO / PEDOT:PSS / polyTPD / Perovskite / C_{60} / BCP / Ag	0.82	7.76	47.6	3.08 ± 0.55
PTm	ITO / PEDOT:PSS / polyTPD (mod.) / Perovskite / C_{60} / BCP / Ag	0.86	15.33	69.3	9.30 ± 0.90

To indicate the type of cells, different abbreviations were used. The letter N, P, X, T, and Tm stands for, NiO_x, PEDOT:PSS, absence of any interlayer, poly-TPD, and modified poly-TPD, respectively. Modified poly-TPD means that the spin-coated poly-TPD layers were spin-washed with anhydrous chlorobenzene, possibly thinning the interlayer of poly-TPD down. Excluding PX and PT structures, all cells worked well with a decent fill factor, *FF* value. In the rest of the chapter, impedance responses of all these 6 cells were analyzed and the results were presented.

Inspection of the Table 6.1 reveals that there are noticeable changes in performance parameters by changing only the HTL layers. The top contact of all the devices were the same as they employ fullerene C_{60} ETL. In fact, fullerene derivatives renowned for their surface passivation properties in perovskite devices [82], [83]. Such employment of a fullerene C_{60} as the top contact allows the study of recombination with an emphasis on HTL / Perovskite interface.

6.2. Analysis of PEDOT:PSS Based Devices

When the device employing PEDOT:PSS layer only (PX) was fabricated, it yielded low efficiency of ~5%, as it is seen in Table 6.1. Poly-TPD has been utilized as an

extra p-type layer on top of PEDOT:PSS in the literature, especially in organic and quantum dot LEDs [84], [85] but also in PSCs [34]. Inspired by these studies, double HTL devices of PEDOT:PSS / poly-TPD (PT) was fabricated with lower efficiency values of ~3%. Then, this efficiency drop was thought to be associated to the low-doping, and hence low conductivity, of poly-TPD. Therefore, another set of devices employing thinned-down poly-TPD layers (PTm) were fabricated. This modification was carried out by spin-washing of presumably thick poly-TPD layers with anhydrous chlorobenzene. Significant efficiency enhancement was observed as PTm devices exhibit >9% efficiency. Finally, in order to understand the origin of efficiency increase, IS measurements were conducted on these devices.

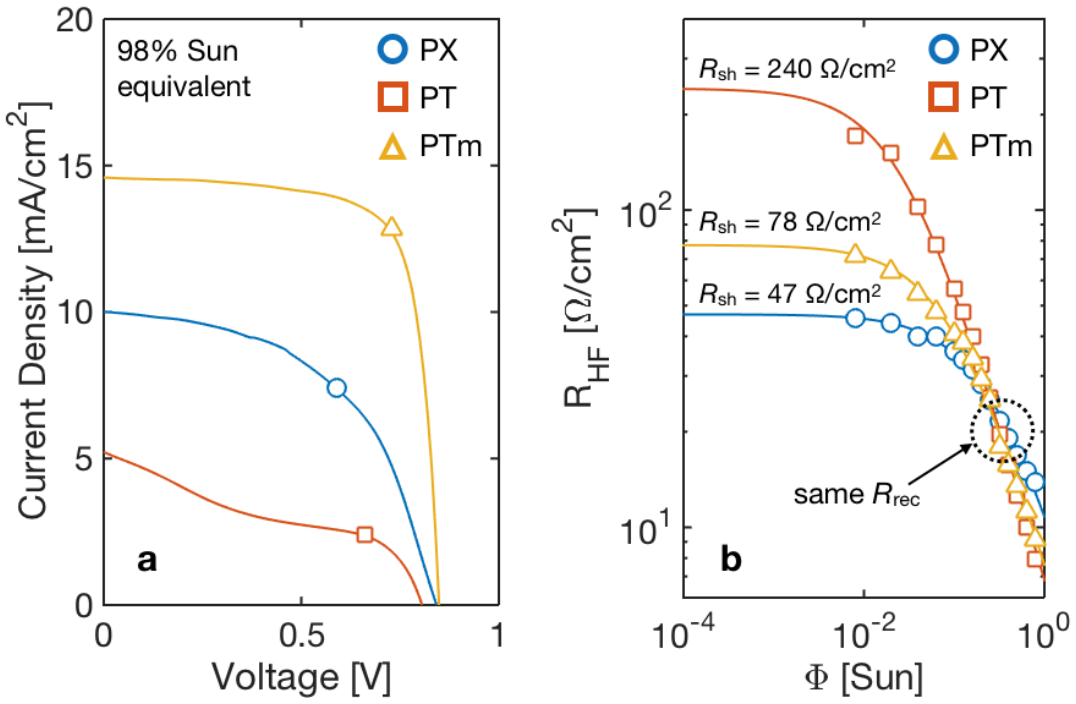

Figure 6.1. *A selection of I–V curves for PEDOT:PSS-based devices (a) and their R_{HF}–Φ characteristics (b)*

Current–voltage characteristics of a selection of PEDOT:PSS-based devices are shown in Figure 6.1a, where markers denote the maximum-power-points (MPP). I–V curves were obtained at forward scan. As it is seen from Figure 6.1a, there is a significant increase in efficiency for the device PTm compared to the base device PX. Yet, an efficiency drop was observed in device PT, in which a suboptimum poly-TPD layer

was deposited on PEDOT:PSS. The need for such modification of thinning-down can be ascribed to the low conductivity of thick poly-TPD layer.

In Figure 6.1b, the illumination dependence of HF resistance (R_{HF}) were given. Inspection reveals a considerable increase in shunt resistance for devices employing an interlayer of poly-TPD, i.e. PT and PTm. Yet their recombination resistances at high frequency seems to be comparable with no major change (recall that $R_{HF} = R_{rec} \parallel R_{sh}$ and R_{HF} goes to R_{rec} in high irradiance conditions). This situation is also the same in LF region for devices PX and PTm where R_{LF} values are comparable. The LF portion is not completely revealed in PT device. This is probably due to slowing down of the ionic migration in these devices. In order to resolve the LF feature completely, impedance measurements at lower frequency values should be made by a low-frequency impedance analyzer.

Overall, the efficiency enhancement due to modified poly-TPD layer deposited on PEDOT:PSS HTL has been ascribed to the increase in R_{sh}, and hence, to the reduction of shunt electrical pathways—not to the suppression of recombination that would be deducted otherwise, if the measurements were carried out only in low-illumination intensity. Comparing different devices in terms of their recombination-related properties without taking shunt leakage pathways into account might result in misinterpretation of the underlying recombination mechanism, which is masked by the present R_{sh}. When doing such IS measurements, it is important to carry out measurements in different steady-state conditions, either by changing the bias or the illumination or both. By doing so, different sets of impedance spectra should be analyzed. Only by this way, reliable comparisons between different devices can be made. Therefore, it should be stressed that this discussion is valuable, especially for emerging technologies employing solution processing methods.

Up to this point, no claims were made on the nature of these seemingly constant shunt resistances. However, it is certain that shunt resistance values of around ~30 $\Omega.cm^2$ observed in decently working devices (NiO_x-based ones mostly) seems to be too low and are inconsistent with the decent *FF* values. Here, it should be emphasized that R_{sh}

is extracted from HF ac measurements, not from DC measurements. In a material where grain boundaries are abundant, shunt electrical pathways can be directly connected to such boundaries. In addition, perovskites exhibit ionic conductor nature so that the ionic species respond to the electrical field. Therefore, there is a strong possibility that these grain boundaries are electrically active due to the accumulation (and/or depletion) of ionic species due to differences between bulk and surface potentials of individual grains. In fact, accumulation of ionic species on the grain boundaries were shown in [50] through the revelation of an anomalous photovoltaic effect. Overall, shunt resistance can exhibit a dynamic behavior such as by being frequency and voltage dependent. As a conclusion, R_{sh} value in HF ac measurements can be well below the shunt resistance associated to the DC, the condition that governs the operation of solar cells. Failure of LF fitting encountered when R_{sh} value obtained in HF portion is included in the complete impedance spectra is another argument that supports this point of view.

6.3. Analysis of Nickel Oxide Based Devices

Three different NiO_x-based devices were fabricated and studied as summarized in Table 6.1. Devices employing NiO_x layer only (NX) exhibits higher short-circuit current density J_{SC} but lower open-circuit voltage V_{OC} compared to the devices utilizing an extra interlayer of poly-TPD (NT) or PEDOT:PSS (NP) on top of NiO_x. Furthermore, the efficiency values of NT and NP devices were enhanced compared to the base device NX, as it is seen in Table 6.1.

The most stable devices in terms of their steady-state MPP stability, which is assessed by using developed MPPT (see Chapter 4), were used in the IS measurements. As a representative of cell performances, the I–V curves of these most stable devices are given in Figure 6.2. Noticeable hysteresis is present in all the devices, and it can be seen by noting the differences between forward scan (a) and reverse scan (b). An S-shaped kink is also observed in device NT around MPP of reverse scan as a result of hysteresis.

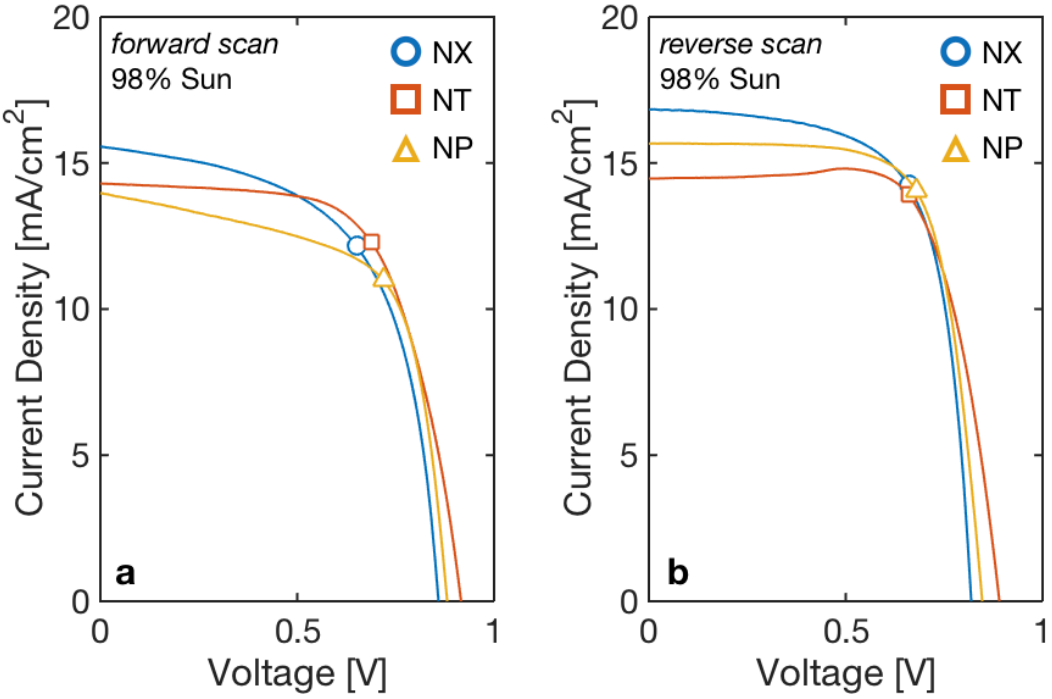

Figure 6.2. *The I–V curves of the most stable NiO_x-based PSCs: (a) forward scan, (b) reverse scan*

NiO_x HTLs were fabricated by magnetron sputtering technique, which is prone to result in non-stoichiometric composition. Such non-stoichiometry is in fact strongly correlated to the conductivity and hence the doping of NiO_x films [86]. In addition to the irregularities of ion vacancies or interstitials, inorganic oxides have surface trap states due to dangling bonds on the surface, distorting the local lattice symmetry. Passivation of interface states through introduction of organic interlayers can be found in the literature: [87], [88]. Study on the effects of such interlayers on the devices can be conducted through impedance spectroscopy (IS) since IS might give information on the underlying recombination mechanisms, if the results are analyzed properly. Inspired with these arguments, modification of HTL layer of NiO_x was carried out through the additional organic interlayers of p-type poly-TPD and PEDOT:PSS, followed by IS measurements of these devices.

In the previous chapter, analyzes were mostly conducted on NiO_x-based devices without interlayers, i.e. NX. It has been shown that both low and high frequency resistances (R_{HF} and R_{LF}), which are associated to the impedance spectra, are in fact

recombination resistances. An introduction of a shunt resistance R_{sh} was done in order to extract the true recombination resistance R_{rec} associated to high-frequency (HF) response such that $R_{HF} = R_{rec} \parallel R_{sh}$. The low-frequency (LF) resistance did not need the inclusion of such resistance, and it has shown inverse proportional dependence on irradiance Φ directly. At this point, intuition calls for the study and comparison of illumination dependence of these recombination resistances belonging NX, NT and NP.

Solar cells are devices that operate at steady-state conditions employing DC voltages and currents. But R_{HF} and R_{LF} are the response of the device to the perturbation of small voltage around the open-circuit voltage, and hence they are *differential* ac resistances. Considering the overall impedance model given in Figure 5.8 at DC conditions, the total DC recombination resistance R_{REC} can be written as the summation of both recombination resistances R_{rec} and R_{LF} i.e.

$$R_{REC} \equiv R_{rec} + R_{LF} \tag{6.1}$$

This is because the capacitive elements act as open-circuit in DC. Note that the total recombination resistance is denoted with subscript "REC" all in capitals and the HF recombination resistance employs "rec", all in lowercase letters. (This convention is used throughout the thesis where ac parameters were denoted with lowercases while DC components were shown with capitals.) The reasoning for being able to name R_{REC} a recombination resistance is that both resistances (R_{rec} and R_{LF}) scales linearly with Φ^{-1}, and therefore their summation (R_{REC}) is also proportional to Φ^{-1}.

Having established the notion of resistances associated to impedance response, the irradiance dependence of R_{HF} and R_{REC} is given in Figure 6.3 for devices NX and NT. The line of fit was extrapolated in order to facilitate the recognition of R_{sh} by the y-axis crossing. It should be noted that the results for the device NP are quite similar to NX in high-frequency, and to NT in both low-frequency and in terms of total recombination resistance R_{REC}. Hence, the results for NP were not shown in Figure 6.3 since it decreases the readability of the plots. See Figure 6.4 for a proper comparison.

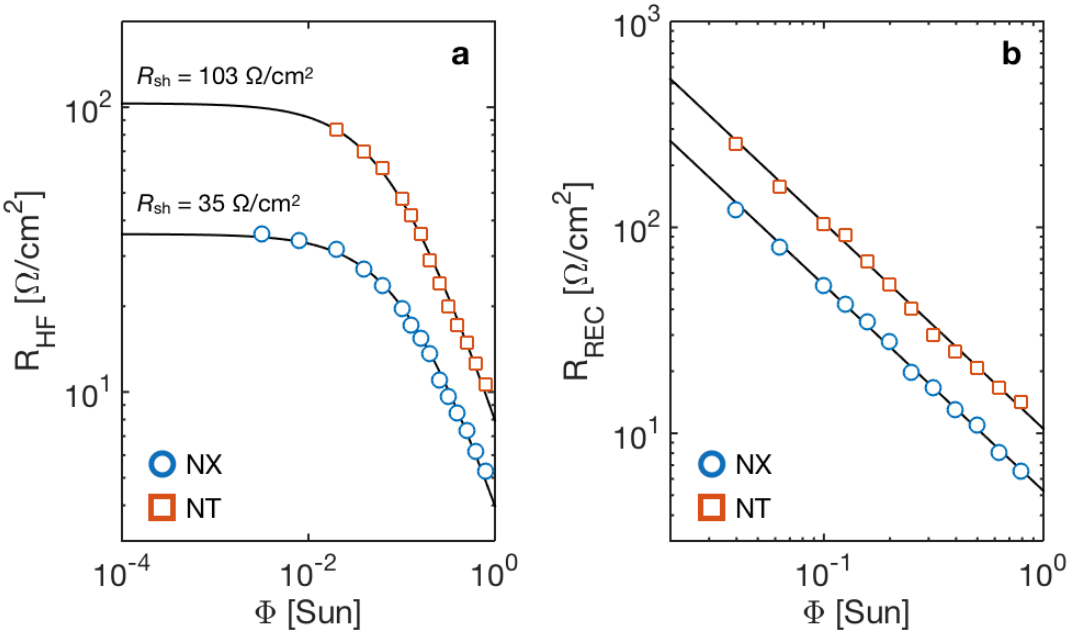

Figure 6.3. *The illumination dependence of R_{HF} (a) and R_{REC} (b) for NX and NT*

Figure 6.3 reveals that both R_{rec} and R_{REC} increased twofold when a poly-TPD interlayer was deposited on NiO_x HTL. This observation suggests that the underlying recombination process was suppressed by the introduction of a passivation layer. In addition, HF shunt resistance R_{sh} also increased in NT device compared to NX. Suppression of any shunt resistance by itself, acts as an improvement in the operation of the solar cell—like in the case of recombination resistance. So, introduction of poly-TPD layer improves the device performance through two ways: (i) increase in shunt resistance, (ii) suppression of dominant recombination process.

The passivation effect of PEDOT:PSS is demonstrated by Figure 6.4 where Nyquist plots of NX, NP and NT are given. By inspection of the semi-circles in Figure 6.4, it is evident that NP acts similar to NX in HF region and to NT in LF region. Yet, overall, both NT and NP devices exhibit decrease in recombination through the increase of R_{REC}. These observations are in line with the efficiency enhancement associated to poly-TPD and PEDOT:PSS passivation, as presented in Table 6.1.

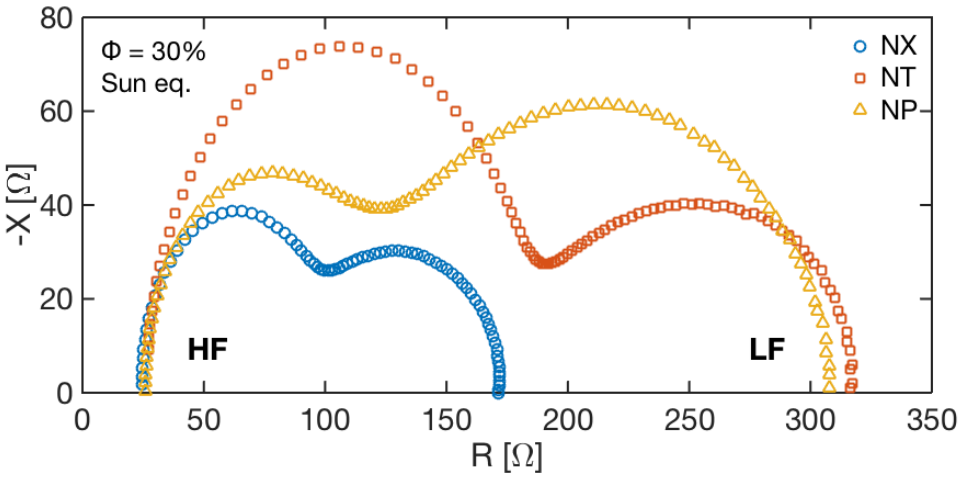

Figure 6.4. *The Nyquist plots of NX, NT and NP at 30% equivalent Sun*

For the case of NT and NP; their impedance spectra are distinctly different, but they result in the same DC recombination resistance R_{REC}. This hints at the possibility that introduction of a p-type interlayer covering the surface of NiO_x, modifies the recombination kinetics by *the same* means, although their impedance responses are dissimilar. Connecting this possibility to abundance of surface states in NiO_x layer implies that the recombination taking place at the NiO_x / Perovskite surface might be the dominant recombination mechanism in a NiO_x-based PSCs, like the device NX, but this surface might be passivated by the introduction of an organic interlayer.

The LF feature in the impedance spectra of PSCs revealed a dynamic capacitive response C_{LF} whose value changes with the irradiance (see Table 5.2) unlike the HF capacitive element C_{geo}, which remains constant due to its geometrical origin of dielectric perovskite layer. Therefore, the case for C_{LF} deserves special attention. First of all, irradiance dependence of the dispersion parameter p of constant phase element (CPE) associated with the LF feature should be evaluated. This dependence is illustrated in Figure 6.5a, with p-values obtained through the fitting of entire impedance spectra. Device without an interlayer (NX) attains a $p \sim 1$ while devices exhibiting an organic interlayer (NT and NP) demonstrates p-values tending to 0.5. As noted before in Section 2.7, p-values close to 1 is the sign of an ideal capacitive behavior whereas values tending to 0.5 are the indication of very time-dispersive behavior, and specifically, a diffusion process. Response of large ionic species to the

voltage perturbation in IS (as they move and diffuse), and their effect on the recombination dynamics could well induce such behavior. It seems that the introduction of a passivation layer on NiO_x changes the coupling of R_{LF} (and hence R_{REC}) from a capacitive response to a diffusive process.

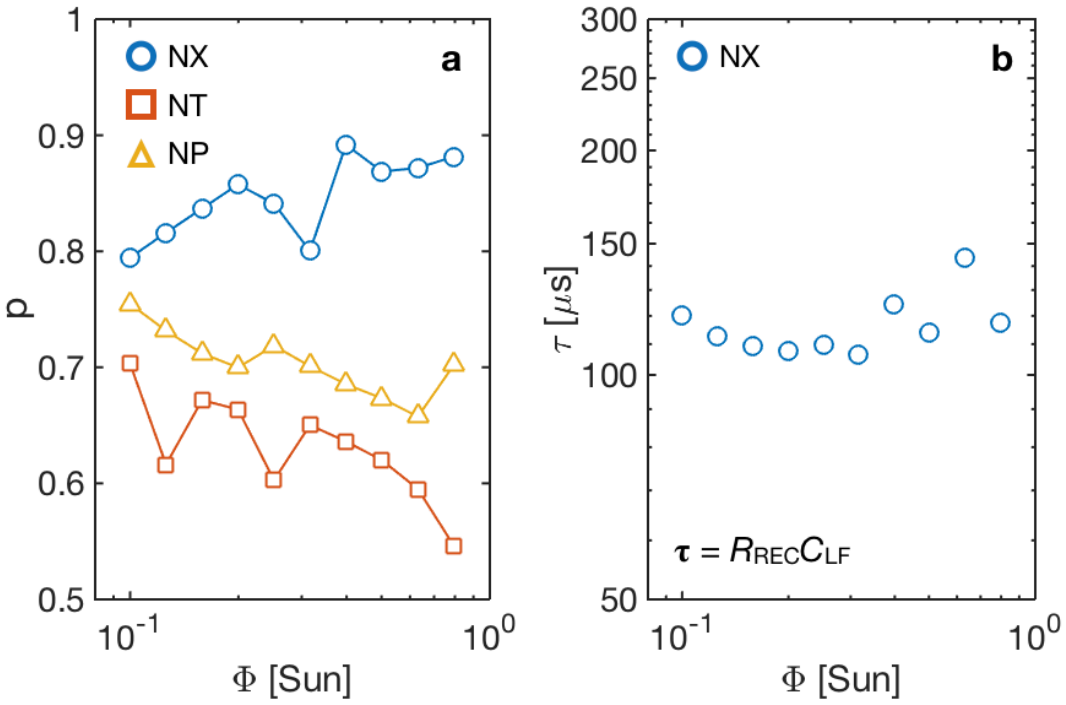

Figure 6.5. *Illumination dependence of (a) dispersion parameter p and (b) time constant τ*

Furthermore, the time constant τ obtained from the impedance response of the device NX is given in Figure 6.5b, which reveals an irradiance-independent time constant for the underlying capacitive process. It should be noted that τ is calculated as $\tau = R_{REC}C_{LF}$ where C_{LF} is the equivalent capacitance corresponding to the CPE element (and is calculated by using Equation 2.5). Similar calculation cannot be made for devices NT and NP since they exhibit *p*-values smaller than 0.75. Such calculation would be physically meaningless, as it is discussed in Section 2.7.

The independence of τ on Φ suggests a connection between the underlying recombination mechanism to the capacitive response C_{LF} through R_{REC}—unlike the case for C_{geo} and R_{rec} in high frequency since C_{geo} is naturally constant. Such

observation were also made in [81] in a very similar fashion. In this aforementioned study and in [89], the origin of the LF capacitive element C_{LF} was ascribed to the interfacial accumulation capacitance due to majority carriers. Same approach was also employed in this thesis, since the clear link of surface passivation of NiO_x was shown through the devices NT and NP. This surface passivation could be directly the cause of both the vanishing of the capacitive behavior having $p \sim 1$ and the emergence of a diffusive behavior having $p \sim 0.5$.

6.4. Discussion

Here, it has been hypothesized that the surface passivation of NiO_x using interfacial layers of poly-TPD and PEDOT:PSS resulted in the change of dominant recombination channel. The capacitive process observed in the NiO_x-only device was attributed to the formation of an accumulation capacitance (C_{acc}) in NiO_x / Perovskite interface. The large values of ~15μF/cm^2 attained for C_{LF} (see Table 5.2) are indicative of interfacial nature [81], since the accumulated carriers are confined to a geometrically thin region where band bending is substantial. Introduction of an interlayer on NiO_x seems to prevent this carrier accumulation, as it is evidenced by the change of dispersion parameter p from ~1 to ~0.5 in Figure 6.5a.

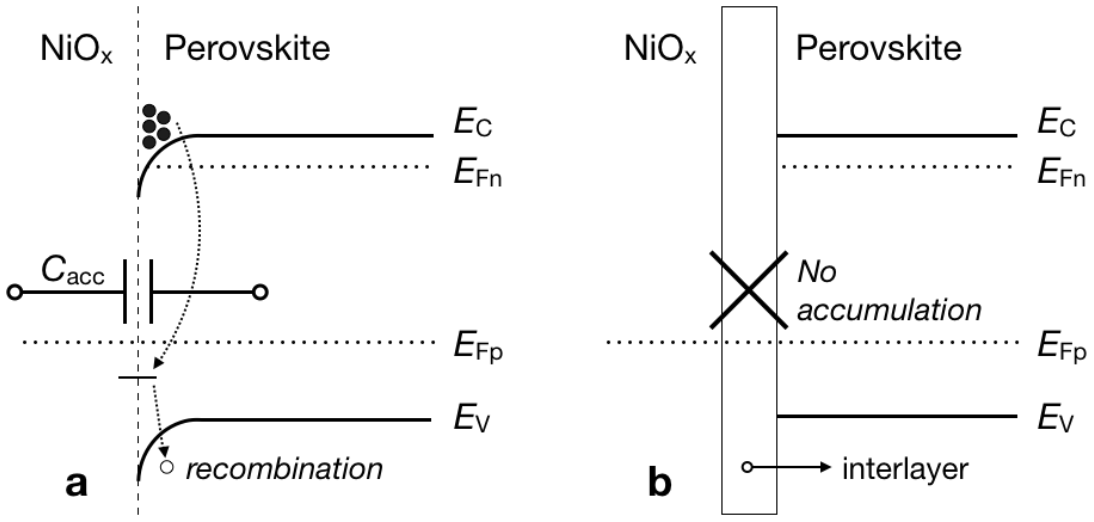

Figure 6.6. *Band diagram schematics for devices employing (a) unpassivated and (b) passivated NiO_x layers*

Schematic depiction of band diagrams of devices employing NiO_x-only and passivated NiO_x layers are given in Figure 6.6a and b, respectively. Diagrams are given assuming a flat-band condition for (b) for the ease of illustration. Then, accumulation of electrons causes the band bending in (a).

An illumination independent nature of low-frequency time constant was previously observed on (TiO_2/spiro-OMeTAD)-based and (PEDOT:PSS/PCBM)-based perovskite devices [81]. Similar reasoning was applied here as well: Assuming a weak to moderate n-type doping in perovskite absorber, as justified next, and recognizing the recombination on NiO_x surface as the dominant recombination channel, one may write:

$$J_{\mathrm{REC}} = q k_{\mathrm{r}} n_s' p_{\mathrm{s}} \tag{6.2}$$

where J_{REC} is the total recombination current density, k_{r} is the recombination coefficient, n_s' and p_{s} are the concentrations of majority electrons per unit area and of minority holes per unit volume at the surface, respectively. Note that the surface hole concentration p_{s} is dictated by the HTL of NiO_x due to the abundance of holes (i.e. p+-type doping). Simply put, p_{s} is both voltage and illumination independent since hole concentration is much larger than electron concentration in NiO_x. In terms of accumulated majority carriers, C_{acc} can be written as:

$$C_{\mathrm{acc}} = q \frac{dn_{\mathrm{s}}'}{dV} \tag{6.3}$$

Combining Equation 6.2 and 6.3, and by noting the voltage independence of p_{s}, the total recombination resistance $R_{\mathrm{REC}} = (dJ_{\mathrm{REC}} / dV)^{-1}$ (see Equation 5.2) can be expressed as follows:

$$R_{\mathrm{REC}} = \frac{1}{k_{\mathrm{r}} p_{\mathrm{s}} C_{\mathrm{acc}}} \tag{6.4}$$

Therefore, the time constant $\tau = R_{REC}C_{acc}$ attains a constant value because p_s is irradiance independent. Overall, τ value depicted on Figure 6.5b is illumination independent since C_{LF} is attributed to be equal to C_{acc}. It should be noted that, this result is valid regardless of the relation between R_{REC} and Φ. Furthermore, it is well-established thus far that R_{REC} is inversely proportional to Φ, which, in turn, necessitates that C_{acc} is proportional to Φ. That is the natural result of the performed derivation. And it is intuitively accurate that n_s' scales with Φ linearly, giving rise to the linear relation between C_{acc} and Φ.

In order to rationalize the claims regarding the domination of surface recombination due to unpassivated NiO_x HTL, light ideality factor measurements were conducted for both NiO_x-only and NiO_x / poly-TPD devices, NX and NT, respectively. Prior to the results, a theoretical framework is established.

In the ideal case of only radiative (band-to-band) recombination, organic-inorganic hybrid perovskites (OIHP) are limited to have ~1.3 V open-circuit voltage V_{OC} [90]. Examination of V_{OC} values in Table 6.1 suggest that there is considerable amount of voltage loss due to non-radiative recombination channels. Therefore, the case of radiative recombination is disregarded. One way to identify the dominant recombination mechanism in a solar cell is to measure the photocurrent–voltage ideality factor. Adapted from Equation 2.1, one may write:

$$V_{OC} = \frac{mk_B T}{q} \ln\left(\frac{J_{ph}}{J_0}\right) \tag{6.5}$$

where m is the ideality factor. This value can take different values depending on the recombination mechanism. For instance, for a trap mediated (i.e. Shockley-Read-Hall, SRH) recombination in a moderately-doped semiconductor, m = 1 for low-level injection, and m = 2 for high-level injection. Derivation of ideality factor for these two cases is given in Appendix, by assuming mid-gap trap states. Modification of Equation 6.5 yields:

$$\frac{\partial V_{\mathrm{OC}}}{\partial(\ln \Phi)} = \frac{m k_{\mathrm{B}} T}{q} \tag{6.6}$$

which states that the slope associated to the semilogarithmic plot of illumination dependence of V_{OC} directly yields the ideality factor m. Note that this expression was written by noting the proportional relation between the photocurrent J_{ph} and irradiance Φ. Illumination dependence of V_{OC} of devices NX and NT is given in Figure 6.7.

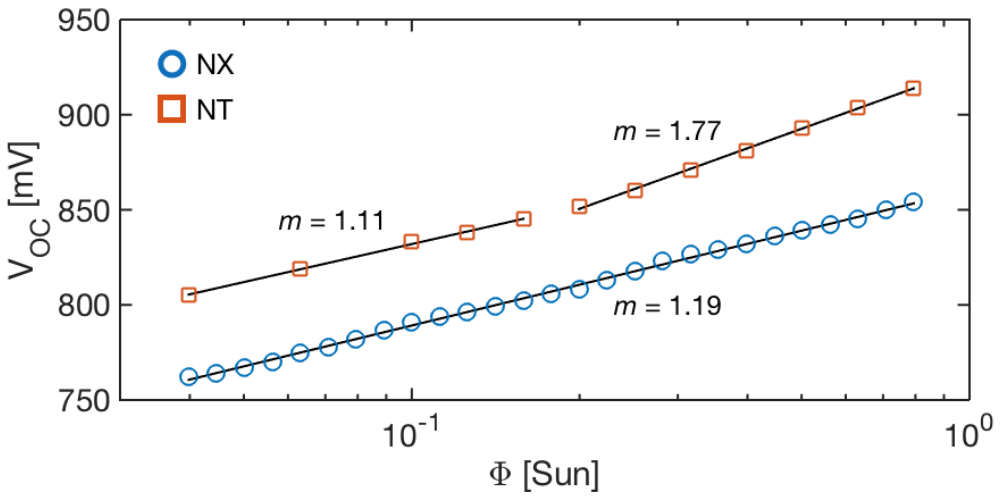

Figure 6.7. *Illumination dependence of V_{OC} for NX and NT*

As seen in Figure 6.7, besides the apparent increase in V_{OC} when poly-TPD interlayer was used, the device NT exhibits larger ideality factor in moderate to high illumination condition. In the lower excitation region, it has an ideality factor comparable to NiO_x-only device NX. Increase of m in NT can be interpreted by following reasoning: At low illumination condition, either electrons or holes are much greater than their counterpart such that $n \gg p$, or vice versa. Here, n and p are the free carrier densities of electrons and holes, respectively. In such condition, m tends to 1 for SRH recombination. However, when Φ increases, carrier concentrations become comparable i.e. $n \sim p$. Then m tends to 2. Given the probable low-doped nature of perovskite layer (ideally intrinsic), high excitation limit can be low, e.g. illumination of ~0.2 Sun equivalent for the case given in Figure 6.7.

In order to explain the change in recombination mechanism, a certain amount of n-type doping of perovskite absorber was assumed. Then, the expression regarding the accumulation capacitance in Equation 6.3 was introduced accordingly. As pointed out earlier in Section 2.1, perovskites were observed to exhibit n-type behavior in PbI_2-rich conditions. The fabrication method employed in this study is a sequential method in which a PbI_2 evaporation is followed by spin-coating of MAI on top of ~220 nm PbI_2 layer (see Section 3.1 for fabrication details). When a relatively thick PbI_2 of 280 nm was used, devices showed poor performance. SEM micrographs revealed a layer of unreacted PbI_2 just below the perovskite capping layer. It suggests that the reaction between PbI_2 and MAI is limited by the amount of and/or diffusion of MAI. This deduction, in turn, indicates the possible PbI_2-rich composition and therefore, n-type doping of perovskite—justifying the assumption of a weak to moderate n-type doping.

Overall, the suggestion of surface passivation of NiO_x by poly-TPD and PEDOT:PSS layers as the reason of suppression of dominant recombination mechanism can be summarized by the means of findings presented in Chapter 5 and 6. It should be emphasized that no claims were made on the certainty of the following rationale. It is a hypothesis that accurately explains the open-circuit impedance behavior of NiO_x-based PSCs in terms of internal dynamics of charge carriers and ionic species. Throughout the summary relevant referrals are made through footnotes.

When an intimate contact between the n-type perovskite and p-type NiO_x is formed, majority carriers of electrons are accumulated on the surface under illumination[a]. Accumulation of electrons give rise to a low-frequency capacitive response readily observed in IS measurements[b]. This capacitive response shows minor time dispersion, with a p-value of approximately 0.9[c] allowing a calculation of equivalent capacitance C_{LF}. Large values of C_{LF} and its linear dependence on irradiance[d] validates the origin of electron accumulation. Since electrons are confined to a very thin region, $n \gg p$ in this very region regardless of the illumination intensity upon the device. Light ideality

[a] Figure 6.6a
[b] Figure 6.4
[c] Figure 6.5a
[d] Table 5.2

factor of ~1, which is extracted from illumination dependence of open-circuit voltage[e], agrees with carrier concentration condition[f] of $n \gg p$. Due to the abundance of accumulated carriers and surface states on NiO_x, surface recombination is the dominant recombination mechanism in NiO_x-only devices. Introduction of thin interlayers of poly-TPD and PEDOT:PSS changes the dominant recombination mechanism by suppression of surface recombination.

When a thin passivation layer is deposited between the NiO_x and perovskite, no charge accumulation takes place[g]. Instead the low-frequency recombination resistance is now coupled to a capacitive process exhibiting a noticeable time dispersion of *p*-value tending to 0.5[h]. Dispersion parameter close to 0.5 are indicative of Warburg element modelling a diffusion process[i]. The large *Q*-values (at least an order of magnitude higher than the ones obtained in NiO_x-only devices) attained in the low-frequency CPE fitting suggests that the underlying capacitive process is connected to the ionic species responding to the ac perturbation in IS measurements. In the bulk of perovskite, $n \gg p$ and $n \sim p$ for low and high illumination, respectively. Changing of light ideality factor from ~1 to ~2 as the irradiance increases[e] falls in line with the change of carrier concentrations as *n* and *p* overlap in high illumination[f]. On the whole, dominant recombination mechanism is now Shockley-Read-Hall taking place in the bulk, which is unlike the surface recombination in NiO_x-only devices. The effect of surface passivation is directly observed by the increase of the open-circuit voltage and efficiency in passivated devices compared to the base device having unpassivated NiO_x layer[j]. Enhancement of total recombination resistance[k] also agrees well with the preceding discussion.

---

[e] Figure 6.7
[f] Equation A6 in Appendix
[g] Figure 6.6b
[h] Figure 6.5a
[i] Section 2.7
[j] Table 6.1
[k] Figure 6.3b

CHAPTER 7

CONCLUSION AND FUTURE OUTLOOK

The impedance response of planar p–i–n heterojunctions employing NiO_x and PEDOT:PSS layers is modelled. This model was shown to be accurate by IS measurements at different irradiance levels. Both high and low-frequency impedance features were shown to be linked to the recombination process. While the high-frequency recombination response is coupled to the geometrical capacitance of the cell, the low-frequency one is coupled either to a charge accumulation process or to the motion of ionic species. This finding emphasizes the applicability of IS for the deconvolution of different processes composing the complex impedance response.

Impedance analyses of two different sets of PSCs were made. Devices employing PEDOT:PSS-only were shown to be suffering from shunt leakage pathways. Proper modification by an interlayer of poly-TPD improved the shunt resistance, and, in turn, boosted the efficiency. No surface passivation effect was observed for these devices. The case was quite different for NiO_x-based devices.

All devices based on sputtered NiO_x layers worked with decent efficiencies. However, devices employing organic interlayers on top of NiO_x exhibited higher V_{OC} values, in addition to an apparent increase in efficiency. These enhancements were shown to be due to the passivation of NiO_x surface through the set of IS experiments. It is deducted that unpassivated NiO_x layers causes a formation of carrier accumulation on the surface. The disappearance of the accumulation capacitance in devices employing interlayers have strengthened this deduction and implied the change of dominant recombination channel from surface to bulk. Illumination dependence of the light

ideality factors of the devices indicated the suppression of surface recombination. Overall, this thesis presents a study in which the surface recombination in NiO_x-based PSCs is suppressed by introduction of organic interlayers. It should be noted that both the application and analysis of passivation of NiO_x surface with poly-TPD and PEDOT:PSS are novelties original to this work—to the best of the author's knowledge.

It is believed that the study presented in this thesis contributes to the understanding of perovskite device physics. But further investigation is needed in order to provide with a more complete impedance model. The overall equivalent circuit presented in this thesis was verified to be modelling the impedance response of PSCs in open-circuit under illumination. Such conditions were chosen to directly probe the recombination dynamics. However, impedance response of PSCs should also be resolved at different bias voltages. Only by this way a comprehensive model can be constructed. In addition, studies on lower frequency regimes are needed. It should be noted that this necessitates superior stability of devices due to the long data acquisition times in μHz–mHz range. Voltage dependence of impedance response and low-frequency regime will be studied in future works.

The origin of the shunt resistance observed in high-frequency regime needs to be clarified. Such revelation might provide the methods to suppress leakage current in devices. If the contribution of electrically active grain boundaries to shunt pathways are significant, then proper techniques of passivation of grain boundaries needs to be developed.

The significant difference between the efficiency values (~10%) obtained in the scope of this thesis and the ones commonly presented in the literature (>15%) can be due to sub-optimum perovskite layer quality. Similar passivation study for more efficient devices can result in favorable efficiency enhancements as well. So, impedance modelling of high-efficiency devices and the analysis of impedance response with respect to different device architectures should be conducted. Passivation of other transport layers, especially of oxides such as titanium dioxide, can be studied with IS.

Superior passivation techniques seem to be needed in order for the efficiency of PSCs to be increased further. In addition, proper control of doping in perovskites is necessary for an all-around management of device dynamics. For an optimized performance, the process of ionic migration and its relation to device operation and stability should be well-understood as well.

REFERENCES

[1] G. W. Crabtree and N. S. Lewis, “Solar energy conversion,” *Phys. Today*, vol. 60, no. 3, pp. 37–42, 2007.

[2] J. Bartos and A. Robertson, “Energy Supply Security: Emergency Response of IEA Countries,” 2014.

[3] N. M. Haegel *et al.*, “Terawatt-scale photovoltaics: Trajectories and challenges.,” *Science*, vol. 356, no. 6334, pp. 141–143, 2017.

[4] E. Becquerel, “Mémoire sur les effets électriques produits sous l’influence des rayons solaires,” *Comptes Rendus*, vol. 9, pp. 561–567, 1839.

[5] C. E. Fritts, “On the fritts selenium cells and batteries,” *Van Nostrands Eng. Mag.*, vol. 32, pp. 388–395, 1885.

[6] “This Month in Physics History: April 25, 1954: Bell Labs Demonstrates the First Practical Silicon Solar Cell,” *APS News*, vol. 18, no. 4, 2009.

[7] Fraunhofer ISE, “Photovoltaics report,” 2018.

[8] D. M. Bagnall and M. Boreland, “Photovoltaic technologies,” *Energy Policy*, vol. 36, no. 12, pp. 4390–4396, 2008.

[9] “Best Research-Cell Efficiency Chart,” *National Renewable Energy Laboratory*, 2018. [Online]. Available: https://www.nrel.gov/pv/. [Accessed: 19-Jul-2018].

[10] W. Shockley and H. J. Queisser, “Detailed balance limit of efficiency of p-n junction solar cells,” *J. Appl. Phys.*, vol. 32, no. 3, pp. 510–519, 1961.

[11] M. A. Green, “Third generation photovoltaics: Ultra-high conversion efficiency at low cost,” *Prog. Photovoltaics Res. Appl.*, vol. 9, no. 2, pp. 123–135, 2001.

[12] “GCell.” [Online]. Available: https://gcell.com. [Accessed: 19-Jul-2018].

[13] A. Kojima, K. Teshima, Y. Shirai, and T. Miyasaka, “Organometal halide perovskites as visible-light sensitizers for photovoltaic cells,” *J. Am. Chem. Soc.*, vol. 131, no. 17, pp. 6050–6051, 2009.

[14] M. M. Lee, J. Teuscher, T. Miyasaka, T. N. Murakami, and H. J. Snaith, “Efficient hybrid solar cells based on meso-superstructured organometal halide

perovskites," *Science*, vol. 338, no. 6107, pp. 643–647, 2012.

[15] "Perovskite Mineral Data." [Online]. Available: http://webmineral.com/data/Perovskite.shtml#.W1cc4S2B0WI. [Accessed: 24-Jul-2018].

[16] H. S. Kim *et al.*, "Lead iodide perovskite sensitized all-solid-state submicron thin film mesoscopic solar cell with efficiency exceeding 9%," *Sci. Rep.*, 2012.

[17] S. Brittman, G. W. P. Adhyaksa, and E. C. Garnett, "The expanding world of hybrid perovskites: Materials properties and emerging applications," *MRS Commun.*, vol. 5, no. 1, pp. 7–26, 2015.

[18] M. A. Green, Y. Hishikawa, E. D. Dunlop, D. H. Levi, J. Hohl-Ebinger, and A. W. Y. Ho-Baillie, "Solar cell efficiency tables (version 51)," *Prog. Photovoltaics Res. Appl.*, vol. 26, no. 1, pp. 3–12, 2018.

[19] L. M. Herz, "Charge-Carrier Mobilities in Metal Halide Perovskites: Fundamental Mechanisms and Limits," *ACS Energy Lett.*, vol. 2, no. 7, pp. 1539–1548, 2017.

[20] D. Kiermasch *et al.*, "Improved charge carrier lifetime in planar perovskite solar cells by bromine doping," *Sci. Reports, Publ. online 16 December 2016; | doi10.1038/srep39333*, 2016.

[21] J. H. Noh, S. H. Im, J. H. Heo, T. N. Mandal, and S. Il Seok, "Chemical management for colorful, efficient, and stable inorganic-organic hybrid nanostructured solar cells," *Nano Lett.*, vol. 13, no. 4, pp. 1764–1769, 2013.

[22] S. D. Stranks *et al.*, "Electron-hole diffusion lengths exceeding 1 micrometer in an organometal trihalide perovskite absorber," *Science*, 2013.

[23] G. Xing *et al.*, "Long-range balanced electron-and hole-transport lengths in organic-inorganic CH3NH3PbI3," *Science*, vol. 342, no. 6156, pp. 344–347, 2013.

[24] T. Leijtens *et al.*, "Electronic properties of meso-superstructured and planar organometal halide perovskite films: Charge trapping, photodoping, and carrier mobility," *ACS Nano*, 2014.

[25] C. Wehrenfennig, G. E. Eperon, M. B. Johnston, H. J. Snaith, and L. M. Herz, "High charge carrier mobilities and lifetimes in organolead trihalide perovskites," *Adv. Mater.*, 2014.

[26] N. G. Park, "Perovskite solar cells: An emerging photovoltaic technology," *Mater. Today*, vol. 18, no. 2, pp. 65–72, 2015.

[27] Y. Chen, M. He, J. Peng, Y. Sun, and Z. Liang, "Structure and Growth Control

of Organic-Inorganic Halide Perovskites for Optoelectronics: From Polycrystalline Films to Single Crystals," *Adv. Sci.*, 2016.

[28] M. Grätzel, "The light and shade of perovskite solar cells," *Nature Materials*, vol. 13, no. 9. pp. 838–842, 2014.

[29] M. A. Green, A. Ho-Baillie, and H. J. Snaith, "The emergence of perovskite solar cells," *Nature Photonics*. 2014.

[30] M. A. Green and A. Ho-Baillie, "Perovskite Solar Cells: The Birth of a New Era in Photovoltaics," *ACS Energy Letters*. 2017.

[31] J. H. Heo *et al.*, "Efficient inorganic-organic hybrid heterojunction solar cells containing perovskite compound and polymeric hole conductors," *Nat. Photonics*, 2013.

[32] M. Liu, M. B. Johnston, and H. J. Snaith, "Efficient planar heterojunction perovskite solar cells by vapour deposition," *Nature*, 2013.

[33] S. X. Tao, X. Cao, and P. A. Bobbert, "Accurate and efficient band gap predictions of metal halide perovskites using the DFT-1/2 method: GW accuracy with DFT expense," *Sci. Rep.*, vol. 7, no. 1, 2017.

[34] C. Momblona *et al.*, "Efficient methylammonium lead iodide perovskite solar cells with active layers from 300 to 900 nm," *APL Mater.*, 2014.

[35] Z. Xiao, Q. Dong, C. Bi, Y. Shao, Y. Yuan, and J. Huang, "Solvent Annealing of Perovskite-Induced Crystal Growth for Photovoltaic-Device Efficiency Enhancement," *Adv. Mater.*, vol. 26, no. 37, pp. 6503–6509, 2014.

[36] W.-J. Yin, J.-H. Yang, J. Kang, Y. Yan, and S.-H. Wei, "Halide perovskite materials for solar cells: a theoretical review," *J. Mater. Chem. A*, vol. 3, no. 17, pp. 8926–8942, 2015.

[37] J. Huang, Y. Yuan, Y. Shao, and Y. Yan, "Understanding the physical properties of hybrid perovskites for photovoltaic applications," *Nature Reviews Materials*. 2017.

[38] Q. Lin, A. Armin, R. Chandra, R. Nagiri, P. L. Burn, and P. Meredith, "Electro-optics of perovskite solar cells," *Nat. Photonics*, 2014.

[39] V. D'Innocenzo *et al.*, "Excitons versus free charges in organo-lead tri-halide perovskites," *Nat. Commun.*, 2014.

[40] G. Giorgi, J. I. Fujisawa, H. Segawa, and K. Yamashita, "Small photocarrier effective masses featuring ambipolar transport in methylammonium lead iodide perovskite: A density functional analysis," *J. Phys. Chem. Lett.*, 2013.

[41] A. Miyata *et al.*, “Direct measurement of the exciton binding energy and effective masses for charge carriers in organic-inorganic tri-halide perovskites,” *Nat. Phys.*, vol. 11, no. 7, pp. 582–587, 2015.

[42] Q. Wang *et al.*, “Qualifying composition dependent p and n self-doping in CH3NH3PbI3,” *Appl. Phys. Lett.*, vol. 105, no. 16, 2014.

[43] J. M. Ball and A. Petrozza, “Defects in perovskite-halides and their effects in solar cells,” *Nat. Energy*, vol. 1, no. 11, 2016.

[44] D. Bi *et al.*, “Efficient luminescent solar cells based on tailored mixed-cation perovskites,” *Sci. Adv.*, 2016.

[45] T. M. Brenner, D. A. Egger, L. Kronik, G. Hodes, and D. Cahen, “Hybrid organic - Inorganic perovskites: Low-cost semiconductors with intriguing charge-transport properties,” *Nature Reviews Materials*. 2016.

[46] H. J. Snaith *et al.*, “Anomalous hysteresis in perovskite solar cells,” *J. Phys. Chem. Lett.*, 2014.

[47] B. Chen, M. Yang, S. Priya, and K. Zhu, “Origin of J-V Hysteresis in Perovskite Solar Cells,” *Journal of Physical Chemistry Letters*. 2016.

[48] M. N. F. Hoque *et al.*, “Polarization and Dielectric Study of Methylammonium Lead Iodide Thin Film to Reveal its Nonferroelectric Nature under Solar Cell Operating Conditions,” *ACS Energy Lett.*, vol. 1, no. 1, pp. 142–149, May 2016.

[49] Z. Xiao *et al.*, “Giant switchable photovoltaic effect in organometal trihalide perovskite devices,” *Nat. Mater.*, vol. 14, no. 2, pp. 193–197, 2015.

[50] Y. Yuan, T. Li, Q. Wang, J. Xing, A. Gruverman, and J. Huang, “Anomalous photovoltaic effect in organic-inorganic hybrid perovskite solar cells,” *Sci. Adv.*, 2017.

[51] S. N. Habisreutinger, D. P. McMeekin, H. J. Snaith, and R. J. Nicholas, “Research Update: Strategies for improving the stability of perovskite solar cells,” *APL Mater.*, vol. 4, no. 9, 2016.

[52] N.-K. Kim *et al.*, “Investigation of Thermally Induced Degradation in CH3NH3PbI3 Perovskite Solar Cells using In-situ Synchrotron Radiation Analysis,” *Sci. Rep.*, vol. 7, no. 1, p. 4645, 2017.

[53] R. B. Dunbar *et al.*, “How reliable are efficiency measurements of perovskite solar cells? the first inter-comparison, between two accredited and eight non-accredited laboratories,” *J. Mater. Chem. A*, vol. 5, no. 43, pp. 22542–22558, 2017.

[54] W. H. Mulder, J. H. Sluyters, T. Pajkossy, and L. Nyikos, “Tafel current at

fractal electrodes. Connection with admittance spectra," *J. Electroanal. Chem.*, vol. 285, no. 1–2, pp. 103–115, 1990.

[55] R. S. Rodgers, "Another Way to View the CPE - ZARCs." [Online]. Available: http://www.consultrsr.net/resources/eis/zarc.htm#eqn3. [Accessed: 11-Aug-2018].

[56] M. E. Orazem, P. Shukla, and M. A. Membrino, "Extension of the measurement model approach for deconvolution of underlying distributions for impedance measurements," in *Electrochimica Acta*, 2002.

[57] M. E. Orazem and B. Tribollet, *Electrochemical Impedance Spectroscopy*, 2nd ed. 2017.

[58] J. Bisquert and F. Fabregat-Santiago, "IMPEDANCE SPECTROSCOPY: A GENERAL INTRODUCTION AND APPLICATION TO DYE-SENSITIZED SOLAR CELLS," in *Dye-sensitized Solar Cells*, 2010.

[59] W. Lai, "Impedance Spectroscopy as a Tool for the Electrochemical Study of Mixed Conducting Ceria," California Institute of Technology, 2007.

[60] "Documentation: fminsearch." [Online]. Available: https://www.mathworks.com/help/matlab/ref/fminsearch.html. [Accessed: 10-Aug-2018].

[61] J. C. Lagarias, J. A. Reeds, M. H. Wright, and P. E. Wright, "Convergence Properties of the Nelder--Mead Simplex Method in Low Dimensions," *SIAM J. Optim.*, 1998.

[62] "Documentation: Evaluating Goodness of Fit." [Online]. Available: https://www.mathworks.com/help/curvefit/evaluating-goodness-of-fit.html. [Accessed: 10-Aug-2018].

[63] Q. Chen *et al.*, "The optoelectronic role of chlorine in CH3NH3PbI3(Cl)-based perovskite solar cells," *Nat. Commun.*, 2015.

[64] E. Zimmermann *et al.*, "Characterization of perovskite solar cells: Towards a reliable measurement protocol," *APL Mater.*, 2016.

[65] J. A. Christians, J. S. Manser, and P. V. Kamat, "Best practices in perovskite solar cell efficiency measurements. Avoiding the error of Making Bad Cells Look Good," *Journal of Physical Chemistry Letters*. 2015.

[66] T. Esram and P. L. Chapman, "Comparison of Photovoltaic Array Maximum Power Point Tracking Techniques," *IEEE Trans. Energy Convers.*, 2007.

[67] F. Haugen, "The good gain method for simple experimental tuning of PI controllers," *Model. Identif. Control*, 2012.

[68] J. G. Ziegler and N. B. Nichols, “Optimun setting for automatic controllers,” *Trans. Am. Soc. Mech. Eng.*, 1942.

[69] F. Haugen, “The Good Gain method for PI(D) controller tuning,” 2010. [Online]. Available: http://techteach.no/publications/articles/good_gain_method/good_gain_method.pdf. [Accessed: 02-Aug-2018].

[70] Q. Wang, J.-E. Moser, and M. Grätzel, “Electrochemical Impedance Spectroscopic Analysis of Dye-Sensitized Solar Cells,” *J. Phys. Chem. B*, 2005.

[71] A. Dualeh *et al.*, “Impedance spectroscopic analysis of lead iodide perovskite-sensitized solid-state solar cells,” *ACS Nano*, 2014.

[72] A. R. Pascoe, N. W. Duffy, A. D. Scully, F. Huang, and Y.-B. Cheng, “Insights into Planar CH3NH3PbI3 Perovskite Solar Cells Using Impedance Spectroscopy,” *J. Phys. Chem. C*, 2015.

[73] A. Pockett *et al.*, “Characterization of planar lead halide perovskite solar cells by impedance spectroscopy, open-circuit photovoltage decay, and intensity-modulated photovoltage/photocurrent spectroscopy,” *J. Phys. Chem. C*, 2015.

[74] G. Garcia-Belmonte, P. P. Boix, J. Bisquert, M. Sessolo, and H. J. Bolink, “Simultaneous determination of carrier lifetime and electron density-of-states in P3HT:PCBM organic solar cells under illumination by impedance spectroscopy,” *Sol. Energy Mater. Sol. Cells*, vol. 94, no. 2, pp. 366–375, 2010.

[75] L. Contreras-Bernal *et al.*, “Origin and Whereabouts of Recombination in Perovskite Solar Cells,” *J. Phys. Chem. C*, vol. 121, no. 18, pp. 9705–9713, 2017.

[76] J. M. Esteban and M. E. Orazem, “On the Application of the Kramers-Kronig Relations to Evaluate the Consistency of Electrochemical Impedance Data,” *J. Electrochem. Soc.*, vol. 138, no. 1, p. 67, 1991.

[77] M. Samiee *et al.*, “Defect density and dielectric constant in perovskite solar cells,” *Appl. Phys. Lett.*, 2014.

[78] N. Onoda-Yamamuro, T. Matsuo, and H. Suga, “Dielectric study of CH3NH3PbX3 (X = Cl, Br, I),” *J. Phys. Chem. Solids*, 1992.

[79] J. Bisquert, G. Garcia-Belmonte, and I. Mora-Sero, “Characterization of capacitance, transport and recombination parameters in hybrid perovskite and organic solar cells,” in *Unconventional Thin Film Photovoltaics*, 2016, pp. 57–106.

[80] A. Pockett, “Characterization of Perovskite Solar Cells,” University of Bath, 2016.

[81] I. Zarazua *et al.*, “Surface Recombination and Collection Efficiency in Perovskite Solar Cells from Impedance Analysis,” *J. Phys. Chem. Lett.*, 2016.

[82] Y. Shao, Z. Xiao, C. Bi, Y. Yuan, and J. Huang, “Origin and elimination of photocurrent hysteresis by fullerene passivation in CH3NH3PbI3planar heterojunction solar cells,” *Nat. Commun.*, 2014.

[83] J. Peng *et al.*, “Interface passivation using ultrathin polymer-fullerene films for high-efficiency perovskite solar cells with negligible hysteresis,” *Energy Environ. Sci.*, 2017.

[84] P. Jing *et al.*, “Vacuum-free transparent quantum dot light-emitting diodes with silver nanowire cathode,” *Sci. Rep.*, vol. 5, 2015.

[85] Q. Huang *et al.*, “High-performance quantum dot light-emitting diodes with hybrid hole transport layer via doping engineering,” *Opt. Express*, vol. 24, no. 23, pp. 25955–25963, 2016.

[86] M. D. Irwin, D. B. Buchholz, A. W. Hains, R. P. H. Chang, and T. J. Marks, “p-Type semiconducting nickel oxide as an efficiency-enhancing anode interfacial layer in polymer bulk-heterojunction solar cells,” *Proc. Natl. Acad. Sci.*, 2008.

[87] P. Da and G. Zheng, “Tailoring interface of lead-halide perovskite solar cells,” *Nano Research*, vol. 10, no. 5. pp. 1471–1497, 2017.

[88] A.-N. Cho and N.-G. Park, “Impact of Interfacial Layers in Perovskite Solar Cells,” *ChemSusChem*, 2017.

[89] I. Zarazua, J. Bisquert, and G. Garcia-Belmonte, “Light-Induced Space-Charge Accumulation Zone as Photovoltaic Mechanism in Perovskite Solar Cells,” *J. Phys. Chem. Lett.*, 2016.

[90] W. Tress, “Perovskite Solar Cells on the Way to Their Radiative Efficiency Limit – Insights Into a Success Story of High Open-Circuit Voltage and Low Recombination,” *Adv. Energy Mater.*, 2017.

APPENDIX

DERIVATION OF LIGHT IDEALITY FACTORS

The derivation of ideality factors obtained from the illumination dependence of open-circuit voltage is given in this appendix. The separation of quasi-Fermi levels can be given as:

$$E_{\mathrm{Fn}} - E_{\mathrm{Fp}} = k_{\mathrm{B}} T \ln\left(\frac{np}{n_{\mathrm{i}}^2}\right) \tag{A1}$$

where E_{Fn} and E_{Fp} are the electron and hole quasi-Fermi levels, k_{B} is the Boltzmann constant, T is the absolute temperature, n and p are the electron and hole concentrations, and n_{i} is the intrinsic carrier density. The ideality factor m is given as (see Equation 6.6):

$$\frac{\partial V_{\mathrm{OC}}}{\partial(\ln \Phi)} = \frac{m k_{\mathrm{B}} T}{q} \tag{A2}$$

where V_{OC} is the open-circuit voltage and Φ is the photon flux. Assuming the quasi-Fermi level separation to be equal to the open-circuit voltage i.e. $E_{\mathrm{Fn}} - E_{\mathrm{Fp}} = qV_{\mathrm{OC}}$, and recognizing the proportionality between the recombination rate U and photo flux Φ Equation A2 is equivalent to:

$$m = \frac{1}{k_{\mathrm{B}} T} \frac{\partial(E_{\mathrm{Fn}} - E_{\mathrm{Fp}})}{\partial(\ln U)} \tag{A3}$$

Combination of Equation A1 and A3 yields (note that $d\ln(x) = dx / x$):

$$m = \frac{U(n.dp + p.dn)}{np.dU} \tag{A4}$$

The recombination rate for Shockley-Read-Hall (SRH) recombination mediated by mid-gap traps is given in Equation A4:

$$U_{\mathrm{SRH}} \cong \frac{np - n_{\mathrm{i}}^2}{p\tau_{\mathrm{n}} + n\tau_{\mathrm{p}}} \tag{A5}$$

where $\tau_{\mathrm{p,n}}$ is the recombination lifetimes of respective carriers. Now, two different cases will be analyzed. First assume $n \gg p$ so that $U_{\mathrm{SRH}} = k_1 p$ where $k_1 = 1/\tau_{\mathrm{p}}$. Equation A4 yields (note that $dn = 0$ for this case) $m = 1$ as:

$$m = \frac{k_1 p(n.dp)}{np(k_1.dp)} = 1$$

Now assuming $n = p$ and $\tau_{\mathrm{p}} = \tau_n$, $U_{\mathrm{SRH}} = k_2 n$ where $k_2 = 1/(2\tau_{\mathrm{p}})$. Equation A4 yields $m = 2$ as:

$$m = \frac{k_2 n(2n.dn)}{n^2 k_2.dn} = 2$$

Overall:

$$m = \begin{cases} 1 & \text{for } n \gg p \text{ or low-excitation} \\ 2 & \text{for } n = p \text{ or high-excitation} \end{cases} \tag{A6}$$